Ph.D. Thesis

Universitat de Barcelona
Departament de Geodinàmica i Geofísica

A Magnetotelluric Investigation of Geoelectrical Dimensionality and Study of the Central Betic Crustal Structure

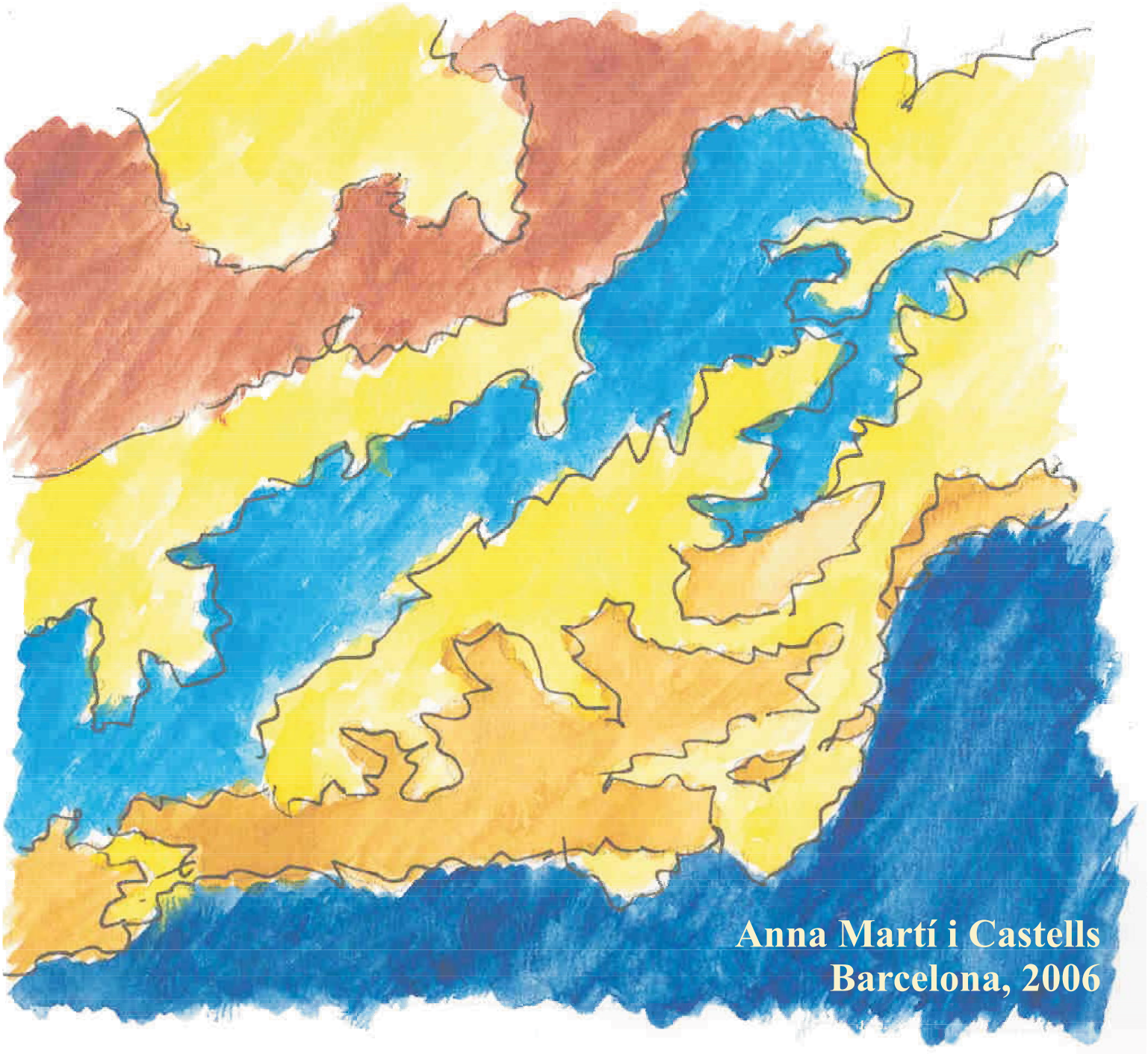

Anna Martí i Castells

Barcelona, 2006

Part III. Magnetotelluric Study of the Central Betics Crustal Structure

6. Geological and Geophysical Settings
7. Data Acquisition and Processing: Evaluation of MT Responses
8. Geoelectric Dimensionality Analysis of the Betics MT Data
9. 2D Modelling
10. 3D Modelling of the Central Betics Geoelectric Structure

Chapter 6: Geological and Geophysical Settings

This chapter presents the main geological description and geophysical features of the Betic Chain and the Alboran Basin, with the further purpose of constraining the interpretation of the magnetotelluric data recorded in the Central part of the Betics.

6.1 Geological Setting

The Betic Chain (Betic Cordillera or Betics) (Figure 6.1) is a WSW-ENE oriented Alpine Chain, located in the western end of the Mediterranean. It extends along the southern part of the Iberian Peninsula from the Gulf of Cádiz to Cape de la Nao and continues northeastward towards the Balearic Islands.

The Betics, together with the African Rif Chain, comprise an arc shaped orogenic belt, surrounding the present Alboran Basin, which was formed as a consequence of the convergence between the African and Iberian plates since the Late Cretaceous (60 My) (Platt and Vissers, 1989; García-Dueñas *et al.*, 1992; Azañón and Crespo-Blanc, 2000).

The formation of this arc and its inner Alboran Basin occurred in three main phases:

a) A Late Triassic – mid-Cretaceous extensional stage, related to the significant African plate left-lateral motion relative to a fixed Iberia (Dewey *et al.*, 1973; Rosenbaum *et al.*, 2002; Schettino and Scotese, 2002). During this stage, the area in question was affected by rifting processes that resulted, from the Liassic, to the Tethyan Oceanic accretion between the Iberian and African plates (García-Hernández *et al.*, 1980; Favre and Stampfli, 1992).

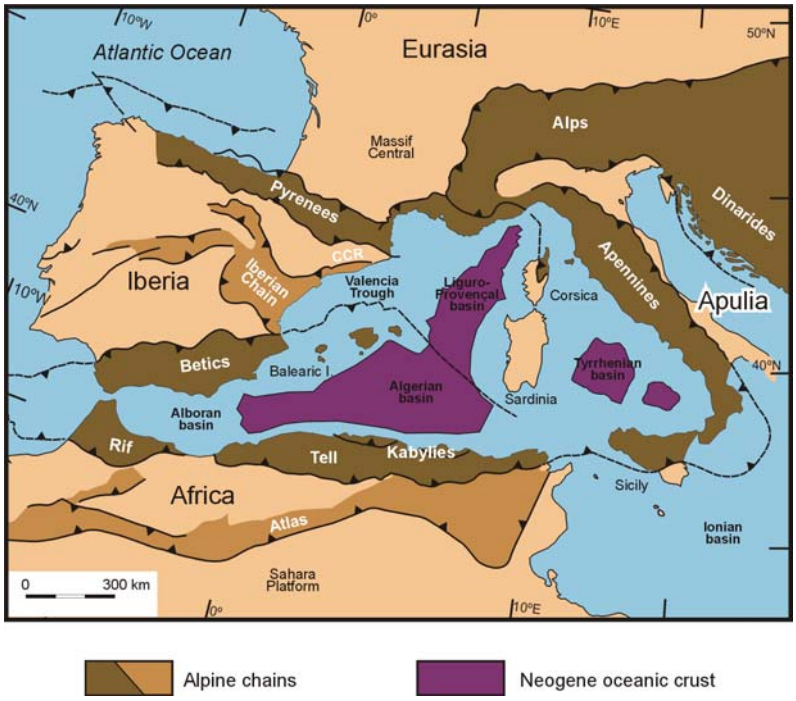

Figure 6.1: Simplified tectonic map of the Western Mediterranean region with the main Alpine compressive chains and Neogene extensional basins (Roca, 2004).

b) A Late Cretaceous-Middle Oligocene stage, characterised by the beginning of a relatively fast NE-SW to N-S convergence between Iberia, Eurasia and Africa (Dewey *et al.*, 1989; Mazzoli and Helman, 1994; Rosenbaum *et al.*, 2002). This convergence resulted in the development of an orogen from subduction and orogenic wedging between Africa and Iberia, which constituted what is known as the Alboran Domain (Balanyá and García-Dueñas, 1987).

c) An Oligocene-Miocene stage of strong tectonic activity which developed during a slowing of the N-S convergence between Eurasia and Africa (Dewey *et al.*, 1989; Mazzoli and Helman, 1994). During this stage, back-arc extension processes related to N-dipping subduction of the African slab below the Alboran Domain (Rehault *et al.*, 1984; Frizon de Lamotte *et al.*, 2004) resulted in the opening of the Alboran Basin and the outward migration (mainly to the West) of the Gibraltar Thrust (outer limit of the Alboran Domain). This migration thrust, during the Miocene, collided with the passive paleomargins of Africa and Iberia, inducing the development of fold-and-thrust belts (Rif and Betic chains) in the sedimentary materials settled during the former stage (Balanyá and García-Dueñas, 1987). At the same time, the thrust belt previously formed in the Alboran Domain continued in an extensive regime with the formation of low angle faults, which lead to a 13 km - 20 km crustal thinning of the Alboran basin.

In relation to this geological evolution, the Betic Chain has been traditionally divided in two stratigraphically and structurally well-differentiated zones: the External Zone and the Internal Zone (Figure 6.2).

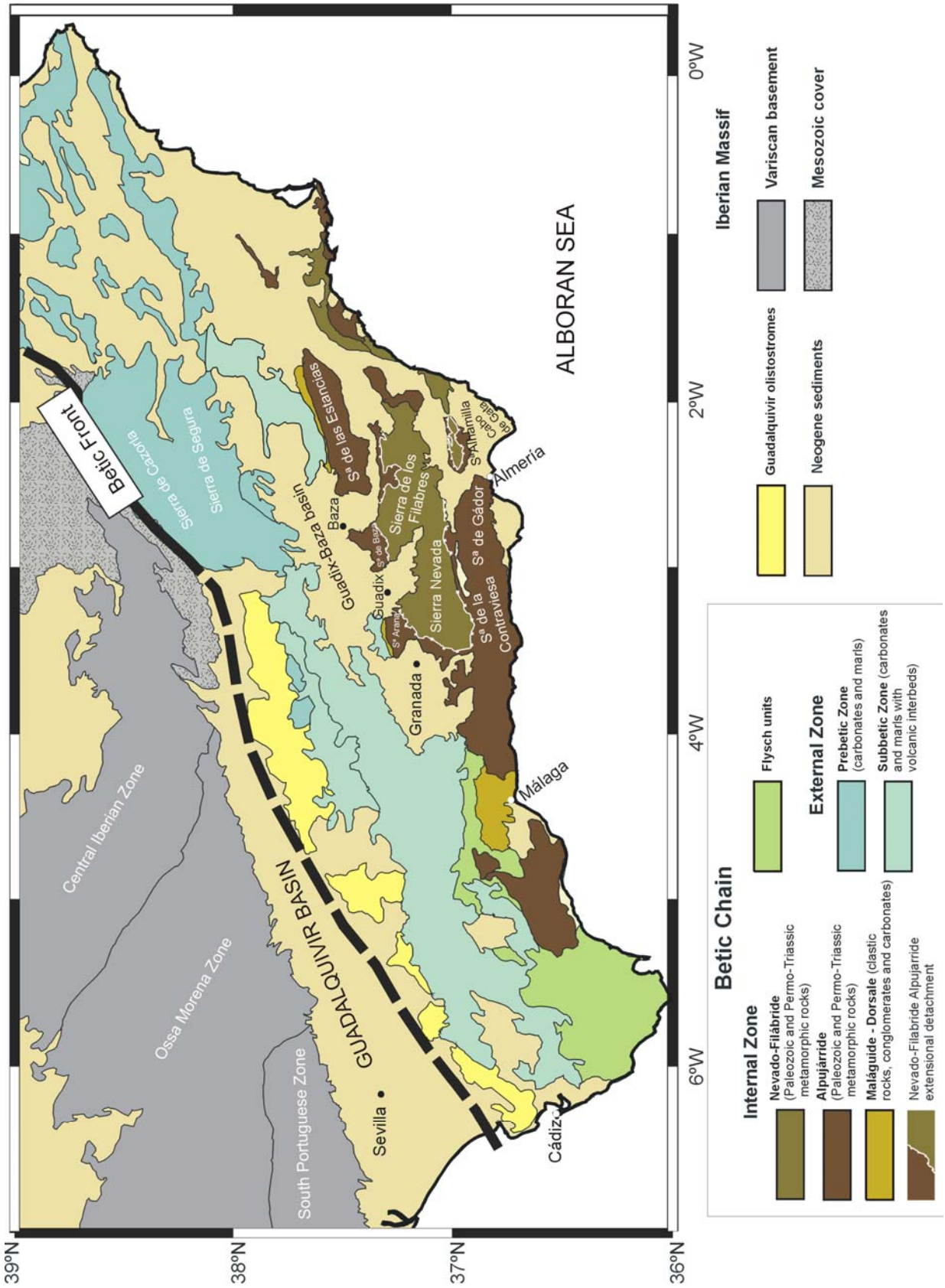

Figure 6.2: Geological sketch map of the Betic Chain.

The **External Zone** is derived from the Mesozoic sedimentary cover of the South Iberian paleomargin of the Tethys (García-Hernández *et al.*, 1980) and crops out in the Northwest of the Chain. It comprises the *Prebetic* and *Subbetic* zones, both formed by non-metamorphosed rocks (mainly carbonates and marls) of Triassic to Neogene age. The *Prebetic Zone* is characterised by shallow-water facies, as opposed to the *Subbetic Zone*, where pelagic facies prevail with some mafic volcanic and subvolcanic interbeds. Both *Prebetic* and *Subbetic* zones are defined as an ENE to NE-trending fold-and-thrust belt with the main transport direction towards the NNW.

Between the External and Internal zones, are the *Flysch units*. These are deformed deep-water sediments, Cretaceous to Miocene in age, which are interpreted as the former sedimentary cover at the paleomargins of the westernmost part of the Tethys Ocean. Hence, the *Flysch units* are structurally below the Internal Zone, with some exceptions, as observed near Ronda and Antequera (Azañón *et al.*, 2002; Frizon de Lamotte *et al.*, 2004).

The **Internal Zone**, in the Southeast, is formed by metamorphic rocks from the Paleozoic and locally from the Mesozoic belonging to the Alboran Domain (Balanyá and García-Dueñas, 1987). The interior structure of the Internal Zone is highly complex, with several stacked thrust sheets emplaced before the Miocene that were affected and cut by low angle normal faults during the latest Oligocene-Miocene opening of the Alboran Basin. These extensional faults determine the present-day structure of the Internal Zone and are associated with the development of several intramontane basins filled with continental and marine Neogene and Quaternary sediments (Sanz de Galdeano and Vera, 1992). The innermost of these basins (e.g., Cabo de Gata) include widespread calc-alkaline Neogene volcanic rocks (López Ruiz *et al.*, 2004). The whole area is deformed and uplifted due to Late Tortonian E-W folding. As a consequence, the lowest sequence materials crop out in the cores of the anticlines (Azañón *et al.*, 2002).

According to their stratigraphic signatures and metamorphic conditions, the stacked thrust sheets of the Internal Zone have been grouped into three nappe complexes, separated by major low angle faults. From lower to upper, these nappes are: the Nevado-Filábride complex, the Alpujárride complex and the Maláguide-Dorsale (Figure 6.3).

The *Nevado-Filábride Complex* is the lowest metamorphic complex and crops out in the Sierra Nevada, Sierra de los Filabres and Sierra de Alhamilla. It consists of three major thrust units (García-Dueñas *et al.*, 1988) containing a thick Paleozoic graphitic schist and quarzite series, Permo-Triassic metapelites and metapsammites and a calcite and dolomite marble formation, Triassic to Cretaceous (?) in age. All rocks of this complex were affected by high pressure – low temperature (HP-LT) metamorphic conditions (Monié *et al.*, 1991).

The *Alpujárride Complex* overthrusts the Nevado-Filábride, although its present boundary corresponds to a Serravallian to Early Tortonian extensional detachment. This

complex is also mainly made up of Paleozoic schists, graphitic micaschists and quartzites, Permo-Triassic metapelites and metapsammites, and calcite and dolomite marbles, Middle to Late Triassic in age (Braga and Martín, 1987; Azañón and Crespo-Blanc, 2000). In the western Betics, this complex includes slices of peridotites and granulites representative of sub-continental lithospheric mantle (Ronda massif). All these rocks were affected by low temperature and medium-high pressure metamorphic conditions during the Paleogene and were later deformed by folds and a penetrative foliation.

The *Maláguide-Dorsale Complex* belongs to the uppermost unit. It contains Paleozoic sedimentary clastic rocks, Middle Triassic continental red conglomerates and an upper succession of carbonate rocks, Middle Triassic to Paleogene in age. The Paleozoic rocks retain Variscan orogenic features (folding and low-grade metamorphic foliation), whereas its Mesozoic to Paleogene cover did not suffer pervasive deformation nor metamorphism (Azañón *et al.*, 2002).

The geometry of the boundary between the Internal and External zones (IEZB) varies from West to East (Frizon de Lamotte *et al.*, 2004). In the western part, the Internal Zone thrusts over the Subbetic zone and the Flysch units (e.g. Platt *et al.*, 2003). In the central and Eastern Betics, the Internal Zone structurally crops out below the Subbetic zone, which is interpreted as a wedge-shaped indentor (Banks and Warburton, 1991; Platt *et al.*, 2003).

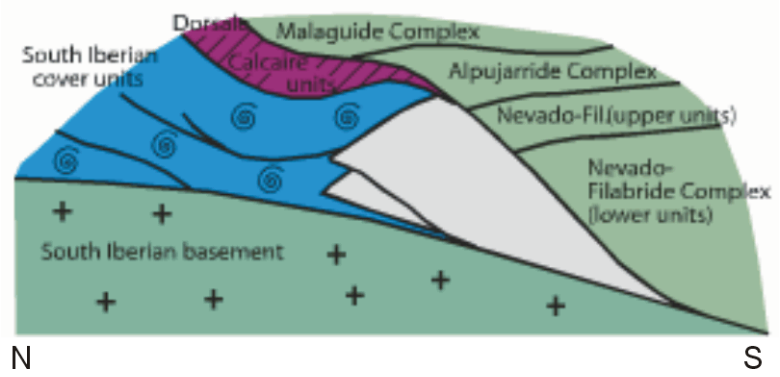

Figure 6.3: Sketch of the relationships between the Internal and External (South Iberian cover) zone units and the Iberian Massif basement in the Central Betics. The scheme proposed is a hybrid solution between the different geometries from West to East. (Modified from Frizon de Lamotte, 2004 with data from Navarro-Vilá and García-Dueñas, 1980 and Balanyá, 1991).

Both Internal and External zones of the Betic Chain overthrust (e.g. Figure 6.3) the Iberian Massif or Iberian Meseta, which near the Betic Chain is overlaid by the Neogene sediments of the Guadalquivir Basin. This basin belongs to the northern foreland basin of the

Betic Chain and is elongated ENE-WSW. It is filled with marine sediments from the Early Miocene up to the present ages (Fernàndez *et al.*, 1998a).

Beneath and North of the Guadalquivir Basin there are Paleozoic and Precambrian rocks of the Iberian Massif. This massif belongs to a portion of the Variscan orogen, formed by sedimentary and volcanic rocks strongly deformed and metamorphosed during the Late Paleozoic. Close to the Betics, it is divided into three NW-SE directed tectonic units with significant stratigraphic and structural features. From NE to SW, these are (Figure 6.2):

- The Central Iberian Zone (CIB), formed by Precambrian and Paleozoic rocks affected by a variable degree of metamorphism with large granitic and granitoid intrusions.
- The Ossa Morena Zone (OMZ), made up of Precambrian to lower Paleozoic sediments, also with a variable degree of metamorphism, and granitoid intrusions.
- The South Portuguese Zone (SPZ), formed by middle to upper Paleozoic rocks, with important sulphur deposits.

The contact between SPZ and OMZ is interpreted as a suture, with basic igneous rock outcrops of oceanic affinity (Pérez-Estaún and Bea, 2004; Ábalos *et al.*, 2002).

6.1.1 Geodynamic Models of the Betic-Alboran-Rif Region

Nowadays it is accepted that the geodynamic evolution of the Betic-Alboran-Rif (BAR) region includes a stage of subduction and orogenic wedging of the Alboran domain, which occurred in an almost constant position; followed by a stage of compression and thrusting along the Gibraltar Arc and coeval extensional opening of the Alboran Basin. However there are two open geodynamic problems in which several hypotheses have been proposed. The first problem is on the state of the initial subduction (stage b), page 132). The second is on the nature of the coeval extension and compression.

With regard to the first problem, two main models have been proposed (Frizon de Lamotte, 2004), to explain the timing of high-pressure events and metamorphic stacking. The first one (e.g. Doglioni *et al.*, 1999) proposes two types of subduction, which acted successively: first, an E to S dipping subduction from the Late Cretaceous to Early Oligocene, which closed a Betic ocean; and a second W to N dipping subduction of the Appeninic-Maghrebian system obliterating the Flysch units from Late Oligocene to Early Miocene (Figure 6.4). The second model suggests a N-dipping subduction which produced a bi-vergent wedge and its progressive roll-back (Jolivet and Faccenna, 2000).

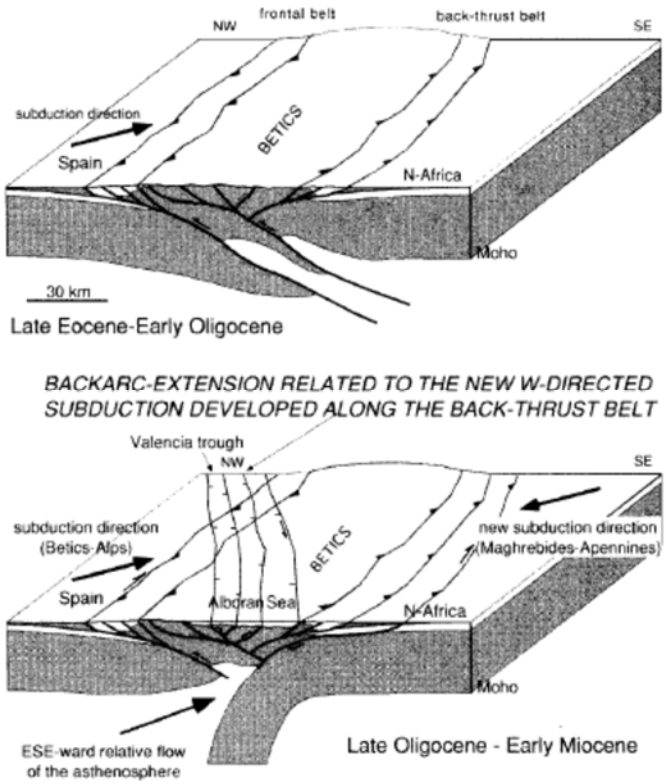

Figure 6.4: Sketch of the superposition of two subduction modes in the formation of the Betic-Gibraltar arc, according to Doglioni *et al.* (1999).

In relation to the coeval thrusting and extension in the BAR region, three main models have been proposed, the last one being the most widely accepted (Figure 6.5):

a) Convective removal of a thickened lithosphere (Platt and Vissers, 1989).

b) Gravitational collapse of a thickened lithosphere (Seber *et al.*, 1996).

c) Westward to southward rollback of an eastward-northward dipping subduction of the African slab that generated back arc extension, which that migrated westward (Royden, 1993; Lonergan and White, 1997; Gutsher *et al.*, 2002).

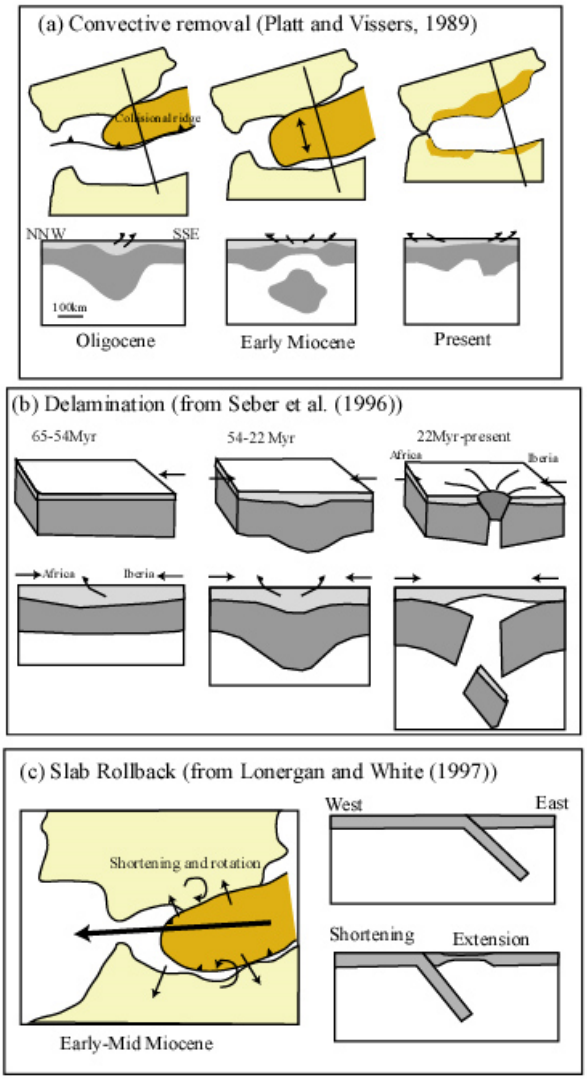

Figure 6.5: Main tectonic models proposed to explain the opening of the Alboran Basin and coeval thrusting and extension along the Gibraltar Arc (Calvert *et al.*, 2000)

6.2 Geophysical Knowledge of the Central Betic Chain

Within this geodynamic framework, as reviewed above, a significant number of geophysical studies performed show that the crustal and lithospheric structure of the Betics is highly complex and difficult to characterise. Thus, the geophysical studies carried out, including gravimetry, magnetism, seismic refraction, reflection and tomography, heat flow and magnetotellurics, have lead to different interpretations for the deep structure of the central Betic Chain.

In the following sections, the main geophysical results and interpretations are presented to summarise the present knowledge of the whole Central Betic crust and upper mantle structures.

6.2.1 Gravimetry

Maps of Bouguer gravity anomalies in the Betics and the Alboran Sea (IGN, 1976; Casas and Carbó, 1990) show a minimum below the Guadiz-Baza basin (-150 mGal), with an ENE-WSW orientation (red area in Figure 6.6), and maximum values of 100 mGal and higher below the Alboran Sea. In the eastern part of the Betics, the gradient between these minimum and maximum values is smooth whereas in the central and western parts this gradient is more abrupt. Towards the North of the minimum, the anomaly increases gradually until reaching values of about –50 mGal, which are common in the Iberian Massif. More locally, positive anomalies are located North of Malaga.

With the exception of these last anomalies, which have been associated with the presence of peridotitic bodies, gravimetric data allow the characterisation of the variations in crustal thickness in the Betics area. Hence, these data indicate a crustal thickening from the Iberian Massif towards the Internal Betics, then a crustal thinning towards the Alboran Sea. It should be also noted that the minimum anomaly values, corresponding to a maximum in crustal thickness (40 km - 45 km), are located in the Guadix-Baza basin and not in Sierra Nevada, which suggests the lack of a significant root below the highest altitudes of the Betics.

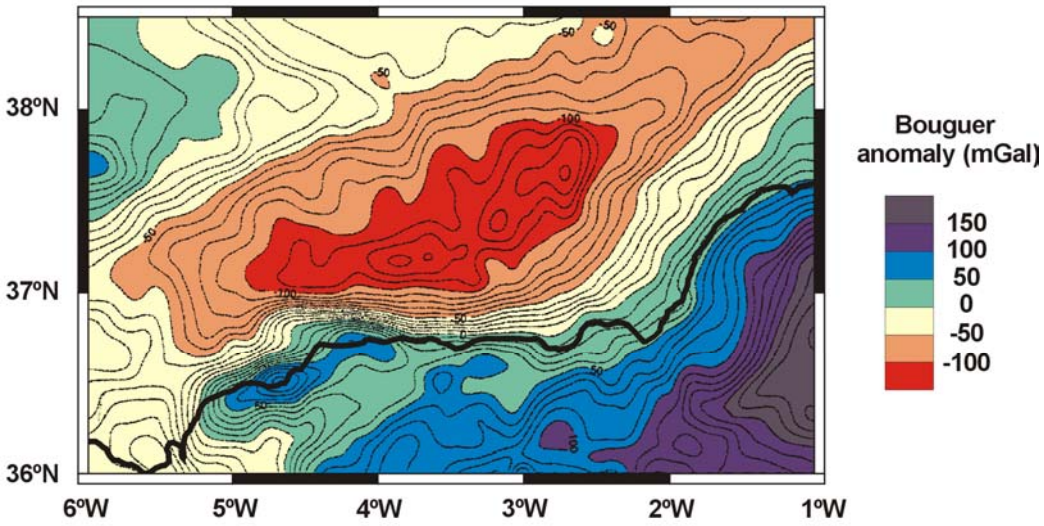

Figure 6.6: Bouguer gravity anomalies map of a Southern sector of the Betics (modified from Torné and Banda, 1992).

6.2.2 Magnetism

The southeastern sector of the 1:1000000 aeromagnetic anomaly map of Spain (Figure 6.7) (Ardizone *et al.*, 1989) shows that in the External Zone the magnetic anomalies are controlled by the crustal structure and not by mesozoic and cenozoic sediments. This crust presents a Variscan structure, which is a continuation of Iberian Massif outcrop materials. For the particular case of the intense NW-SE anomalies that cross from the Iberian Massif to the External Zone, these have been interpreted as igneous rock bodies that outcrop in the Ossa Morena zone, which would continue below the External zone, up to the boundary between the Internal and External zones (Galindo-Zaldívar *et al.*, 1997; Bohoyo *et al.*, 2000). In the Internal Zone, aeromagnetic anomalies are more localised, or have an EW to ENE-WSW orientation. Among these, an ENE-WSW directed anomaly (70 nT and 15 km – 20 km dipole length) is located, east of Guadix, in the Sierra de los Filabres. It was modelled as being caused by Fe-mineralizations in joints of the Nevado-Filabride metamorphic rocks, up to 10 km depth, with a susceptibility value of χ=0.005 (SI) (Galindo-Zaldívar *et al.*, 1997). Other local anomalies are found above the Ronda peridotitic bodies and in the Cabo de Gata volcanic zone.

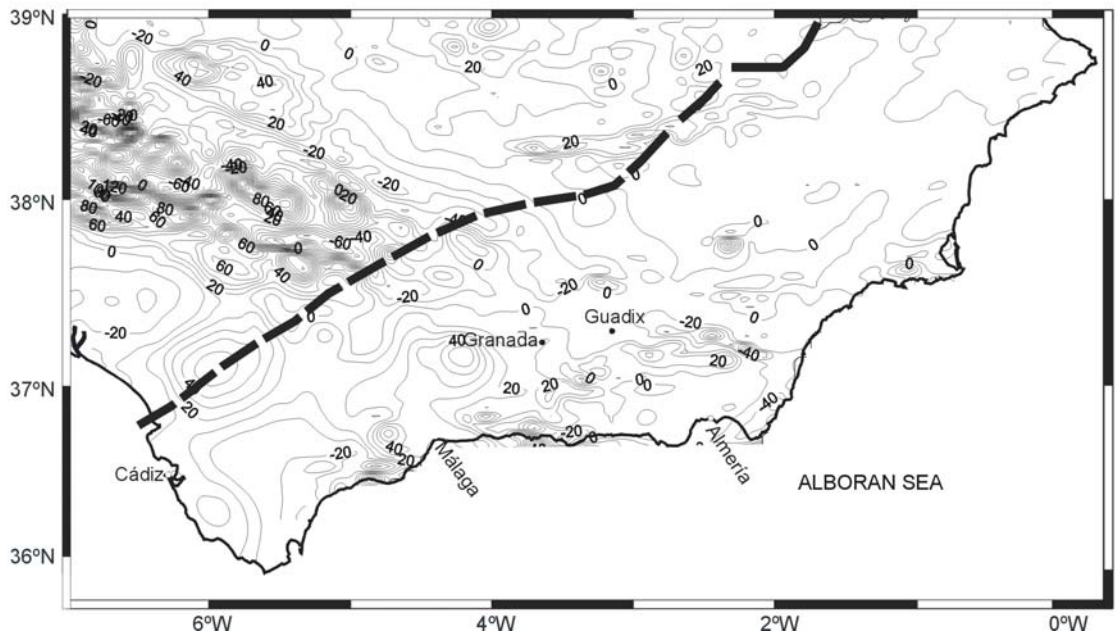

Figure 6.7: Total field magnetic anomalies map (data from Ardizone *et al.*, 1989) of the Betics and southwestern sector of Iberian Massif. Isomagnetic values in nT.

6.2.3 Seismic Refraction Profiles

Refraction seismic profiles carried out in the Betics and the Alboran Sea (Figure 6.8) (Suriñach and Udías, 1978; Banda and Ansorge, 1980; Banda *et al.*, 1983; Medialdea *et al.*, 1986; Banda *et al.*, 1993) made it possible to characterise the Moho depths and intracrustal velocity discontinuities (mainly upper and lower crustal boundaries) in the Central Betics sector.

The interpretation of these profiles shows the following:

- A crustal thickness of 30 km – 35 km in the Iberian Massif.
- Two zones with different crustal structure could be distinguished in the Betic Chain, separated by the Carboneras-Palomares and Alhama de Murcia fault system (Banda and Ansorge, 1980). In the West, the crust can be divided into three layers with different velocities, reaching a total depth of 39 km. In the eastern zone, the crust has two layers and a total thickness of 23 km.
- Towards the South, the crust thins and reaches minimum thicknesses of 13 km to 16 km below the Alboran Sea.
- Both below the Betics and the Alboran Sea, the lower crust is not seismically detected.
- This Southward directed thinning leads to crustal thicknesses along the coast of 23km to 25km.
- SW of Malaga, there is a high velocity body (7 km/s - 7.2 km/s) detected, whose interpretation is speculated on the presence of mantle peridotites, a thinned crust or both (Barranco *et al.*, 1990).

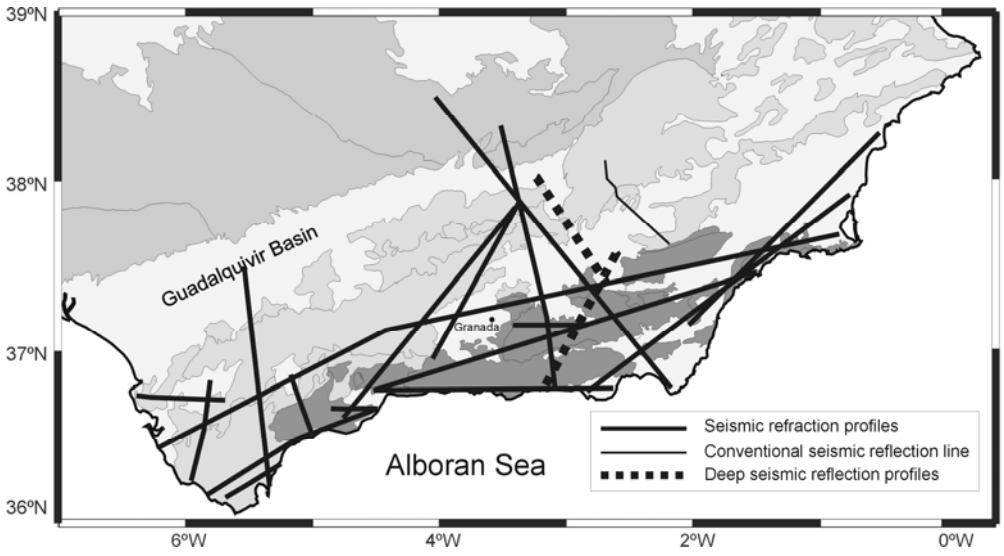

Figure 6.8: Location of seismic refraction and reflection profiles in the Betics.

6.2.4 Seismic Reflection Profiles

Seismic reflection data in the Central Betics is available from multichannel seismic profiles for hydrocarbon exploration and deep reflection profiles.

Among the first, a NW-SE directed profile, BT-3 (Figure 6.8) (Jabaloy *et al.*, 2005), allowed imaging the structure of the contact between the Internal and External zones in the eastern Betics. In this interpretation, the Alpujárride and Maláguide units act as a wedge-shaped indentor between the Prebetic and Subbetic units (Figure 6.9).

Two deep seismic profiles were carried out in the Central Betics: the ESCI-B1, NW-SE directed, that crosses the Guadalquivir Basin and the External Zone; and the ESCI-B2, SW-NE, which, in continuity with the previous profile, crosses the Internal Zones (García-Dueñas *et al.*, 1994) (Figure 6.8).

These two depth converted profiles show:

- The geometry of the Moho, located at 35 km below the External Zone and at a shallower position (≈28 km) below the Internal Zone.
- A well differentiated lower crust with several subhorizontal reflectors and a more or less constant thickness of 15 km – 16 km, and an upper boundary, which is parallel to the Moho at any location below the profiles.
- A transparent upper crust with different features below the External and Internal zones. In the first zone, the upper crust is transparent with a reflective shallow level, with a slightly SE dipping bottom, which corresponds to the Mesozoic and Cenozoic rocks of the External Zone and the Guadalquivir basin. Below the Internal Zone, the upper crust is also transparent, although with the presence of horizontal and dipping bands of reflectors, such as the northeast-dipping UCR. These bands of reflectors follow a dome shape and are interpreted as mylonitic bands. The bands and dome do not affect the lower crust and, consequently, denote a major crustal detachment located at around 10 km – 15 km depth, which corresponds to the Iberian-Alboran domain boundary (Galindo-Zaldívar *et al.*, 1997).

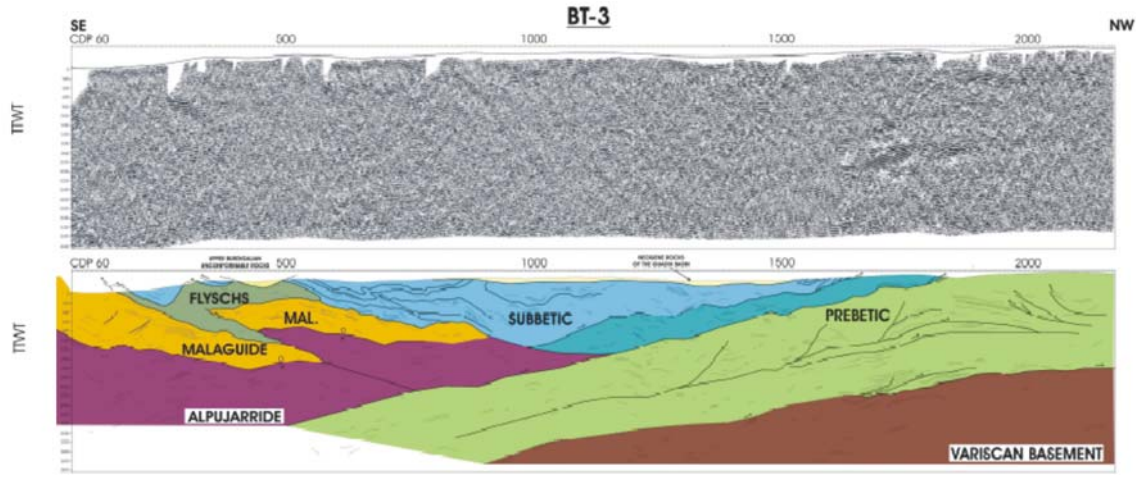

Figure 6.9: Seismic profile BT-3, cross-section and interpretation (Jabaloy *et al.*, 2005).

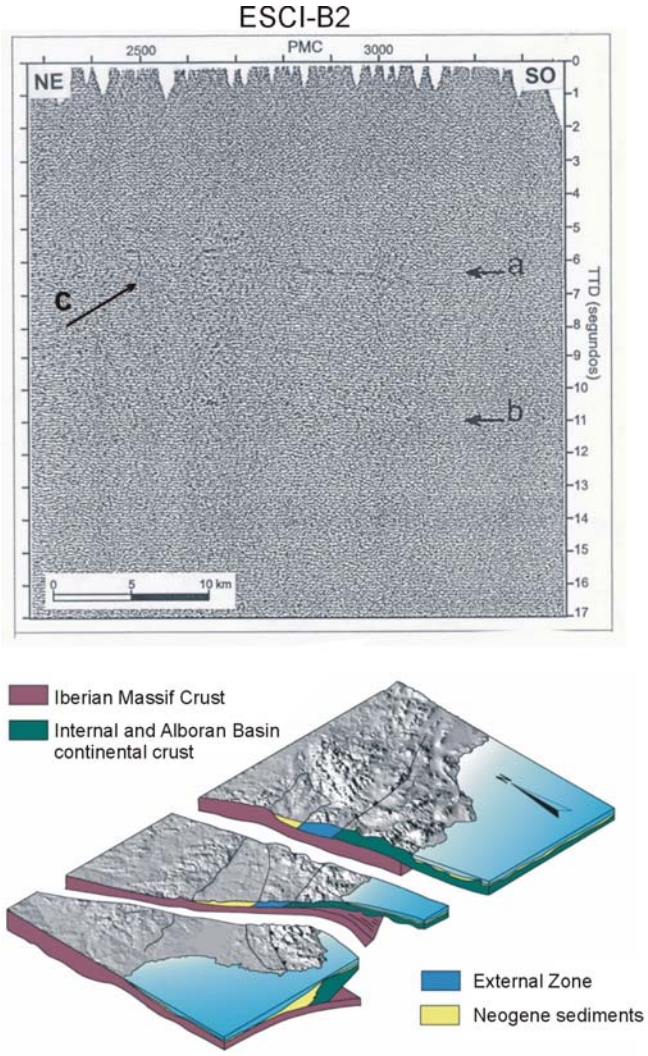

Figure 6.10: Deep seismic profile ESCI-B2. Upper panel: a: upper and lower crust discontinuity. B:Moho. C: Upper Crustal Reflector. Lower panel: sketch of the main crustal structures (modified from Galindo-Zaldívar *et al.*, 2004).

6.2.5 Seismicity and Seismic Tomography

The seismicity of the Betic-Alboran-Rif region is moderate but active (Figure 6.11), with the highest activity located between 3.5°W and 5°W. Earthquakes are mainly produced at mid to low depths, with an important gap between 200 km and 600 km, and some very deep earthquakes which have been recorded (29.3.1954, 30.1.1973, 8.3.1990 and 31.7.1993) under the central and western part of Sierra Nevada, with hypocentral depths > 600 km (IGN, 2001).

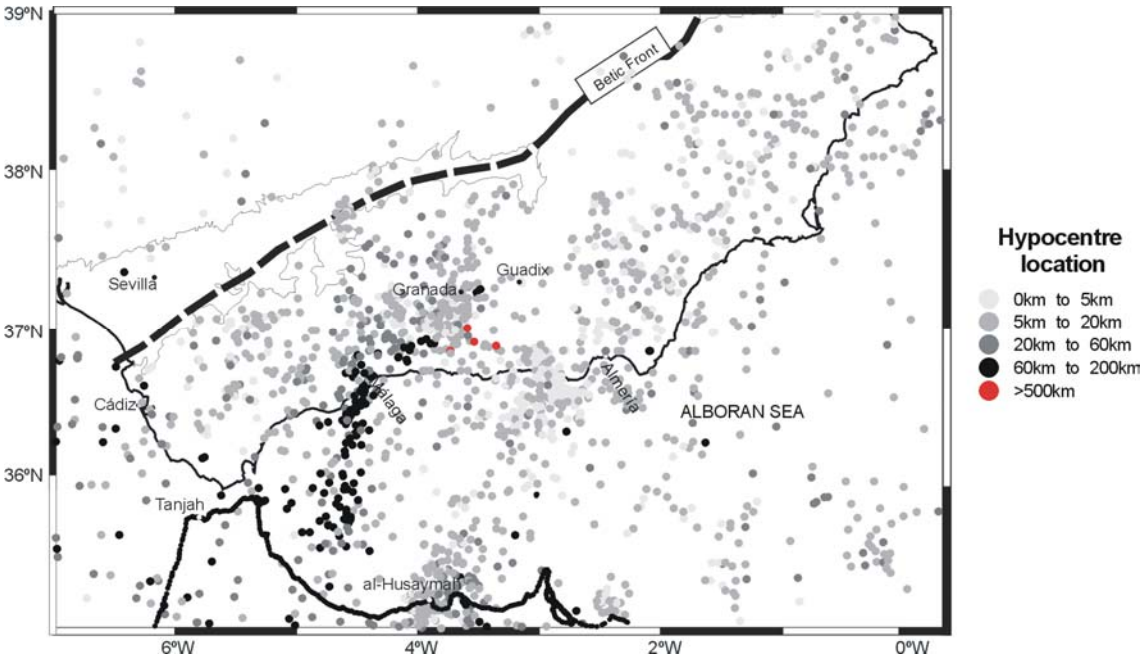

Figure 6.11: Seismicity map of the Betic-Alboran-Rif region. Seismic events from 1950 to 2001 and magnitudes $M_b \geq 3$ have been considered (data from IGN, 2001).

Seismic tomography studies allowed obtaining P-velocity images of the Betics area at crustal - upper mantle levels (Figure 6.12) (Dañobeitia *et al.*, 1998; Serrano *et al.*, 1998).

The results show low velocity zones below the basins, although these continue at lower depths (e.g., 15 km below the Granada Basin, interpreted as fluids along fractures; and 12 km below the Guadix-Baza Basin, suggesting a greater sediment thickness).

At upper crustal levels, high velocity anomalies are found below the Internal and External zones and the contact between them. The anomaly is lower in the External Zone, due to the higher presence of sedimentary materials. At middle and lower crustal levels, these positive anomalies continue below the Internal and External zones, whereas at the contact zone, the velocity is significantly lower.

At the upper mantle, a low velocity anomaly is detected, at the boundary between the Alboran Sea and the Betics.

Lithospheric seismic tomography studies of the Betic- Rif-Alboran region (Calvert *et al.*, 2000) image a high velocity SE dipping body that extends from the Betics to the Alboran Sea, located at depths between 60 km and 400 km, which, followed by a low resolution area, continues up to 650 km.

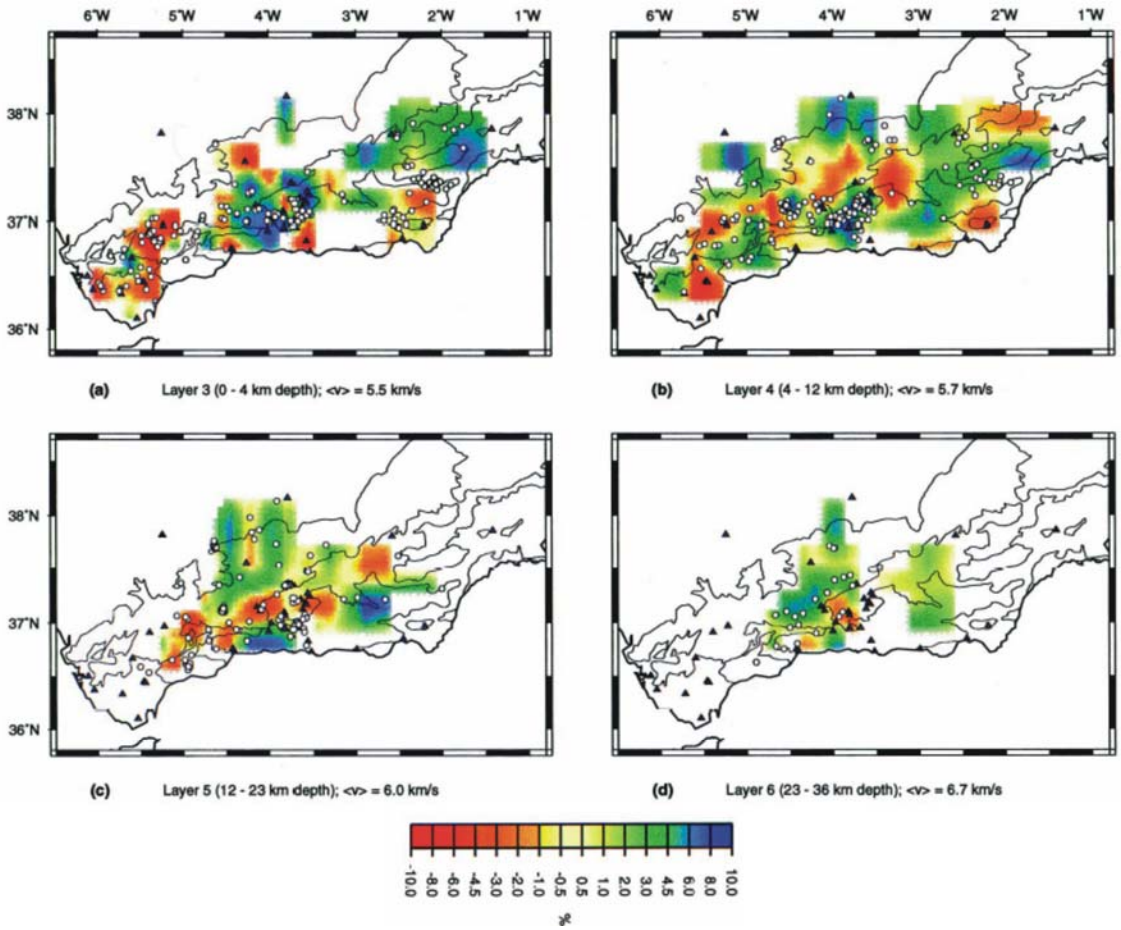

Figure 6.12: Maps of P-velocity anomalies of the Betics crust (after Dañobeitia *et al.*, 1998). Black triangles: station locations. Circles: hypocentral locations within each layer.

6.2.6 Heat-flow

Heat-flow and heat-production maps of the Iberian Peninsula show a rather constant heat-flow value both in the Internal and External zones (60 mW/m^2 – 70 mW/m^2), in continuity with the values obtained from the Iberian Massif and the rest of the peninsula. Towards the South, an abrupt increase of the heat-flow is observed on the coastline, from which it continues increasing until reaching maximum values of 100 mW/m^2 to 120 mW/m^2 in the Alboran Sea

(Fernàndez *et al.*, 1998b). This heat-flow increase has been interpreted as due to the lithospheric thinning from 100 km - 110 km (below the External and Internal zones) to 40 km thick in the Alboran Sea (Polyak *et al.*, 1996).

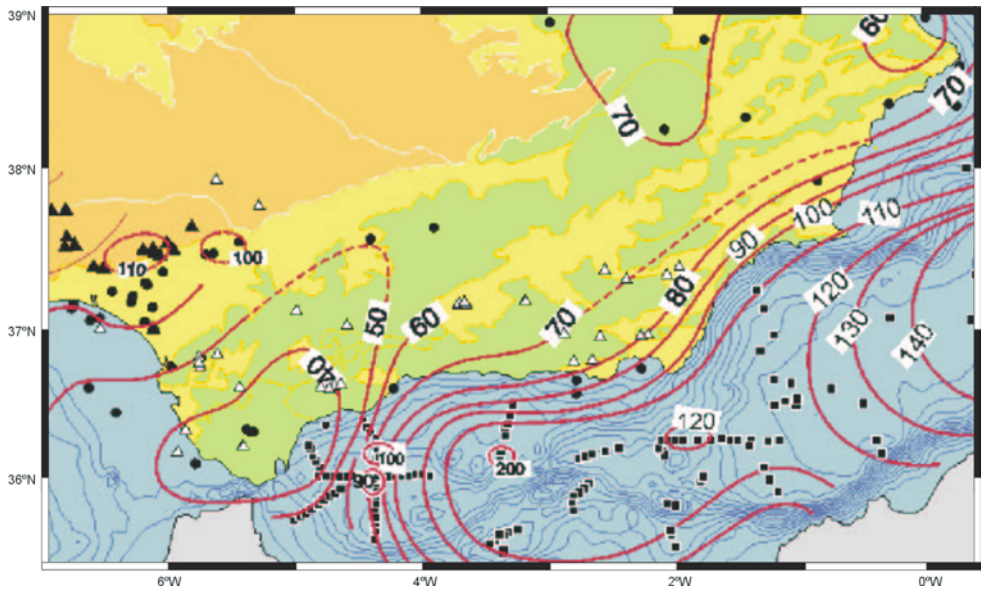

Figure 6.13: Heat-flow map of the Betic-Alboran region. Isolines in mW/m^2. Dots indicate measurements in oil wells; triangles, water and mining exploration wells; and squares, seafloor heat-flow measurements (modified from Fernàndez *et al.*, 1998b).

6.2.7 Magnetotellurics

Previous to the work done in this thesis, a magnetotelluric survey was carried out in the central Betic Chain (Pous *et al.*, 1999). It included 41 sites, with periods recorded from 4ms to 4000s that were acquired between the Iberian Massif and the Alboran Sea coastline.

From this first set of data, a 2D resistivity model was constructed, along a NW-SE strike direction, crossing the Betic Chain from the Guadalquivir Basin to Sierra de Alhamilla (Figure 6.14). The main features of the model are a shallow conductive zone in its northwesternmost part (A); and a shallow resistor, two mid-crustal conductors and a deep conductive body (20 km to 40 km depth) below the Internal Zone.

The main features of the model are three shallow-middle crustal conductors (A, B and D), a shallow resistive zone (C) and a deep conductive body (E), located between 20 km and 40 km depth. The shallow and middle crust conductors have been interpreted as fluid circulation along sedimentary materials (A, Guadalquivir Basin) and along faults (B and D). The shallow resistor C corresponds to metamorphic materials of the Internal Zone. The deep conductive

body, D, located below the Internal Zone, was interpreted as partial melting of the Iberian lower crust under the Alboran Domain.

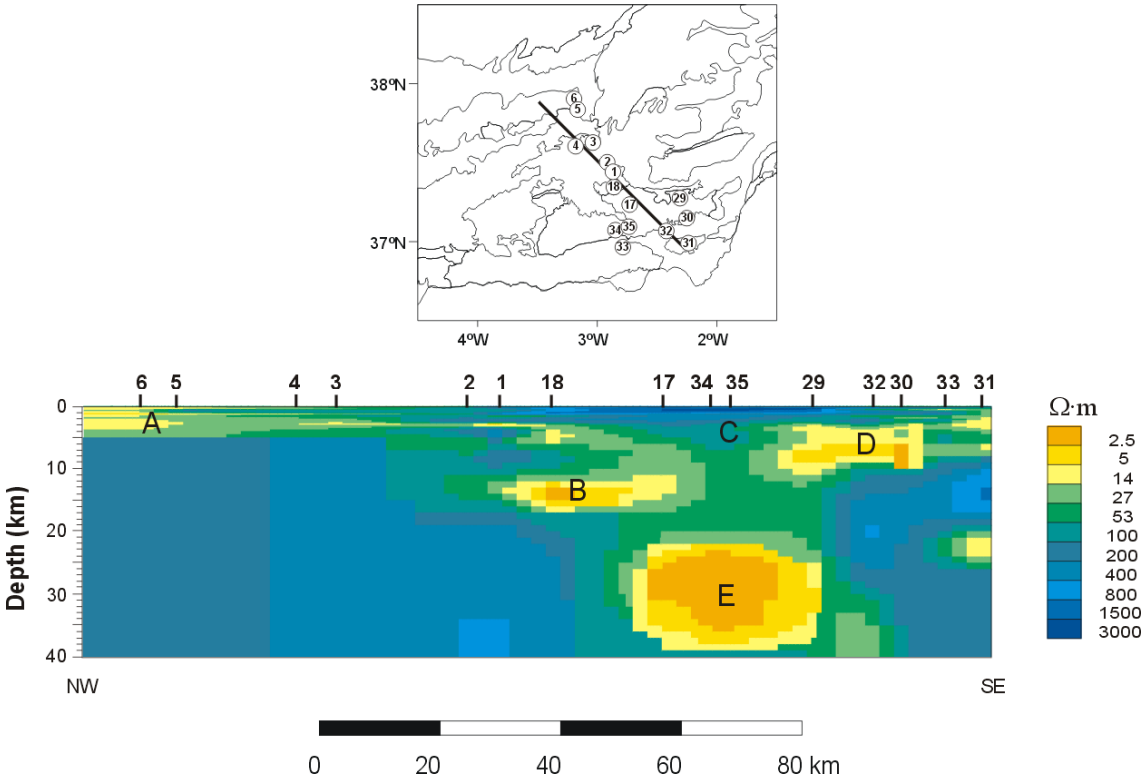

Figure 6.14: Location of MT sites and 2D electrical resistivity model. Circled numbers indicate site locations. A, B, C, D and E are the main conductive structures identified and interpreted.

6.2.8 Summary

The geophysical studies described in the previous chapters allow recognising the main features of the Central Betics inner structure, as have been identified through geophysical disciplinary studies carried out in the last decade (e.g. Galindo-Zaldívar *et al.*, 1997; Carbonell *et al.*, 1998; Morales *et al.*, 1999; Serrano *et al.*, 2002; Frizon de Lamotte, 2004 (Figure 6.15)). The main features are:

- Crustal thickness between 30 km and 40 km below the Internal and External zones, higher on average than those below the Iberian Massif (30 km – 35 km). The maximum crustal thickness, according to gravimetric studies, is located below the Guadix-Baza basin, which indicates the absence of a significant root below the highest elevations of the Betics, in the Sierra Nevada. The crustal thickness decreases towards the coast,

where it reaches values between 20 km and 25 km, and continues decreasing until reaching minimum values below the Alboran Sea (13 km-16 km).

- Continuity of the Iberian Massif below the Betics structure.

- Presence of an anomalous body at lower crustal levels below the Internal Zone, with a low electrical resistivity and low velocities.

- A high velocity slab in the lithospheric mantle below the Internal Zone and Alboran Sea.

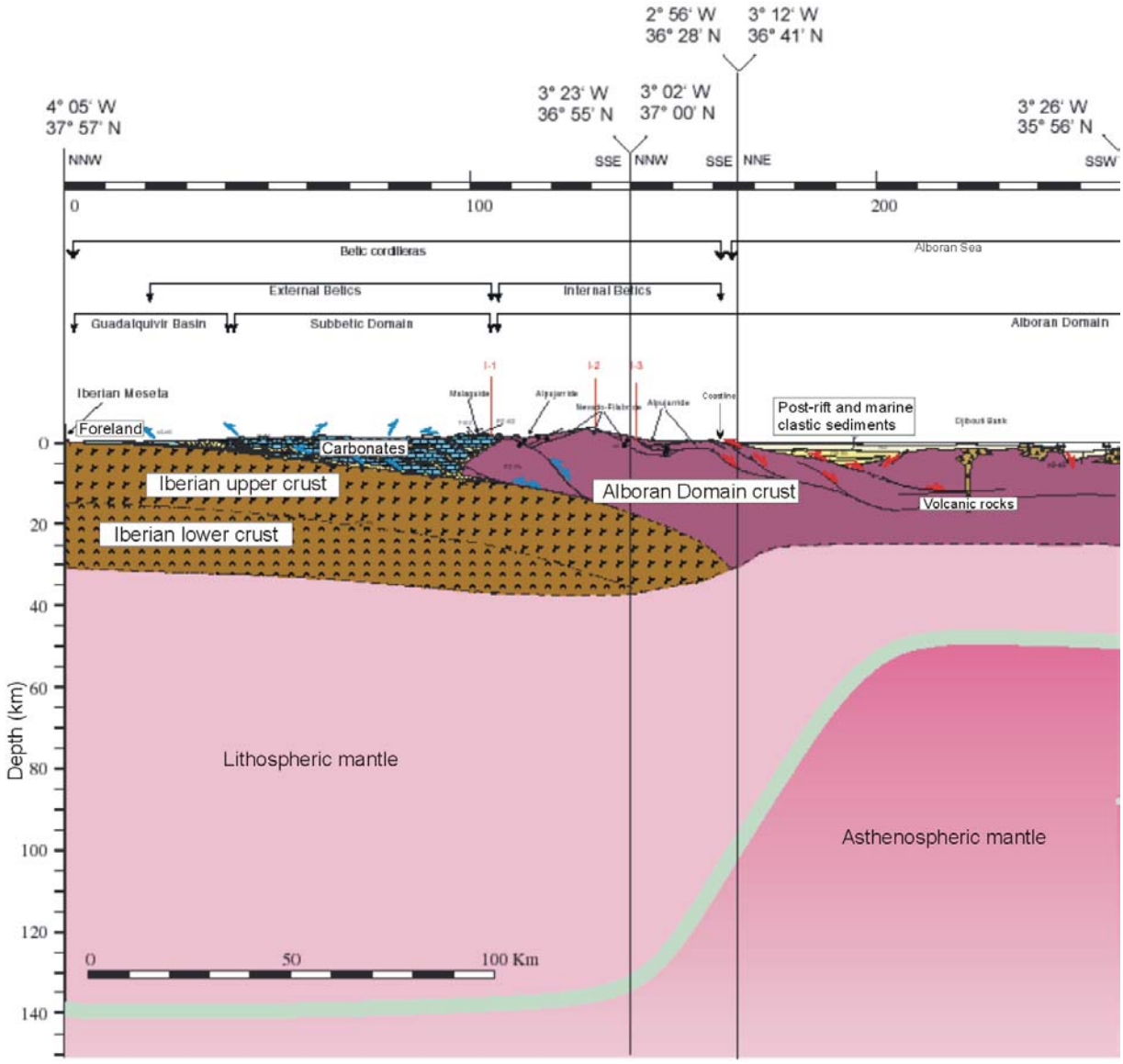

Figure 6.15: Northern portion of TRANSMED Transect I, showing a lithospheric cross-section of the Betic Chain based on geophysical, geological and well data (Frizon de Lamotte *et al.*, 2004).

Chapter 7: Data Acquisition and Processing: Evaluation of MT Responses

The data used in the magnetotelluric study of the Betics were acquired during the former MT survey carried out in 1994-1995, whose data have been processed or reprocessed, as well as in the new survey performed in 2004, for which all the acquisition and processing was done.

In this chapter, the details on how these data were acquired and processed are explained. They are separated into the 94-95 and the 2004 surveys, emphasizing the work done in this thesis. The evaluated responses corresponding to the whole data set are also presented.

7.1 Betics 94-95 Survey

7.1.1 Description

The first magnetolelluric measurements in the Betic Chain were done in the framework of a research project sponsored by the Spanish Education and Science Ministry, with the aim of electrically characterizing the crust in the south Iberian Massif and the Betic chain. The sites were located more or less along a NW-SW profile coincident with previously existing seismic refraction and reflection lines.

The data were acquired in three stages during 1994 and 1995 using three Metronix MS03 instruments, property of the Departament de Geodinàmica i Geofísica of the Universitat de Barcelona (DG-UB).

At each site, the two electric and magnetic horizontal components were registered. The vertical magnetic component was registered only at some sites, given the difficulty of burying the vertical coil in certain terrains. In view of further 2D modelling, the axis orientation of the recorded components at some sites was NE-SW, coincident with the direction of the main outcropping structures of the Betic chain. In total, 41 MT sites, distributed throughout the Central Betics, from the Iberian Massif to the coast, crossing the Internal and External zones and intramontane basins, were acquired (Figure 7.1).

Time series were registered through different bands, with a total duration of three days each. Time series from 21 of the sites were processed using the robust code of Egbert and Booker (1986), resulting in recorded periods ranging from 4 ms to 4000 s.

The sites were labelled as “b” (for “betics”) plus an identification number. Part of this dataset was used to create and interpret a 2D model (see chapter 6, section 6.2.7).

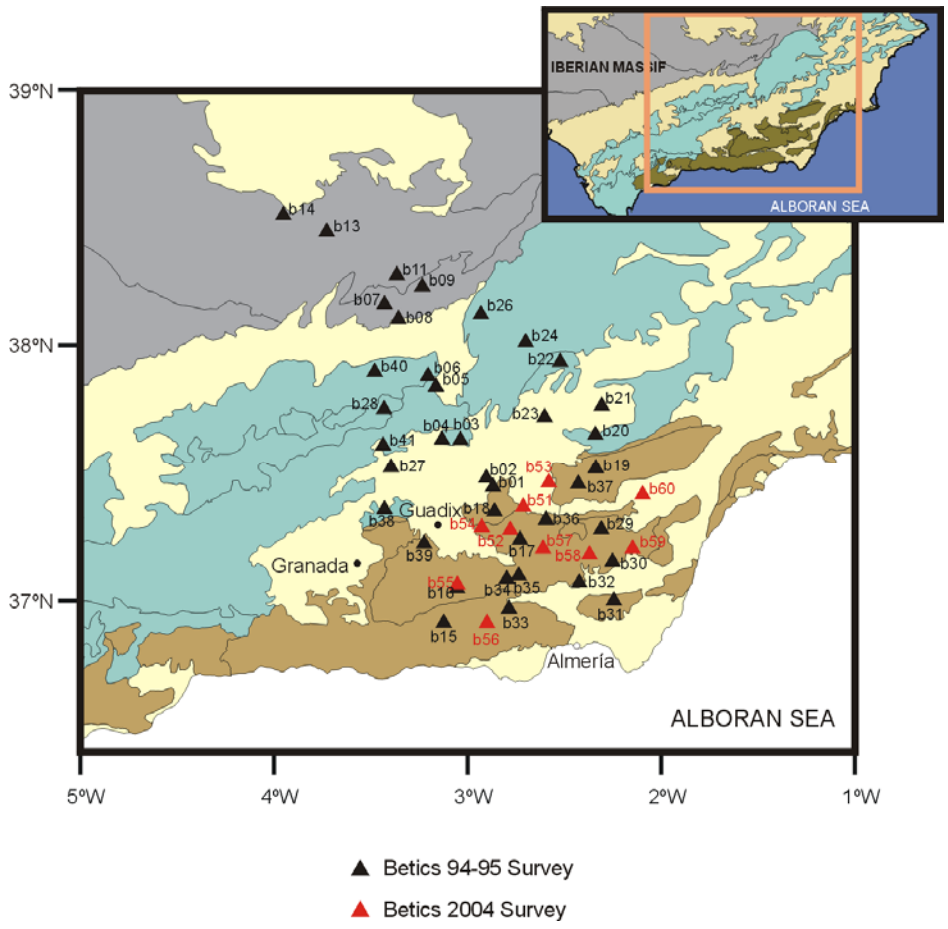

Figure 7.1: Betics sites locations with the corresponding identification, from 94-95 (black) and 2004 (red) surveys.

7.1.2 Time series reprocessing

Although a former dataset with 21 sites from the Betics 94-95 survey existed, reprocessing of the time series and processing of the remaining 20 sites was performed. The aims were to complete the dataset, to obtain a better knowledge of the time series, to have a systematic register of all the processing characteristics and to attempt to improve the quality of the responses, through a careful inspection and selection of the time series segments. Moreover, for further data analysis, especially the dimensionality, it was necessary to establish the same axes directions for all sites, which were set to NS-EW.

The reprocessing consisted of the following five steps, carried out at each site, with the help of specific software provided by Metronix:

1) Restore time series files: Organise time series files in period bands, named band1, band2, band3 and band4 with sampling periods and frequencies: 1 kHz, 32 Hz, 1 s and 32 s respectively (see Table D.2). Band3 and band4 time series can be obtained by resampling the registers of band2 or band3, as long as the recorded ones are not too short and are not low quality.

2) For each band:

a) Visual inspection of the time series and manual selection of the segments (each one containing a determined number of samples) in order to reject contaminated data due to unforeseen incidents (breaking of a wire, digging up an electrode, exhausted batteries…) or to the maintenance of the site. Some indicators of these effects are:

- Signal amplitudes much greater than the average, which can affect only one channel or all channels simultaneously.
- Absence of signal for a certain period of time.
- A period of time with an increase of the oscillation amplitude in all channels.

b) Computation of the MT responses using robust processing (Egbert and Booker, 1986).

c) Data quality check and improvement:

- Bivariate coherences: low values of $E_x(B_xB_y)$ and $E_y(B_xB_y)$ (below 0.8) indicate poor quality data, with a bad correlation between the measured and the predicted fields. Coherence may be improved by the exclusion of more segments in step a).

- Errors: large error bars in the computed responses are undesirable. They can be reduced by the addition of new segments to the selection made in a), such that the confidence limits of the responses become more restricted.

Obviously, a compromise must be achieved regarding the final number of segments, so that the responses present acceptable coherences and only moderately large error bars.

Alternatives that may work to improve the quality of data from long period bands (band3 and band4):

- Perform time-to-frequency conversion using different segment lengths, in order to dispose of a greater number of segments. However, a consequence of this is that the longest periods cannot be estimated.
- Generate new time series by resampling the time series from shorter period bands (band2 and band3).

3) Attach responses from different bands to construct the complete spectrum.

4) Rotate data to N-S direction for those registered with a 45^{o} orientation.

5) Convert output files to EDI (Electrical Data Interchange) format files, which is the SEG Standard for Magnetotelluric Data.

A worksheet was created to store relevant information about each site:

a) site information and equipment configuration: site location, acquisition date, axes orientations, electrode distances and recorded components.
b) time series: data files, recording lengths and channel amplifications.
c) time series processing: number of selected segments, and name of the output files.

Additional comments, such as problems with the initial files, missing data or particular characteristics of the time series processing were also noted in the worksheet.

As an example, Table 7.1 displays the worksheet corresponding to site b01. At this site, five components were recorded (E_x, E_y, B_x, B_y and B_z), with a NW-SE orientation. Data from all bands were restored directly from the registers, without making any posterior resampling of the longest periods bands.

a) Site information

	Geographical coordinates						
Site	Latitude	Longitude	Altitude (m)	Acquisition date (day/month/year)	Measurement orientation (x - y axes)	Electrode distances (m)	TIPPER??
b01	+37:26:31	-2:52:07	1240	31/01/1994 to 02/02/1994	NW-NE	100	YES

b) Time series information

Time series*.03e files	Recorded bands at each file	Total number of segments at each site	Site gains
_1.03e	1,2,3,4	4650	100
_2.03e	3,4	1990	100
_3.03e	1,2	2995	100
_4.03e	1,2,3,4	5910	100
_5.03e	1,2	3170	100
_6.03e	1,2,3,4	6395	100

c) Time series processing

Number of segments per canal(containing 512 samples each) and total recorded time

Band1	Band2	Band3	Band4
100 (51.008s)	315 (83m 56s)	211 (29h 58m 4s)	14 (30h 9m 4s)

Total selections per canal

Band1	Band2	Band3	Band4
47	85	41	12

Output file: b01ss2t.spe

Table 7.1 Site b01 information stored in the worksheet, as an example of the information entered for all sites.

An important number of segments of the time series recorded at this site exhibited noise effects, as expected due to the proximity to populated areas. After a visual inspection and selection of bands 1, 2 and 3, which originally had a large number of segments, a sufficient number of segments prevailed for the posterior robust processing and estimation of the transfer functions.

The selection for band4, with only 14 recorded segments, was not as accurate and hence, only the 2 worst segments were rejected. Otherwise, there would have not been enough data to process and the error bars would have been even greater than they are (see Figure 7.3). However, it did result in low coherence values.

Figure 7.2 and 7.3 show the bivariate coherences and the non-diagonal resistivity and phase responses estimated for site b01, after a 45^{o} rotation. Coherence values are locally lower

than 0.8 for E_x and for T > 40 s for E_y. Nevertheless, resistivity and phases responses have a smooth behaviour, with the exception of a peak near T=10 s, which is especially evident at the yx phase. Error bars are not significant until T=100 s, when these become important, as a consequence of the lack of enough segments at band4 to make a more accurate estimation of the responses. For further analysis of the data, the peaks in the responses must be removed, which will make the data quality acceptable.

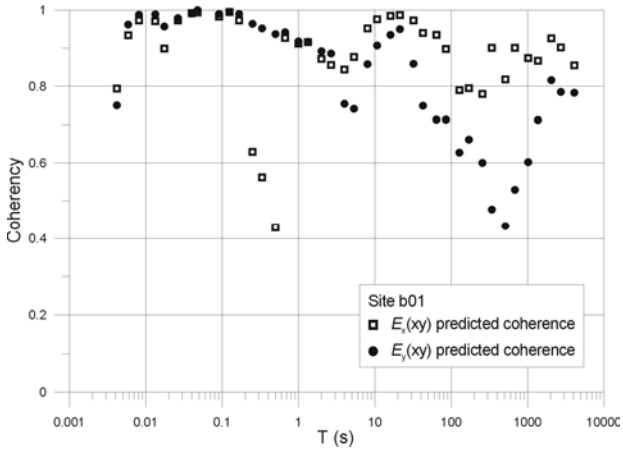

Figure 7.2: Bivariate coherences for the horizontal components of the electric field corresponding to the estimated responses of site b01.

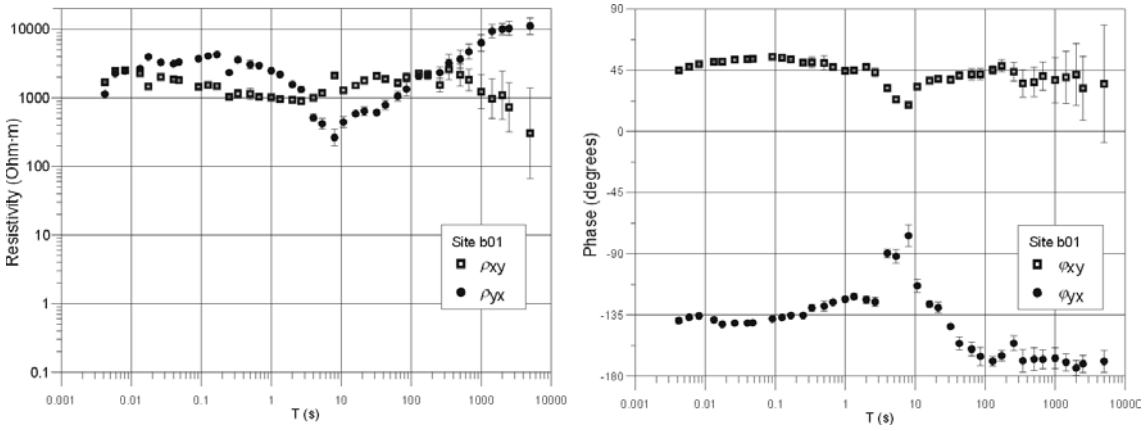

Figure 7.3: xy and yx resistivity and phase responses with their error bars estimated for site b01.

For the remainder of sites, the configuration of the equipment was the same, with the exception of the axes' orientations, the distance between electrodes and the registering or not of the vertical magnetic component. The recording times were similar too, with the time series

displaying the same amount of noise, and in general leading to similar proportions of selected segments. The main differences were in the processing of the longest bands, which in some cases needed different trials regarding the choice of the segments and resampling of the time series, such as to improve data quality. However, at some sites the quality of the data was so low that they had to be rejected from the dataset, which was subsequently reduced to 33 sites.

7.2 Betics 2004 Survey

Given the availability of new MT equipment at the DG-UB, and with the aim of acquiring new data in the study zone, a new MT survey was proposed and executed in the Internal Zone of the Betics during two weeks in the summer of 2004.

7.2.1 Acquisition

The Betics 2004 survey was conducted as a collaboration between the DG-UB and the Departamento de Geodinámica of the Universidad de Granada (DG-UG), using the new Metronix GMS-06 equipment, one belonging to DG-UB and two from the DG-UG.

GMS-06 equipment use the ADU-06 data logger and FMS-06 coils. Compared to the older equipment, ADU-06 allows obtaining high quality data due to 24 Bit Analog/Digital conversion technology, MFS-06 coils are sensitive to a broader range of frequencies (from 0.00025 Hz to 10 kHz) and come with an electronic system to reduce noise levels. This new equipment also permits one to perform remote reference acquisition much more efficiently, due to GPS synchronisation.

The survey area extended from the east of Granada to Almeria, crossing the Nevado-Filábride and Alpujárride complexes, the lowermost of the Internal Zone, and the surrounding basins. Since the area has a marked relief and due to man-made noise, an important task was to carefully locate the sites, to avoid as much as possible the acquisition of noisy data.

The horizontal components of the electric and magnetic fields and the vertical magnetic field (at all except one site) were recorded. The average duration of the registers was two and a half days, in which bands HF, LF1, LF2, Free (with a sampling frequency of 512 Hz) and LF3 were recorded (see chapter 1, Table 1.1, and Table D.2 for comparison with the older system). Band LF4 was obtained from posterior resampling of LF3. At each site, a first test run was performed as a check-up of the equipment. For the shorter bands, HF and LF1, several tests were performed as data backups.

In total, data from 10 sites were acquired (Figure 7.1), identified from b51 to b60. All sites were at new locations, except for b55, which was coincident with the location of a site

from the former 94-95 survey, b16, whose quality was poor with only the short period responses recovered. Apart from improving the information of this site by registering longer time series, the purpose of repeating this measurement was to compare the efficiency between the new and old equipment. The recordings at sites b52 and b57 lasted one week each, in view of using these data for remote reference processing.

Table 7.2 shows part of the worksheet created, containing information on the duration of the recordings at each site, the equipment used and comments on the acquisition runs performed. This table allows one to easily find which of the simultaneous recordings are possible for remote reference processing. Since it was not possible to perform simultaneous recordings of the shorter bands, only LF3 and LF4 could be considered for remote reference. Details of the site coordinates and registered components are also displayed in Appendix D.

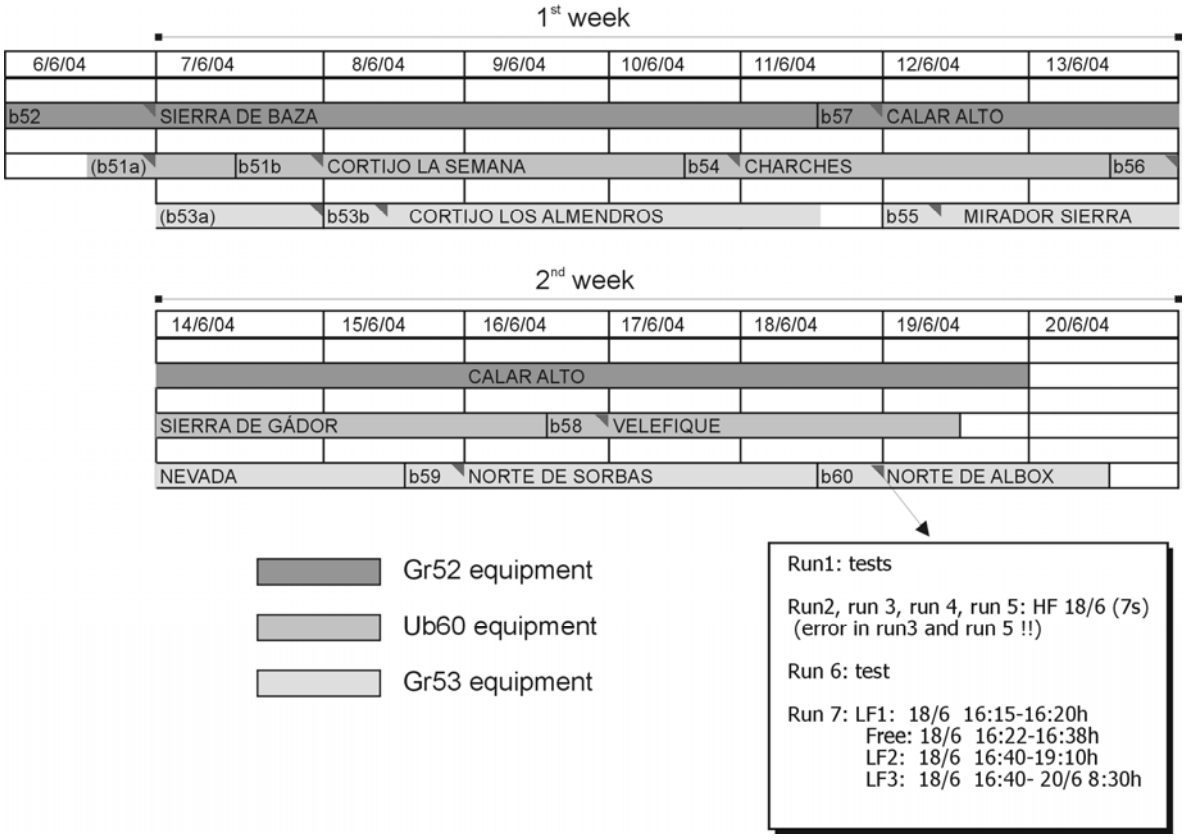

Table 7.2: Information on the Betics 2004 survey sites: dates and duration of the recordings, equipment used and comments (only an example from site b60 is shown) on the different acquisition runs and recorded bands. Comments are placed on the triangle marks.

7.2.2 Time series processing

The acquired data were processed using robust processing from the new version of the Metronix processing software, Mapros (Friedrichs, 2003). The scheme followed was similar to the one used in the former survey, with the difference that most of the steps can be performed automatically by the program.

Inspection of the time series segments revealed the presence of noise at some segments. Particularly, the 50 Hz signal from the power lines could be observed at all sites, which was more intense in those data collected on mountainous terrains than in basins. As it has been observed in previous surveys in other zones, it is common that noise is easily transmitted by irregularities in the terrain. The influence of this signal is reduced in the processing.

For each band, the time series processing was performed in various ways, from which the optimum was chosen. These included making a manual selection of the segments or allowing the program to do it automatically, using different segment lengths, which imply obtaining a broader or narrower spectrum of responses, changing parameters of the time to frequency conversion, and, when available, comparing data from different runs.

Although automatic selection of segments is quite accurate, a visual inspection and manual selection of the segments was always performed, which significantly improved the coherence values.

- HF responses presented very low quality at all sites, due to the low intensity of the natural signal; thus, acquisition using Controlled Source would have been preferable. Responses were not smooth along the period and coherences had very low values. For this reason these frequencies were not included in the final responses.

- LF1, Free and LF2 responses are the best quality responses, with coherence values above 0.8 for LF1 and Free and above 0.6 for LF2, with small error bars and smooth curves for all responses.

- The quality of LF3 and LF4 responses changed from site to site. In some of them, these tests were performed in different ways: either to do more accurate selections of segments or change the time window of the segments. However, there was no significant improvement in the results. In general, the coherence values are low, decrease along with the period and error bars become important for band LF4.

- Remote reference processing (RR) was also tested among sites with simultaneous registers of bands LF3 and LF4, the ones that presented worst quality responses. The use of RR improved the smoothness of the responses at band LF3, although coherence values decrease, whereas both band LF4 responses and coherences worsened. This observation suggests that the separation between sites to apply RR was enough in LF3, but not in band LF4, where a greater separation would have been more desirable. Hence, since only the quality of LF3 improved partly, all the final responses used local reference.

As for the sites recorded in both surveys with the same location, b16 and b55, their coherence values are shown in Figure 7.4. b16 responses could only be estimated up to 10 s, since long period bands recordings were too short and highly affected by noise, and presented low coherences. Site b55 recordings were longer and responses were estimated up to 4000 s, although band LF4 responses were rejected for presenting low coherences and large error bars. Coherence values up to 10 s are similar to those of b16. From 10 s to 100 s (band LF3) their values are slightly increasing. The low values of coherences observed in both sites reflect that noise is inherent to the site, as it does not depend on the equipment.

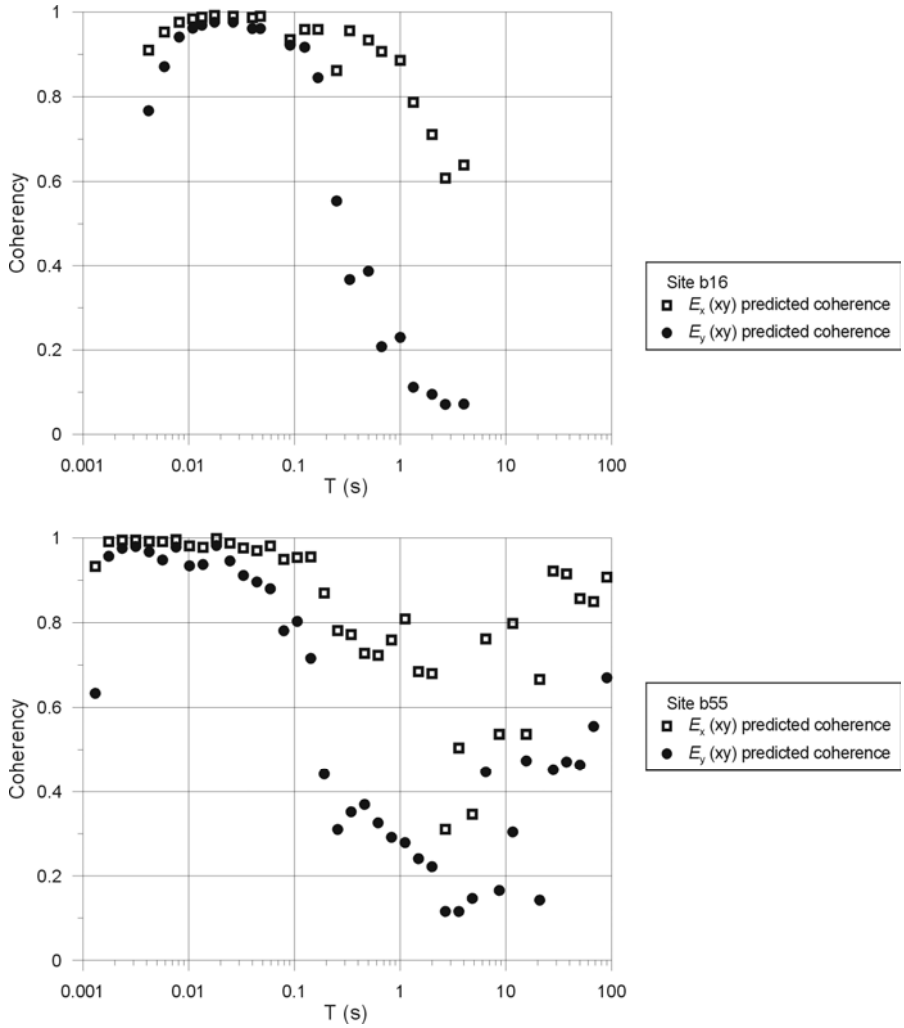

Figure 7.4: Bivariate coherences for the horizontal components of the electric field computed from sites b16 and b55.

7.3 Evaluation of MT Responses

The information about the Betics dataset sites and the MT responses evaluated are displayed in Appendix D (Table D.1 and Figures D.1 to D.9).

The quality of the responses at each site was evaluated following a proposed criterion based on coherences values and errors of the MT tensor components, in the way that high coherence values and small errors are synonymous of good quality.

According to this criterion, there are three sites with poor or very poor quality: sites b09, b38 and b02, the latter due to low coherences, since resistivity and phase curves do not apparently show large error bars. For the rest of Betics 94-95 survey sites, the average qualities are medium and good, and b26 and b30 qualities are very good, as can be seen from the response plots (small error bars).

For sites b51 to b60, with medium and low coherence values, especially for the longest periods, but with moderate error bars, the data quality is regarded from medium to good.

Some of the ρ_{xy} and ρ_{yx} resistivity curves show a displacement, smaller than one decade in value (with the exception of site b52 where it is larger), beginning at the shortest periods. These displacements can be considered static shifts and must be corrected. In general, the variation of the starting resistivity values between sites located over the same area is no greater than one decade.

Apart from the static shifts, it is quite common in the Betics 94-95 sites that the resistivities estimated at the first period present a considerable displacement with respect to the rest of the values. This is a consequence of a problem in the software used on the determination of the responses and, consequently, this period was rejected.

Through an inspection on the shapes of ρ_{xy} and ρ_{yx} plots, which provide a first approach to the variations of underground resistivity with depth, a classification of their morphologies was made, which could be fairly well associated with their locations. The results, in terms of the general behaviour of the different zones, explained from north to south, are:

- Iberian Massif (b14, b13, b11, b09 and b07): smooth resistivity curves for both polaristations, each site with a different constant value, between 10 Ω·m and 1000 Ω·m. The exception is b11 with a drop of ρ_{yx} at the longest periods.
- Guadalquivir basin limits (b08, b06 and b05): split between ρ_{xy} and ρ_{yx} increasing curves.
- Prebetic zone (b26 and b24): constant curves around 100 Ω·m, with a slight drop at intermediate periods.

- Subbetic zone (b40, b03, b20 and b41): b40 and b03 curves have an increasing tendency. b41 resembles more of a basin behaviour, and b20 has a completely different curve, decreasing from 10 Ω·m to 1 Ω·m at 1s, at which point it becomes constant.
- Guadix-Baza basin (b21, b23, b27, b02 and b01): smooth variations of resistivity along a more or less constant curve.
- Internal Zones and surrounding basins (coloured triangles in Figure 7.5): north and south of the Nevado-Filábride complex outcrops (b38, b39, b01, b02, b53, b37, b19, b60, b15 and b32; blue in Figure 7.5), the responses are fairly constant. In the east and west sides of this complex (b18, b30 and b59; yellow in Figure 7.5), the resistivities are increasing at the shortest periods, until reaching a maximum and then drop uniformly. In the NW and SE (b51, b36, b56, b33 and b31; green Figure 7.5) there is a split between xy and yx curves, where ρ_{xy} remains constant and ρ_{yx} decreases. All sites located over the Sierra de los Filabres (b54, b52, b17, b57, b29, b58, b55 and b35; red Figure 7.5) have continuously decreasing resistivity curves. The disposition of the shapes of the resistivity curves around a central part, where a drop in both ρ_{xy} and ρ_{yx} is observed, suggests the existence of a 3D conductive structure confined under the Sierra de los Filabres.

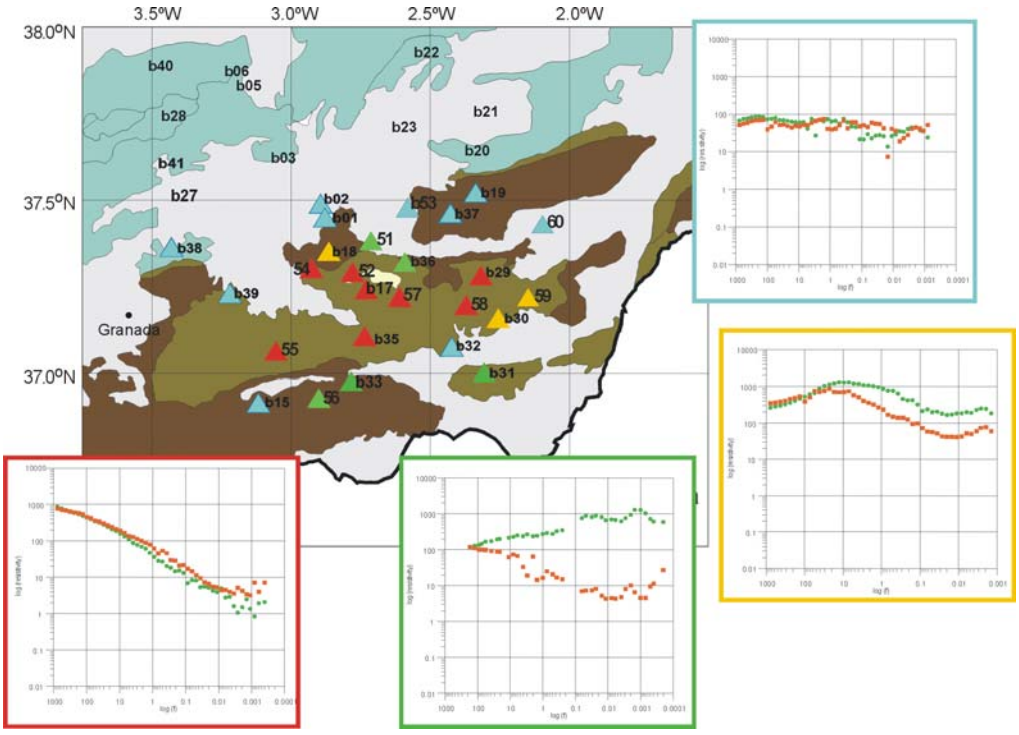

Figure 7.5: Internal Zone and surroundings sites, whose resistivity curves can be classified in four different morphologies, shown in different colours.

The phases corresponding to these curves are consistent with the resistivity variations.

7.4 Conclusions

Betics 94-95 survey data were reprocessed, using a visual inspection of the time series segments. The resulting responses had a range of periods from 4 ms to 4000 s, medium to high coherence values, large error bars at the longest periods and some peaks in the response curves. It resulted in a dataset with 33 sites. The quality was maintained at the sites that already presented good quality and it was improved at sites that presented the lowest coherences and largest error bars.

The new data acquired in 2004 (10 sites) are characterised by high levels of noise, low coherences, but medium to high quality responses, ranging from 1 ms to 1000 s or 4000 s, depending on the sites.

Data from the HF band were not included because of the poor quality of the registers. Remote reference processing was successful for band LF3, but not in LF4, where a larger distance between sites would have been necessary.

The resistivity responses evaluated over the Internal Zone show a central part where both ρ_{xy} and ρ_{yx} decrease, which suggests the presence of a 3D conductive body in depth.

Chapter 8: Geoelectric Dimensionality Analysis of the Betics MT Data

This chapter presents the dimensionality analysis carried out for the Betics MT data. The methodology employed was the WAL invariants criteria, through the WALDIM software developed in this thesis. Taking into account the results of this analysis, an interpretation of the geoelectric structures in depth, and strategies for the further modelling are given.

The results are contrasted with those obtained from two other methodologies, the very commonly used Multisite, Multifrequency Strike code (Strike, McNeice and Jones, 2001), which uses the Groom and Bailey decomposition, and the more recently appeared phase tensor method (Caldwell *et al.*, 2004).

The choice of WAL invariants criteria amongst other methods is due to the fact that it utilises all the information from the MT tensor data and provides a dimensionality description not restricted to a specific model. On the contrary, the phase tensor only utilises half of the information provided by the MT tensor (i.e., the phases). The Strike code searches a 3D/2D description of the data, in view of 2D modelling, although it does provide a misfit that allows one to quantify up to which degree this interpretation is suitable.

8.1 WAL Dimensionality Analysis

Even though all processes in the WALDIM program are performed automatically, this section presents the results obtained for the Betics MT data separated in two steps:

(1) WAL invariant values, errors, and related angles and parameters, at different periods and depths.

(2) Dimensionality analysis results and their interpretation considering other structural knowledge of the crustal structure.

8.1.1 WAL invariants and errors, related angles and parameters

Following the recommendations given in section 3.4, the invariant values were estimated as the true values, and their errors were computed using classical error propagation (approach **a** in section 3.2.1a). Strike directions and distortion parameters were also estimated as true values, whereas their errors were computed using random noise generation (approach **b**, section 3.2.1b).

In order to illustrate the values of the invariants used in the dimensionality determination (I_3 to I_7 and Q) and their variation along the different sites, period and depths, different contour maps were constructed at given periods and equivalent study depths.

Contour maps for constant periods, distributed along the whole spectrum (2 per logarithmic decade) were plotted and analysed. Figure 8.1 shows the invariant maps at four constant periods, whose features are representative of the contiguous ones computed.

T=0.0032 s (Figure 8.1a) is the first period in which almost all sites are represented. I_3 and I_4 have a similar distribution, with broad changes from site to site. I_5 values are in general low, with higher values at the outermost sites, whilst I_6 and Q values are low, the latter implying that I_7 values are considered undetermined. At this period, with $I_3 \neq 0$, $I_4 \neq 0$ and $I_5 \neq 0$, $I_6 \approx 0$ and $Q \approx 0$, the dimensionality is interpreted as 3D/1D2D.

At T=0.1 s (Figure 8.1a), with map appearances representative of the period range from 0.01 s to 1 s, the previous description still holds, although with a notable decrease in all invariants' values. Consequently, the dimensionality is less complex, with mixed 1D and 2D cases.

At T=10 s (Figure 8.1b), invariants I_3 and I_4 follow different values distributions, with higher values than at T=0.1 s. I_5 values become larger at the extremes, but still with a low value zone in the middle. I_6 become larger at the northwesternmost sites, whereas the rest remain low. Q has higher values too, so I_7, with low to moderate values, is not considered undetermined. The exception to this is at the northernmost and southernmost sites, with values larger than 1. At this period, dimensionality increases in complexity, with some 3D cases mixed with 2D cases that are affected by galvanic distortion.

T=1000 s contour maps (Figure 8.1b), with a smaller number of sites, presents a significant change with respect to the rest of period maps. All values are considerably higher than the rest, which indicates an increase in the dimensional complexity, which is mainly 3D.

Contour maps at different study depths were built using "Bostick Modified Depth", h_{BM}, based on the Bostick transform (Bostick, 1977) [(1)].

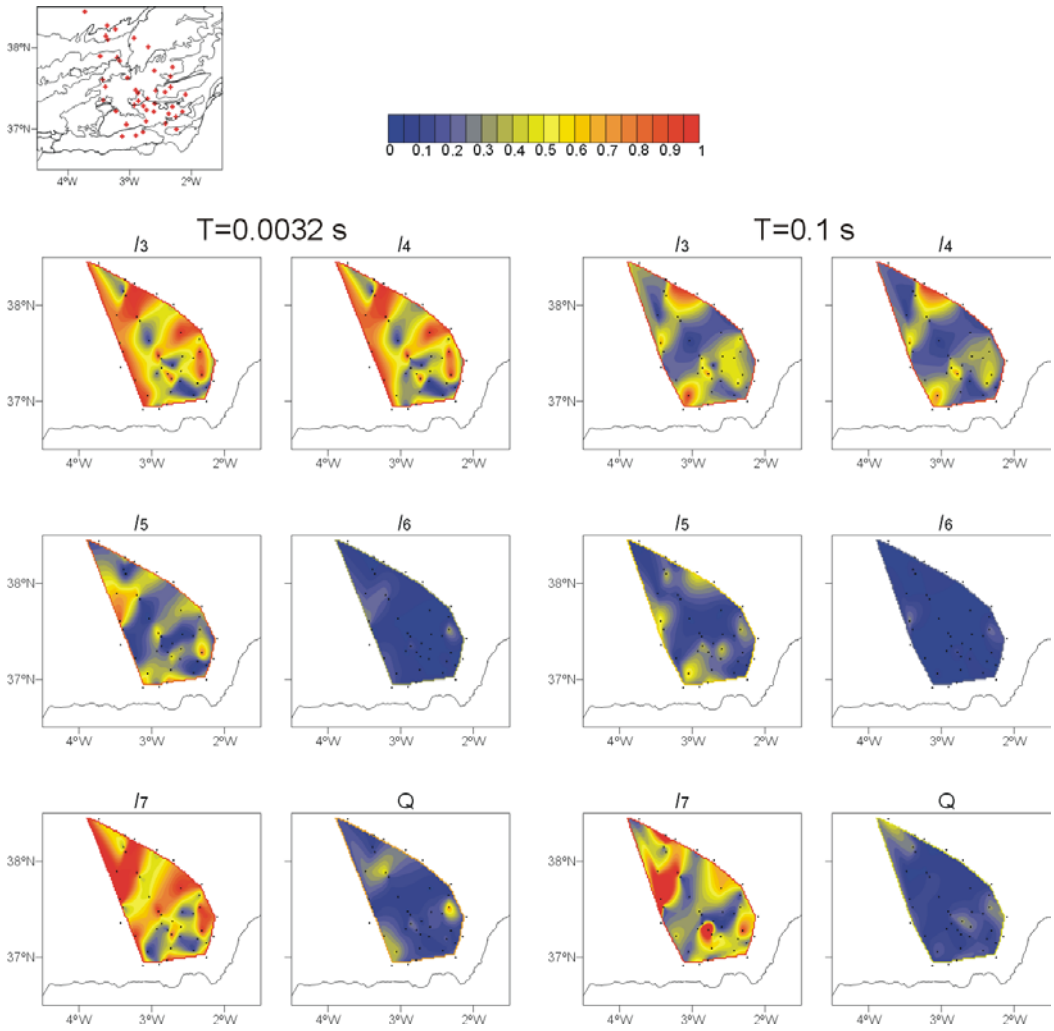

Figure 8.1a: Contour maps of WAL invariants I_3 to I_7 and Q at constant periods T=0.032 s and T=0.1 s. Site locations (black dots) and coastline are given as a reference. Upper left map shows site locations over the main geological features of the study area.

[1] The Bostick transform converts frequency domain resistivity data into a resistivity depth sounding. For each frequency, Bostick resistivity and depth are computed from the apparent resistivity ρ as $\rho_B = \rho \cdot \frac{1+M}{1-M}$ and $h_B = \sqrt{\frac{\rho}{\omega \mu_0}}$, where M is the slope of ρ in a log-log plot. h_B is $1/\sqrt{2}$ times the skin depth, δ. In a layered Earth, h_B can be interpreted as the "centre of gravity" depth of the in-phase induced current systems studied at a given period.

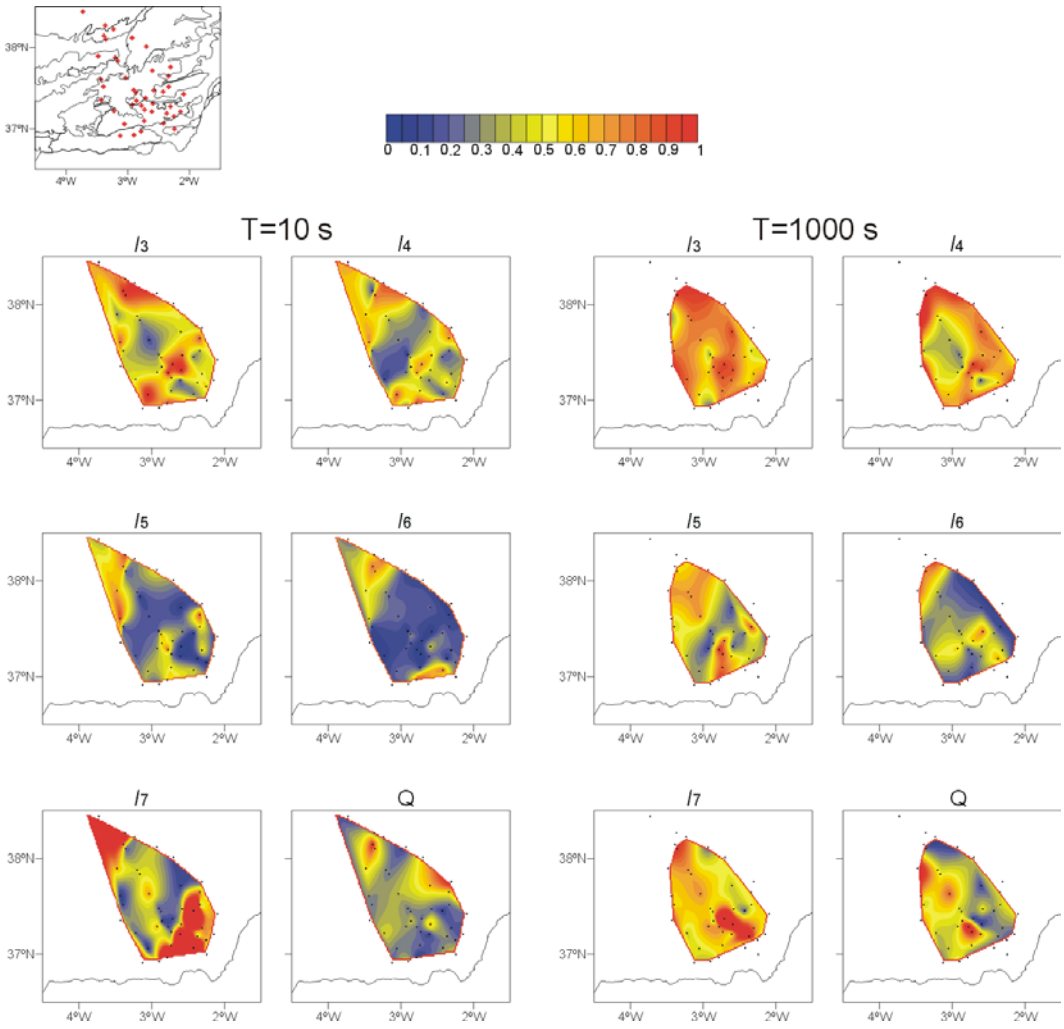

Figure 8.1b: Contour maps of WAL invariants I_3 to I_7 and Q at constant periods T=10 s and T=1000 s. Site locations (black dots) and coastline are given as a reference. Upper left map shows site locations over the main geological features of the study area.

h_{BM} was defined for a given period from the 1D resistivity computed from I_1 and I_2 invariants (eq. 2.20):

$$h_{BM} = \sqrt{\frac{\rho_{1D}}{\omega\mu_0}} = \frac{T}{2\pi}\sqrt{\left(I_1^2 + I_2^2\right)}, \tag{8.1}$$

in m, if I_1 and I_2 are expressed in m/s. The choice of this modified depth has the advantage that utilises a rotational invariant resistivity, and allows mapping the dimensionality related invariant values as a function of the two remaining invariants of the WAL set, I_1 and I_2. However, these invariants, as well as the Bostick depth obtained, may be affected by the static shift.

These contour maps were drawn for different intervals of h_{BM} values, since the dependence of h_{BM} on T, I_1 and I_2 resulted in a broad range of values.

Two of these h_{BM} contour maps, at the intervals h_{BM}=100 m to h_{BM}=120 m (named h_{BM}=100 m) and h_{BM}=10000 m to h_{BM}=12000 m (named h_{BM}=10000 m) are displayed in Figure 8.2, as representative of upper and middle depths.

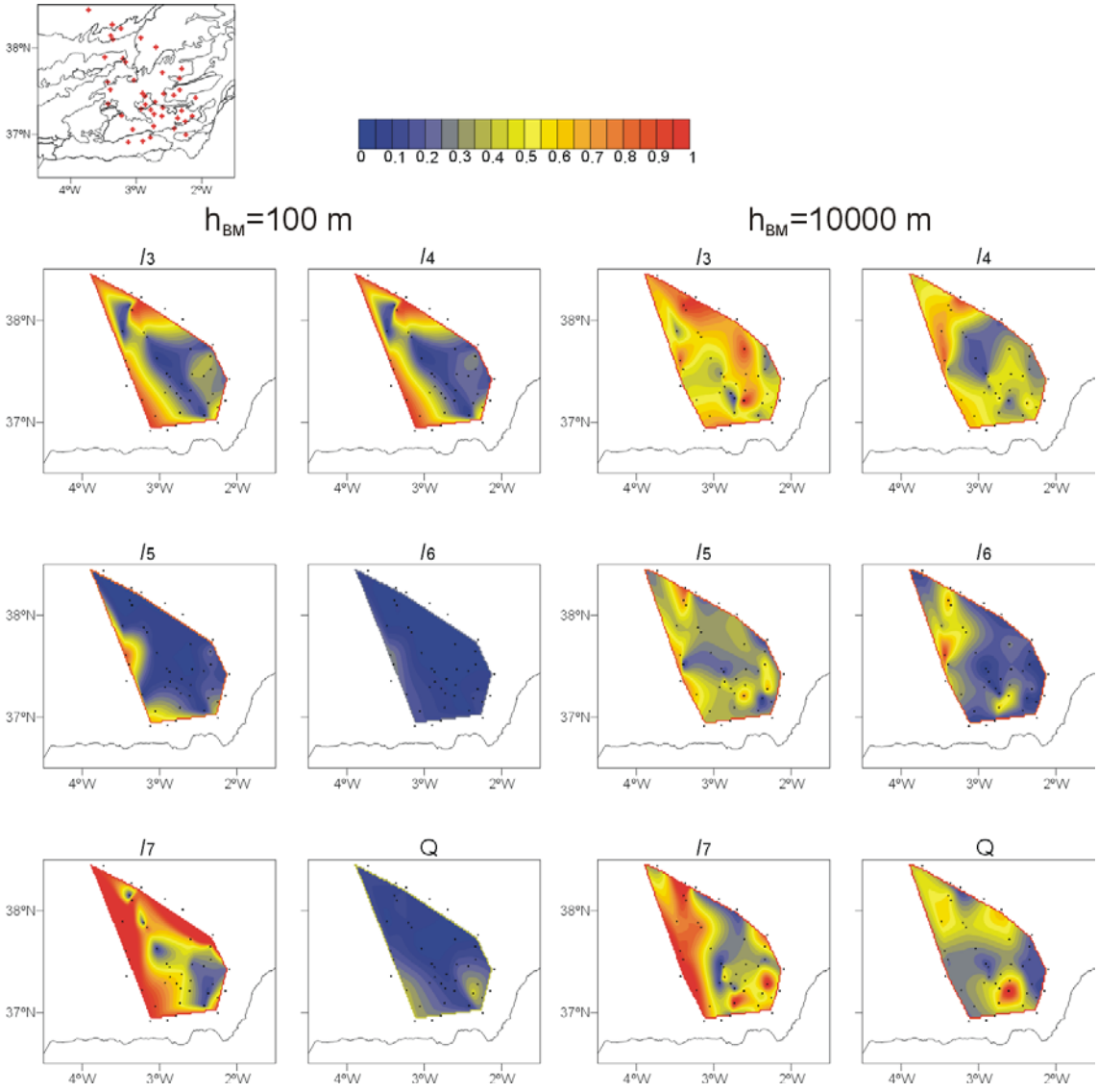

Figure 8.2: Contour maps of WAL invariants I_3 to I_7 and Q at two Bostick modified depths, h_{BM}=100 m and h_{BM}=10000 m. Site locations (black dots) and coastline are given as a reference. Upper left map shows site locations over the main geological features of the study area.

The h_{BM}=100 m map, obtained from 20 sites over two decades (from 0.00175 s to 0.09 s) in general shows similar values of I_3 and I_4, low values of I_5, I_6 and Q; and I_7 is

undetermined, which indicates 1D and 2D dimensionality. However, at the eastern middle and southern edges of the map, I_5 becomes larger, which is interpreted as a twist-distortion; and at the southern part, Q increases, which, together with high values of I_7 indicate three-dimensionality.

The h_{BM}=10000 m map represents 30 sites with an even broader range of periods (between 0.5 s and 1000 s), with most concentrated between 10 s to 100 s. Contrary to the h_{BM}=100 m map, the dimensional complexity is evident, with larger values of all invariants in general, as observed in the middle and long period maps (10 s and 1000 s).

In reference to the errors of WAL invariants, the distribution of the error bars with the period shown at site b23 (chapter 3, Figure 3.3) is in general valid for the rest of the sites. Invariants I_3 to I_6 have error values proportional to the noise level in the MT tensor components, which increase with the period, whereas I_7 and Q errors are large at all periods, especially those of I_7 if Q values are small.

Contour maps of the invariant errors at constant periods follow the above description: up to 100 s, I_3 to I_6 error values are small (<0.1), Q errors are slightly higher (up to 0.4 at some sites and periods) and I_7 errors are large. At longer periods, all errors are large, as it can be seen from the T=1000 s error map (Figure 8.3).

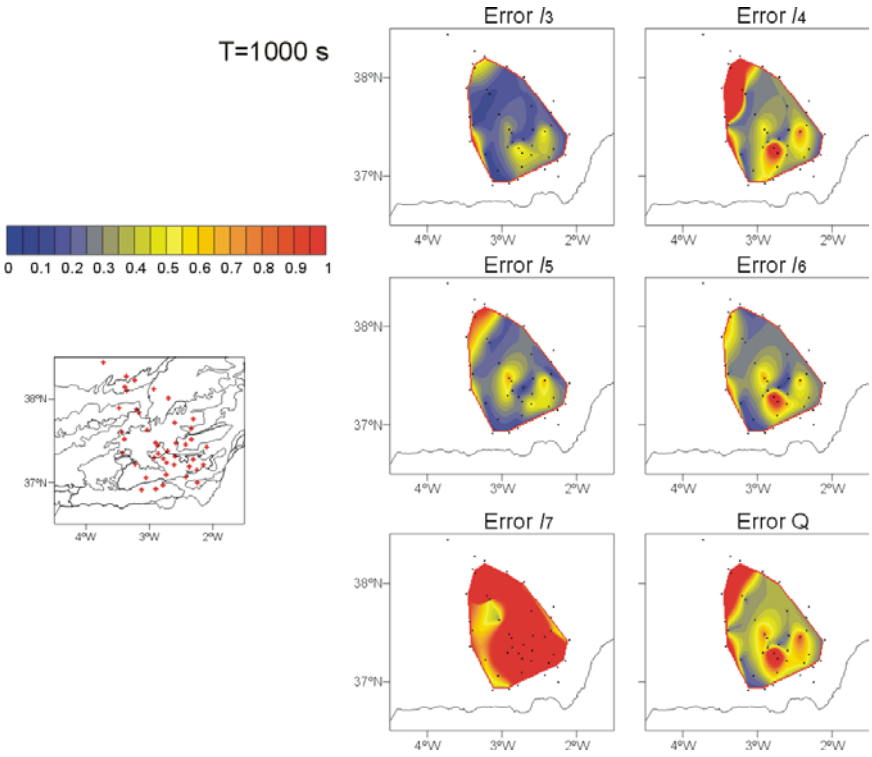

Figure 8.3: Error values of WAL invariants I_3 to I_7 and Q at T=1000 s. Site locations (black dots) and coastline are given as a reference. Left map shows site locations over the main geological features of the study area.

8.1.2 WAL dimensionality analysis of the Betics MT dataset

This dimensionality analysis was carried out for every site and period, using the WALDIM software (chapter 3, section 3.5). The true values of the invariants were estimated and their errors were computed using classical error propagation. For the determination of the dimensionality threshold values τ=0.15 and τ_Q=0.1 were used.

As a preview of the dimensionality results, Figure 8.4 illustrates the dimensionality maps obtained at the same periods used to plot the invariant values (T=0.0032 s, T=0.1 s, T=10 s and T=1000 s). In these four maps there is an ambiguity of 90^o in the determination of the strike direction.

At the shortest period, T=0.0032 s, there is a superposition of all dimensionality cases, without a well-defined spatial pattern. This high complexity at a short period could be caused by local shallow bodies that cause distortion in the measured data. It was already observed in section 3.3 (Figure 3.6), in which the shortest periods displayed a complex dimensionality whereas the data at longer periods were 1D or 2D.

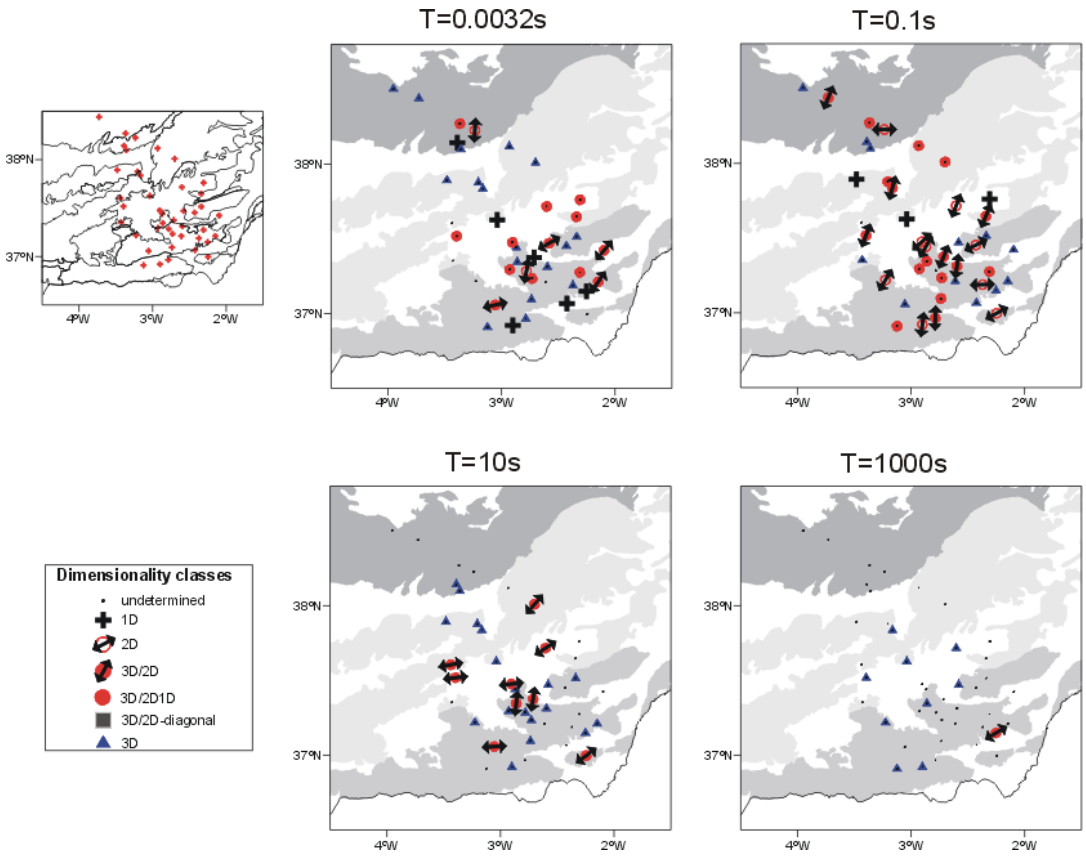

Figure 8.4: Dimensionality distribution according to WAL invariants criteria, for the Betics MT dataset, considering data errors, at four representative periods, T=0.0032 s, T=0.1 s, T=10 s and T=1000 s. Arrows indicate the strike direction, set in the first quadrant. Cases 3D/2Dtwist and 3D/2D are plotted as a single case (3D/2D).

At T=0.1 s, the prevalent dimensionality is 2D, whether affected or not by galvanic distortion, mixed with some 3D/1D2D and 3D cases. Strike directions associated with two-dimensional structures have values around N20^{o}E in the southwesternmost sites and change to values between N60^{o}E and N90^{o}E towards the northeast. The strike determination is good, with small error values (less than 2.5^{o}).

At T=10 s only 3D/2D and 3D cases occur, with an appreciable number of undetermined sites. Strike directions are mainly 0^{o} and N50^{o}E, and the errors are large (up to 20^{o} at some sites).

At T=1000 s, the errors complicate the dimensionality determination, which is reduced to 10 sites, where all but one are 3D.

Considering all periods, the dimensionality could not be determined for thirty percent of the tensors, due to errors, most of them associated with the longest periods.

The dimensionality results (or categories) were grouped at each site in period decade bands (Figure 8.5), in order to represent the prevalent categories and strikes at different penetrations.

The average strike directions with their standard deviations were computed for the bands with 2D and 3D/2D dimensionality. The strike arrows are scaled inversely to the error values. To solve the ambiguity in the determination of the strike direction, the induction arrow information was taken into account when available.

It can be observed (Figure 8.5) that the predominant dimensionality is 3D, with abundant 1D, 2D and 3D/1D2D structures for periods shorter than 1 s and scarcer 3D/2D structures for periods between 1 s and 1000 s.

Up to 1 s (bands 1, 2 and 3, Figure 8.5a to Figure 8.5c), the dimensionality is significantly different between the Iberian Massif, the Betic Chain and the overlying Cenozoic basins. In the Iberian Massif, the structures are 3D and, among these, 2D with strike orientations trending from ENE-WSW to E-W. More to the south, over the Betics, the dimensionality is more complex with 3D/1D2D, 2D, 3D/2D and 3D cases. The bidimensional structures (whether affected or not by galvanic distortion) can be classified into two groups with perpendicular strike directions, one oriented between E-W and WNW-ESE and the other with directions comprised between N-S and NNE-SSW, and a third group, located in the eastern part, with ENE-WSW strike directions. Finally, the sites located over the Cenozoic basins (Guadix and Guadalquivir) are characterised by the presence of 1D cases that are restricted to periods shorter than 0.1 s.

Between 1 s and 10 s (band 4, Figure 8.5d), the structure becomes more 3D. The bidimensional cases are fewer, less precise and located over the Internal Zone of the Betics (southeastern part of the study area) where they also show NNE-SSW and WNW-ESE strike directions.

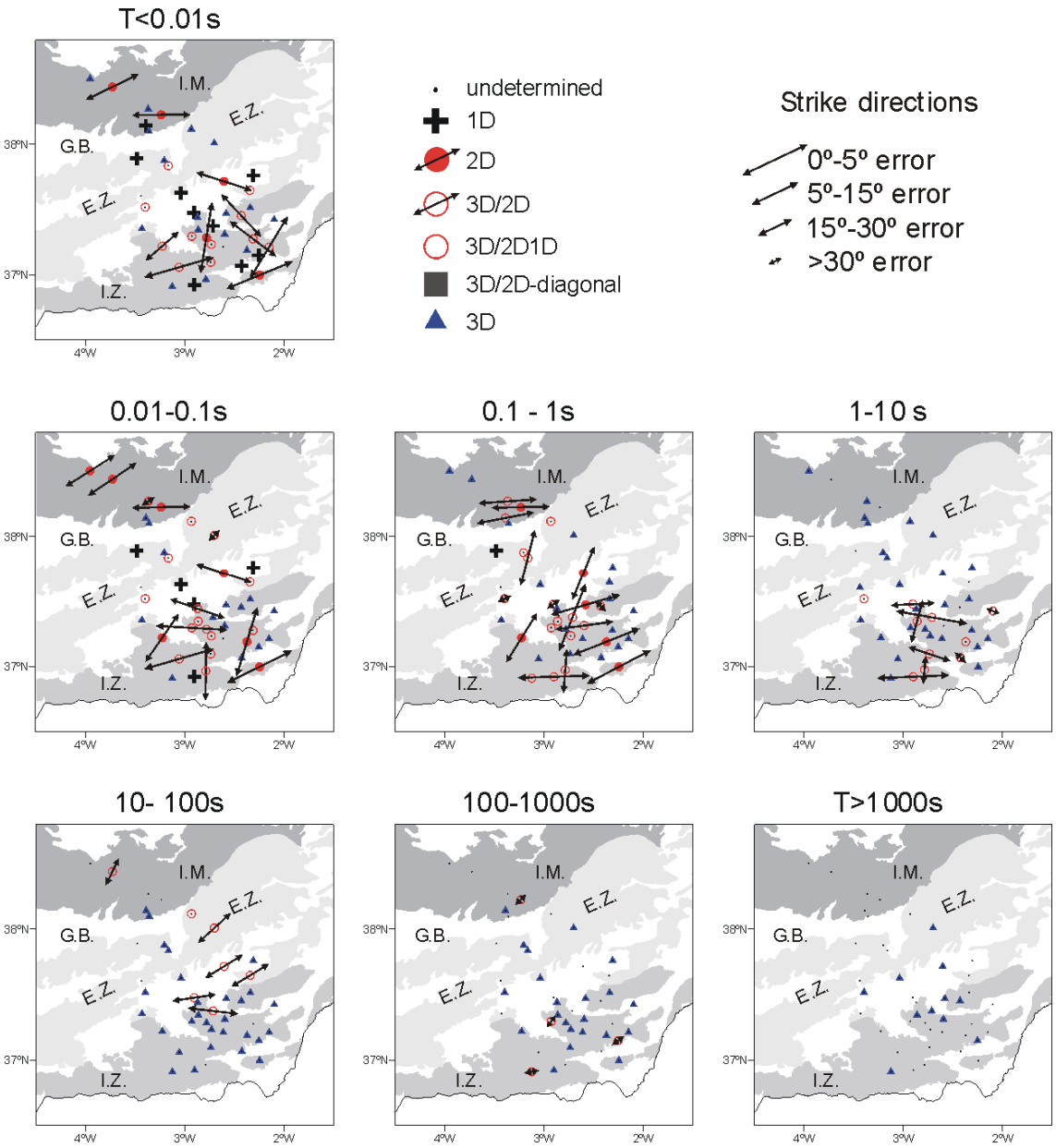

Figure 8.5: Dimensionality results of the Betics MT dataset grouped in 7 period bands. Those cases in which the dimensionality could not be determined are not shown. The arrows indicating the strike directions are scaled by the inverse of the error in the determination of the strike. (a) band 1: T<0.01 s, (b) band 2: 0.01 s – 0.1 s, (c) band 3: 0.1 s –1 s, (d) band 4: 1 s – 10 s, (e) band 5: 10 s – 100 s, (f) band 6: 100 s – 1000 s, (g) band 7: T> 1000 s. I.M.: Iberian Massif, G.B.: Guadalquivir Basin, E.Z.: External Zone and I.Z.: Internal Zone.

These orthogonal bidimensional structures disappear for periods longer than 10 s at the same time that the dimensionality becomes essentially 3D. Despite the predominance of these 3D cases, the presence of periods comprised between 10 s and 100 s (band 5, Figure 8.5e) of relatively abundant bidimensional cases (affected by galvanic distortion) should be noted for the sites located over the Iberian Massif and External Betics. These cases show a strike direction

(NE-SW) which is nearly parallel to that observed for shorter periods in the Iberian Massif. For the longest periods (T < 100 s) (bands 6 and 7, Figure 8.5f and Figure 8.5g), the dimensionality can only be determined at some sites located over the Betic Chain and is in general 3D, with some 2D cases at band 6 (Figure 8.5f) with a high percentage of error.

Discussion

Comparison between the observed geoelectric behaviour and the geological structure of the area denotes a good correlation at upper and middle crustal levels between the changes in the magnetotelluric dimensionality and the kind of deformation affecting the crust. The boundary between the autochthonous Iberian Massif and the allochthonous Betic Chain belongs to a thrust, which dips towards the SSE beneath the Internal Zone and becomes nearly flat at a depth of approx. 5 km beneath the External Zone (Banks and Warburton, 1991). This autochthonous/allochthonous boundary coincides with the most significant change of the dimensionality signature recorded in the analysed data.

Thus, in the allochthonous zones, the dimensionality is highly variable with 2D, 3D/2D, distorted 3D and clearly 3D structures. Further, the strikes show two predominant directions: N-S to NNE-SSW and E-W to WNW-ESE. This signature could be related to the strong Alpine deformation present in this domain which, superimposed upon a previously deformed Variscan basement in the Internal Zone, gave rise to the superimposition of folds and faults of different orientation (Azañón *et al.*, 2002).

Beneath this domain, the upper crustal levels of the autochthonous zone are both 3D and 2D with an ENE-WSW strike. This simpler signature can be correlated with the Variscan structure present in this sector of the Iberian Massif which is characterised by the presence of large E-W to ENE-WSW oriented structural domains (i.e., Ossa-Morena zone) cut by large plutonic bodies with no preferred orientation.

The comparison between this domain and the allochthonous one indicates that the differences of the geoelectrical dimensionality between both domains are related not to the age of deformation but to the major tectonic complexity of the Betic Chain in relation to the Iberian Massif. Whereas the structure of the Iberian Massif is at a large scale mainly bidirectional, the structure of the Betic Chain is characterised by the development of faults and folds which often show changes in direction and are minor in scale.

For the longest periods (> 100 s), in which the inductive length scale is of the same order as the length of the geologic structures, the dimensionality is 3D and it is not possible to distinguish the two domains. The lateral continuity of the conductive body beneath the internal zone in the previous NW-SE 2D model (Pous *et al.*, 1999) is not ensured because the dimensionality obtained is not 2D at a large scale.

8.2 Multisite, Multifrequency Tensor Decomposition Analysis (Strike Code)

Betics MT data were also analysed using Multisite Multifrequency Strike code (McNeice and Jones, 2001). This program performs the Groom and Bailey (G&B) decomposition of the MT tensor data, supported by statistical methods, which can be done in multiple ways: site per site, period per period, for a given group of periods, for a group of sites, fixing some of the parameters or allowing them to be free, etc. In all cases, the strike angle, distortion parameters and the regional tensor (or tensors) are computed. Additionally, a misfit value is given, evaluated from the results and depending on the degrees of freedom of the data considered, which indicates how valid the 3D/2D assumption of the data is.

The final goal of this analysis is to constrain a number of sites within a range of periods in which the data decomposition can be done in view of a 2D model. It means obtaining frequency independent distortion parameters at each site, and a unique strike direction to which to rotate all sites' data. The misfit value is a good tool to determine which these valid sites and period ranges are.

Data analysis using Strike code must be thoughtfully done, as the best fits must be located by the user, supported by the misfit values and other data observations. As an example, site b23 data decomposition was performed, in several ways, and the results compared to those of WAL dimensionality analysis.

In WAL analysis, the error of the MT tensor components was set to a fixed value, to make it comparable to Strike analysis, which utilises a fixed percentage of error in the data instead of using the true data errors. This error percentage was set to 5%. The rest of parameters and options for the WALDIM program were the same as those used in the previous sections.

The Strike program was run with three different settings:

1) Analysis separated in decade period bands, allowing all parameters to be free. Different strike directions and distortion angles were obtained at each band.
2) Analysis of all periods together, all parameters free. One unique strike direction and distortion angles were obtained for the complete period range.
3) Separated analyses in different groups of periods, according to the results from WAL analysis (see Table 8.1, first column):
    a) Up to 1 s (2D according to WAL): assuming a 2D dimensionality, with twist and shear set to zero);
    b) T>1 s (3D/2D, up to 100 s; and 3D, T>100 s): b_1) all parameters free for a single band and b_2) all parameters free, in two groups of periods.

Decomposition results from Strike analysis 1) (Table 8.1) show low misfit values, with the exception of the last band (T>1000 s). The first band (T<0.01 s) has a low misfit, although the strike direction (2^o) differs from the direction obtained from WAL (20^o) and from the decomposition at the next bands (50^o to 60^o). From 0.01 s to 100 s, similar values of twist and shear angles are obtained, with low misfit values, which agrees with a 3D/2D description of the data, although strike directions differ up to 10^o. From 100 s to 1000 s, misfit values are low, so G&B decomposition is valid, although the strike and distortion parameters differ from those of the previous bands.

Analysis 2) leads to a decomposition with θ=60^o, φ_t=0^o and φ_e=-11^o, similar to the results from WAL and analysis 1) from 1 s to 100 s. However, due to the fact that all periods were considered, the misfit is large, which accounts for the fact that all periods cannot be described as 3D/2D with the same strike direction.

In analysis 3a), a strike angle compatible with WAL analysis is recovered, as expected, in good agreement with a 2D description. In analysis $3b_1$), which includes all periods from T=1 s to T=100 s, the same strike and distortion angles as in 1) are recovered, once again with large misfit values, due to the longest periods. On the contrary, analysis $3b_2$) from 1 s to 100 s, the strike and distortion angles are recovered with low misfits, and for T>100 s, a 3D/2D decomposition is obtained, recovering the same parameters as analysis 1) from 10 s to 100 s.

Dimensionality results from site b23 reflected the coincidences and discrepancies between both dimensionality analyses. The Strike program itself showed how it is possible to obtain different decompositions from the same data, since the choice among them depends on a misfit value and not on the real behaviour of the individual MT tensor at each period. At this site, it is not possible to obtain a 2D or 3D/2D description of the data with a unique strike direction. However, when the strike analysis is performed in different bands (e.g. $3b_2$), the results are compatible with WAL.

The principal difference between both methods is that Strike does a global interpretation of a group of data whereas WAL analysis accounts for each individual MT tensor. An important question remains open, that is, to consider whether trying to fit the data to an a-priory description, or to obtain the exact dimensionality information from each MT tensor, even if it does not have a trivial physical explanation.

<table>
<tr><th rowspan="2">Period bands</th><th rowspan="2">WAL analysis</th><th colspan="3">Strike analysis</th></tr>
<tr><th>1) All parameters free - analysis per bands</th><th>2) All parameters free - all periods</th><th colspan="2">3) Two period bands: a) Non distortion b$_1$) Free – one band b$_2$) Free – two bands</th></tr>
<tr><td>T<0.01 s</td><td rowspan="3">2D
$\theta = 20^o \pm 5^o$</td><td>$\theta = 2^o$
$\varphi_t = -1.5^o$
$\varphi_e = 9^o$</td><td rowspan="7">$\theta = 60^o$
$\varphi_t = 0^o$
$\varphi_e = -11^o$</td><td colspan="2" rowspan="3">a)
$\theta = 18^o$</td></tr>
<tr><td>0.01 s-0.1 s</td><td>$\theta = 50^o$
$\varphi_t = 0^o$
$\varphi_e = -9^o$</td></tr>
<tr><td>0.1 s-1 s</td><td>$\theta = 60^o$
$\varphi_t = -1^o$
$\varphi_e = -11^o$</td></tr>
<tr><td>1 s-10 s</td><td>3D/2D
$\theta = 57^o \pm 9^o$
$\varphi_t = 2^o \pm 0.5^o$
$\varphi_e = -9^o \pm 2^o$</td><td>$\theta = 59^o$
$\varphi_t = -0.5^o$
$\varphi_e = -10^o$</td><td rowspan="3">b$_1$)
$\theta = 57^o$
$\varphi_t = 0^o$
$\varphi_e = -10^o$</td><td rowspan="2">b$_2$)
$\theta = 57^o$
$\varphi_t = 0^o$
$\varphi_e = -10^o$</td></tr>
<tr><td>10 s-100 s</td><td>3D/2D
$\theta = 59^o \pm 3^o$
$\varphi_t = 3^o \pm 1^o$
$\varphi_e = -16^o \pm 2^o$</td><td>$\theta = 55^o$
$\varphi_t = -0.5^o$
$\varphi_e = -9^o$</td></tr>
<tr><td>100 s-1000 s</td><td>3D</td><td>$\theta = -17^o$
$\varphi_t = 15^o$
$\varphi_e = 39^o$</td><td>$\theta = -13^o$
$\varphi_t = 12^o$
$\varphi_e = 39^o$</td></tr>
<tr><td>T>1000 s</td><td>3D</td><td>$\theta = -13^o$
$\varphi_t = 12.5^o$
$\varphi_e = 40^o$</td></tr>
</table>

Table 8.1: Results from site b23 WAL analysis (τ=0.15 and τ_Q=0.1) and G&B decomposition, using Strike code: 1) Analysis separated in seven period bands, allowing all parameters free. 2) All periods together, all parameters free. 3) Two different analyses at short and long period bands, according to WAL dimensionality results: a) Short periods, fixing distortion parameters to zero (2D without distortion). b) Long periods, allowing all parameters to be free (b$_1$: one band, b$_2$: two bands). Grey backgrounds indicate large misfit values ($\chi^2/\chi^2_{95\%} \geq 1$, poor agreement between the data and a 2D or 3D/2D description).

For all sites of the Betics MT dataset, Strike code was run following this scheme, considering 5% error in the MT tensor components:

1) Analysis site per site, divided into bands containing one or two periods each, obtaining a different decomposition at each band and site.
2) For the sites with a preferred strike direction for all periods obtained in analysis 1), analysis site per site, fitting all the data from each site to the same distortion parameters.
3) Joint analysis of sites with similar strike directions obtained, fixing the strike direction and computing distortion parameters at each site.

Figure 8.6 shows rose diagrams of the strike directions obtained from analysis 1), for eight sites belonging to the different zones of the study area. These plots allow identification of sites that have a prevalent strike direction (or two perpendicular directions) and, consequently, may agree with a 3D/2D description (sites b14, b23, b55, b56 and b58), or may not (sites b24, b40 and b31). From the complete dataset, sites with a preferred strike direction are shown in Table 8.2.

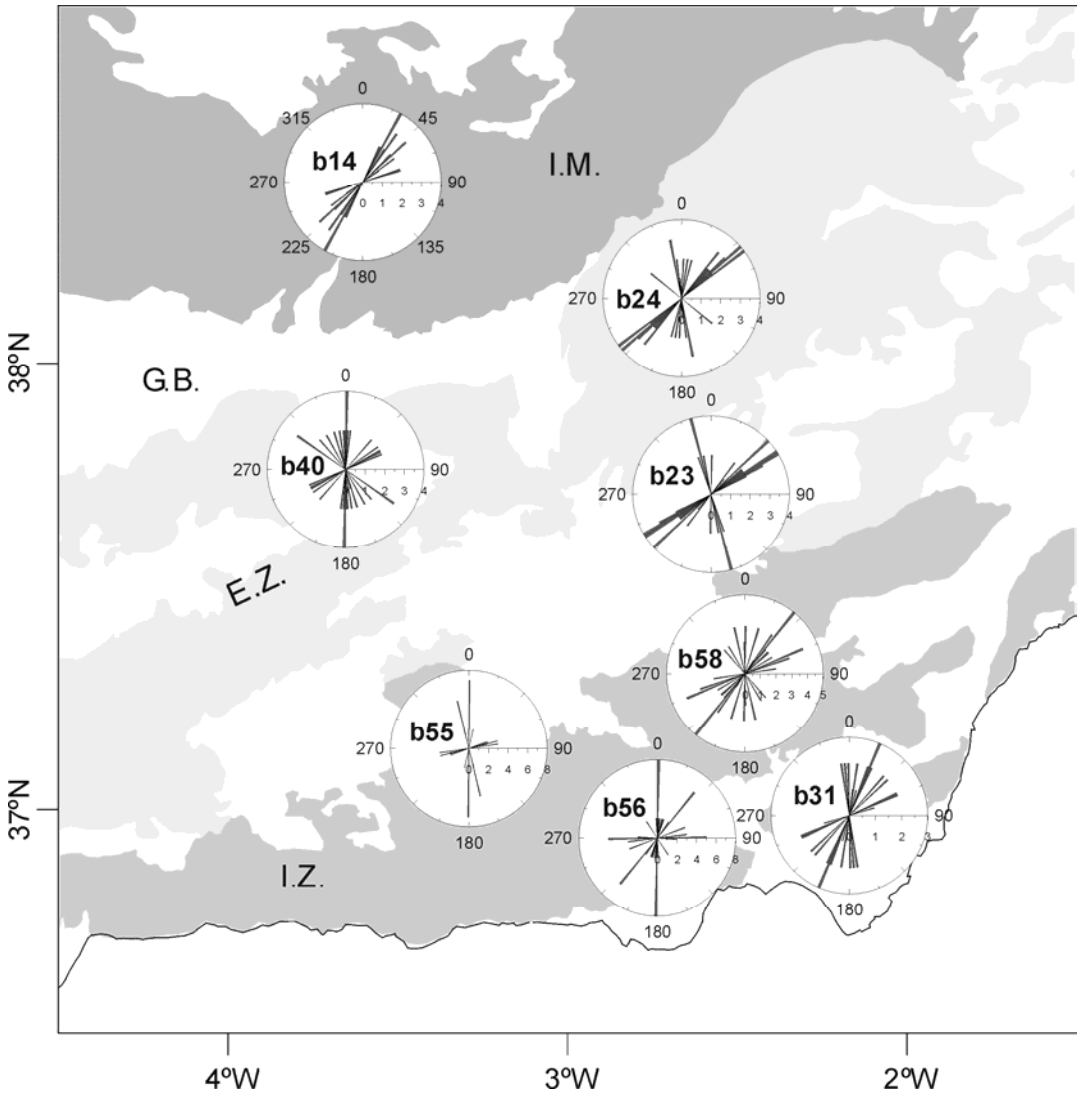

Figure 8.6: Strike directions obtained from Strike analysis 1), for eight sites from the Betics MT dataset, plotted as rose diagrams over the study area.

In analysis 2), the values of the misfits made it possible to corroborate at which sites a 3D/2D assumption is valid (Table 8.2). Only at a few sites is it possible to make a G&B decomposition valid for all periods.

Site	Strike (°)	φ_t (°)	φ_e (°)	$\chi^2/\chi^2_{95\%}$	Decomposition quality ([2])
b31	-5.1 ± 9.6	7.1	-17.1	2	medium
b57	0.0 ± 1.3	6.7	2.3	2	medium
b37	0.0 ± 4.5	6.7	-21.6	1	medium
b01	0.0 ± 5.6	-4.6	-25.0	4	poor
b56	0.0 ± 9.7	0.0	-1.3	3	poor
b08	0.5 ± 7.9	6.5	10.5	2	medium
b35	3.0 ± 9.2	2.7	8.7	6	poor
b39	12.0 ± 2.6	-1.3	-13.2	4	poor
b55	26.0 ± 19.0	-2.0	-33.0	3	poor
b17	28.0 ± 2.0	-7.3	1.7	1	good
b14	34.7 ± 0.3	-3.1	11.0	2	medium
b58	52.0 ± 3.9	1.4	-26.0	0.75	good
b23	57.0 ± 2.0	0.2	-11.0	2	medium
b52	59.0 ± 2.5	1.7	-35.8	0.9	good
b26	62.5 ± 1.0	2.5	-38.8	0.7	good
b20	65.2 ± 10.0	10.0	-17.5	1	good
b09	72.4 ± 0.0	60.0	-42.0	0.025	good
b06	74.0 ± 2.5	-4.5	-25.5	1	good
b19	87.0 ± 1.6	16.0	14.0	3	poor

Table 8.2: Strike analysis 2) results at sites that were identified as possibly 3D/2D in analysis 1). Data has been disposed in ascending Strike value order.

Despite the low misfit values, and given that some of these results indicate a prevalent strike direction (around 0^o or its perpendicular, 90^o), analysis 3) was performed using sites b01, b08, b31, b19, b35, b37, b56 and b57, while fixing the strike value to 0^o, and by separating into period decade bands to obtain the misfit values. The misfit values were substantially greater than in the previous decompositions, given that all sites must fit to the same strike direction, and, since the analysis was performed in period bands, only at a few sites were period independent distortion parameters obtained. Consequently, it seems too restrictive to analyse a

[2] The Strike program computes the misfit of the decomposition according to the departure of the individual data from the decomposition parameters, through a χ^2 test. The program outputs provide the χ^2 values that would correspond to 65% and 95% confidence intervals and the χ^2 values resulting from the decomposition. If χ^2 is smaller than $\chi^2_{95\%}$ the assumption is valid. Otherwise, the quality of the misfit is defined in this thesis as medium (if $\chi^2/\chi^2_{95\%} \leq 2$), or poor (if $\chi^2/\chi^2_{95\%} > 2$).

group of sites with a fixed strike value. The analysis of the individual sites showed better fits, with strike values differing up to 3^o between them.

8.3 The Magnetotelluric Phase Tensor

The phase tensor (chapter 2, section 2.6) was computed from the magnetotelluric tensors of all the Betics MT dataset, as to provide another representation of its dimensionality.

Figure 8.7 represents phase tensor representations and α_p and β_p angles corresponding to site b01, along the measured periods. At this site, according to WAL (τ=0.15) the dimensionality is 3D, with the exception of the period range 0.01 s to 0.1 s, where it is 2D, with an average strike direction of N60^{o}W (Figure 8.5).

The orientation of the phase tensor ellipses (Figure 8.7a) changes smoothly, pointing from WNW at short periods, almost N at middle periods and WNW again at long periods. Discrepancies of 90^o with respect to the strike directions computed from WAL invariants (Figure 3.7) appear, as the phase tensor establishes as strike the direction in which the difference between MT tensor phases is at a maximum. Although not shown, the errors of α_p are moderate at short periods (T < 1 s, $\sigma_{\alpha_P} < 10^o$), and large at middle and long periods(T > 1 s, $\sigma_{\alpha_P} = 10^o$ - 70^o).

A first glance at the ellipses and α_p orientations suggests that the data is 2D, since the ellipses have well distinguishable maximum and minimum axes and are approximately aligned with the direction given by α_p. β_p (Figure 8.7b) has, up to 0.5s, small values and errors, which agrees with a 2D description of the data, with the same strike direction as in WAL (N60^{o}W). At middle and longer periods, β_p is non-zero, with large error bars, which, also taking into account the large errors of α_p, allows one to state that the dimensionality is 3D.

Consequently, to accurately establish the dimensionality using the phase tensor, it is necessary, apart from the analysis of the diagrams, to take into account the values of β_p and the errors.

With the exception of the shortest periods, those up to 1 s, the WAL and the phase tensor descriptions agree well. This discrepancy at the shortest periods lies with the values of I_7, which are not extremely large ($I_7 \approx 0.20$), so a WAL analysis using a slightly larger threshold value would have led to a 2D description (I_5 and I_6 are close to zero), as with the phase tensor description. However, the strike directions θ_1 and θ_2 obtained are significantly different, so a 3D description is more adequate.

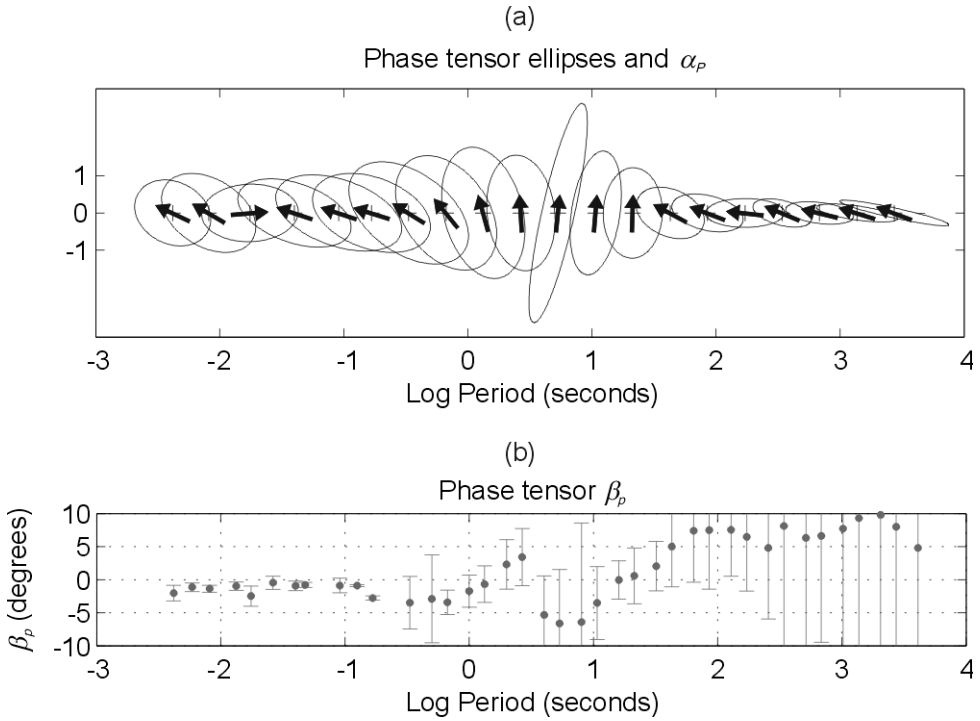

Figure 8.7: Phase tensor representation for site b01 at different periods. a) Ellipses and α_p directions. b) Values of β_p and errors.

Figure 8.8 presents phase tensor diagrams at different periods, representing different period bands, for all sites. Apparently, similar to what was observed at site b01, there is good agreement between the ellipses and the directions of α_p. However, directions change abruptly from site to site and along the different periods, and in general, values of β_p, as well as their errors, increase with the period. Overall, this map provides an image that validates the high complexity of the data.

8.4 Modelling Strategies

The main purpose of data dimensionality analyses is to precisely identify which type of model is required to attempt to reproduce the geoelectric structures below the study area. As for the Betics MT data, these are interpreted to be 1D and 2D at short and middle periods and generally 3D at the longest periods. Those sites with 2D or 3D/2D dimensionalities generally present period dependent strike and distortion parameters. Strike code provided a period independent decomposition of the data at each site, although with large misfit values. Consequently, the wiser option is to endeavour to do a 3D modelling. Since it must be built by forward modelling techniques, the dimensionality information is fundamental in its

construction, as they allow defining the directionality of conductivity structures at some parts of the models or the complexity of these at a certain depth.

Nevertheless, given the time and computing costs of 3D forward modelling, subsets of the data in which the 2D decompositions are not too large and which have similar 2D strike directions, can be used to perform inversions to obtain 2D models perpendicular to the strike, as previews of the final modelled structures.

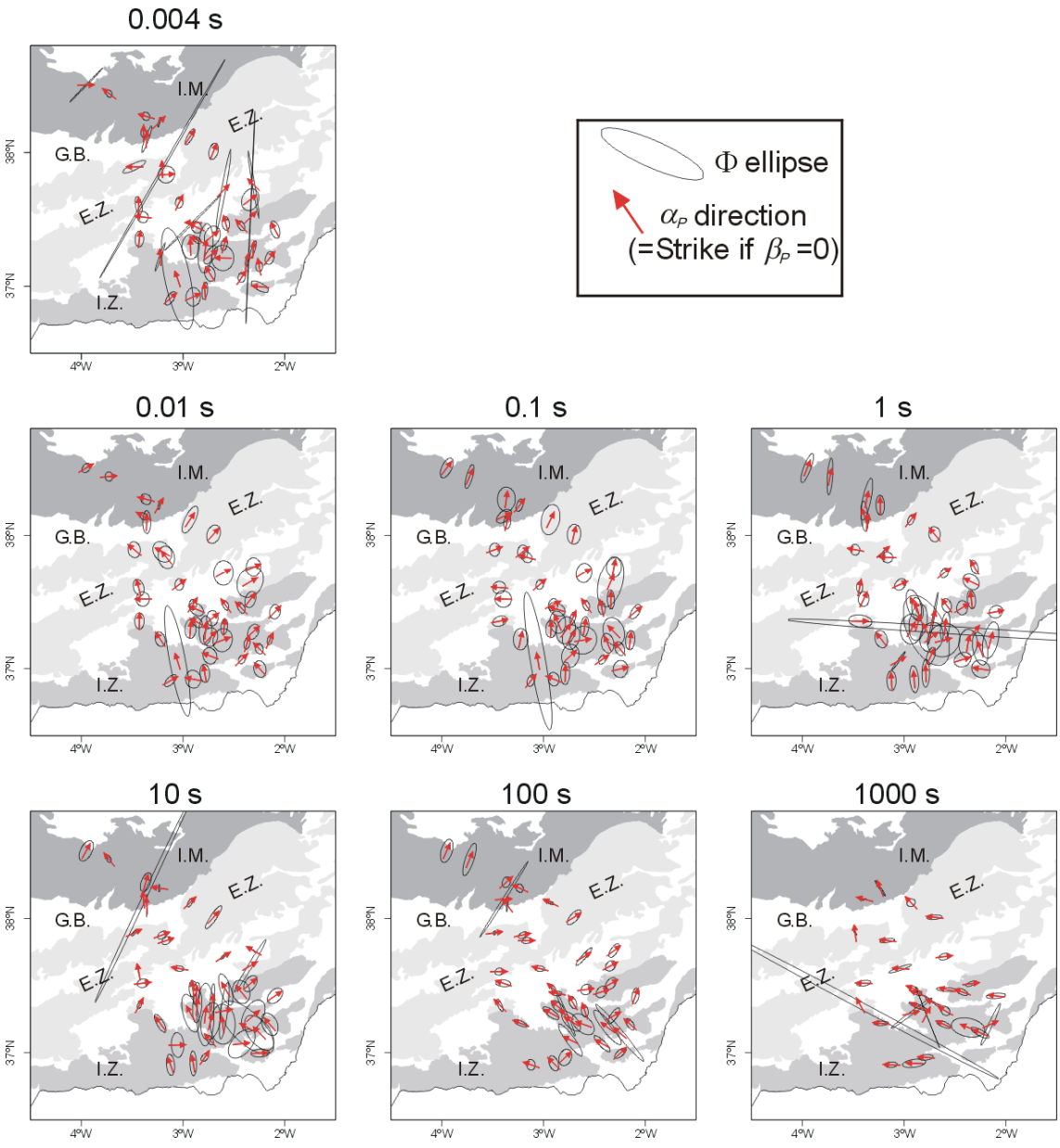

Figure 8.8: Phase tensor maps of the Betics MT data at different periods.

8.5 Conclusions

Dimensionality analysis of the Betics MT data was performed using the WALDIM program based on WAL invariants criteria, taking into account data errors, and with induction arrows complementing the information when available.

The geoelectric structures are mainly 3D, with some 1D cases located over the basins at short periods. Bidimensional structures with N-S to NNE-SSW and E-W to WNW-ESE orientations were found in the allochthonous zones, and with E-W to ENE-WSW orientations in the autochthonous zones. The more complex dimensionality of the Betic Chain is interpreted as being related to the superimposition of processes that took part in its evolution, whereas the Iberian Massif, only affected by the Variscan deformation, shows a simpler dimensionality. The abundance of the 3D structures increases with the period and towards south.

A comparison with other methods showed some similarities but also important discrepancies, a result of the assumptions on which each method is based. G&B decomposition only agrees with the WAL description when this analysis is performed using small subsets of data, and corroborates that the data cannot be described as 2D with a prevalent strike direction. The phase tensor maps of the Betics also confirmed the complex character of the data.

Dimensionality results point at 3D modelling as the best strategy to reproduce geoelectric structures of the Betics, although some 2D models can also be constructed from subsets of the data, which may display a preview of the conductivity structures.

Chapter 9: 2D Modelling

The principal conclusion of the previous chapter is that the dimensionality of the Betics MT data is mainly 3D and that a 3D model is necessary to reproduce the conductivity structures.

However, free 3D inversion software has just been released (Siripunvaraporn *et al.*, 2005, March 2006), and 3D models are still constructed through forward modelling. Meanwhile, 2D inversion is the commonest modelling tool.

In this sense, previous to the 3D modelling, 2D modelling is presented in this chapter. The aims are to do a critical revision of the only prior MT model of the Betics, and also to explore the possibilities of 2D inversion of 3D MT data. In the next chapter, having obtained the 3D model, the limitations of 2D modelling will be demonstrated.

9.1 Sensitivity Study of the Previous 2D Model

The first 2D MT model of the Betics, referred to as MT1 (Pous *et al.*, 1999) was constructed using part of the sites registered in the Betics 94-95 survey (chapter 7, section 7.1), projected over a NW-SE profile. The orientation of the model and the sites to be projected over it were chosen according to the Groom and Bailey decomposition, resulting in a 45^{o} strike, and the induction arrows, which allowed confirmation of the N45^{o}E strike direction and not its perpendicular N45^{o}W. Static shift corrections were applied, such that curves of the sites located over the Internal Betics were shifted up to values on the order of 1000 Ω·m at the shortest periods.

TE and TM responses of 15 sites over the profile, with approximately 38 periods each, were inverted through RRI (Smith and Booker, 1991), and the model responses were computed using the code of Wannamaker *et al.* (1987).

The description of the main conductive (A, B, D and E) and resistive (C) structures identified in the model (Figure 9.1) is found in chapter 6, section 6.2.7.

The dimensionality analysis (chapter 8) pointed to a higher complexity of the geoelectric structures. Below the sites located over the MT1 profile (Figure 9.2) the dimensionality is 1D or 2D at the shallowest depths, whereas at middle and lower depths, it is mainly 3D. Furthermore, the 2D resistivity model is the result of an inversion process, so it is not the only possible solution since other models can fit the same data.

Hence, a revision of the model is necessary in order to discern which is the lateral extent of the conductivity structures and up to which degree the 2D assumption is valid. As a first approach, a sensitivity test of the model was performed.

The purposes of the sensitivity test were to evaluate the sensitivity responses of the 2D model and to check which parts of this model are less sensitive to the recorded data, indicating that they have lower resolution, focusing especially on the lower crustal conductor.

Sensitivity tests (Schwalenberg *et al.*, 2002) are performed to determine how well resolved a model is in terms of its resistivity values and structure, and are generally based on forward modelling in a trial and error style. These tests can be broached from linear and non-linear points of view. The former utilises the sensitivity matrix whereas the latter is based on systematic forward modelling studies and evaluations of the misfits. The linear approach is mainly valid for conductive structures, for which MT responses are highly sensitive to small resistivity variations. On the contrary, given the much lower sensitivity of the MT responses to variations in resistive structures, the non-linear approach is necessary when testing such structures, which must be subjected to large resistivity variations.

Since the aim of this test is to focus on the deep conductive structure, the linear approach was followed. This approach utilises a linear approximation of the sensitivity matrix that contains the partial derivatives of the data responses (2 modes of apparent resistivity and 2 modes of phases obtained at each station at each period) with respect to the model parameters (resistivity values of each model element).

To reduce the number of parameters, the sensitivity of each model element is computed from the normalised sum of the column elements of the sensitivity matrix:

$$s_j = \frac{1}{\Delta_j} \sum_{i=1}^{N} \left\| \frac{1}{\sigma_i} \frac{\partial f_i(m)}{\partial m_j} \right\|, \tag{9.1}$$

where Δ_j is the model element size, σ_i is the error of the response (f_i) and m_j is the model element.

The elements with large sensitivity values are better determined by the data, whereas those with lower values are worse determined and could not be relevant when fitting the measured data. Once the sensitivity values are obtained, the validity of the model can be restricted to the elements with higher sensitivity values.

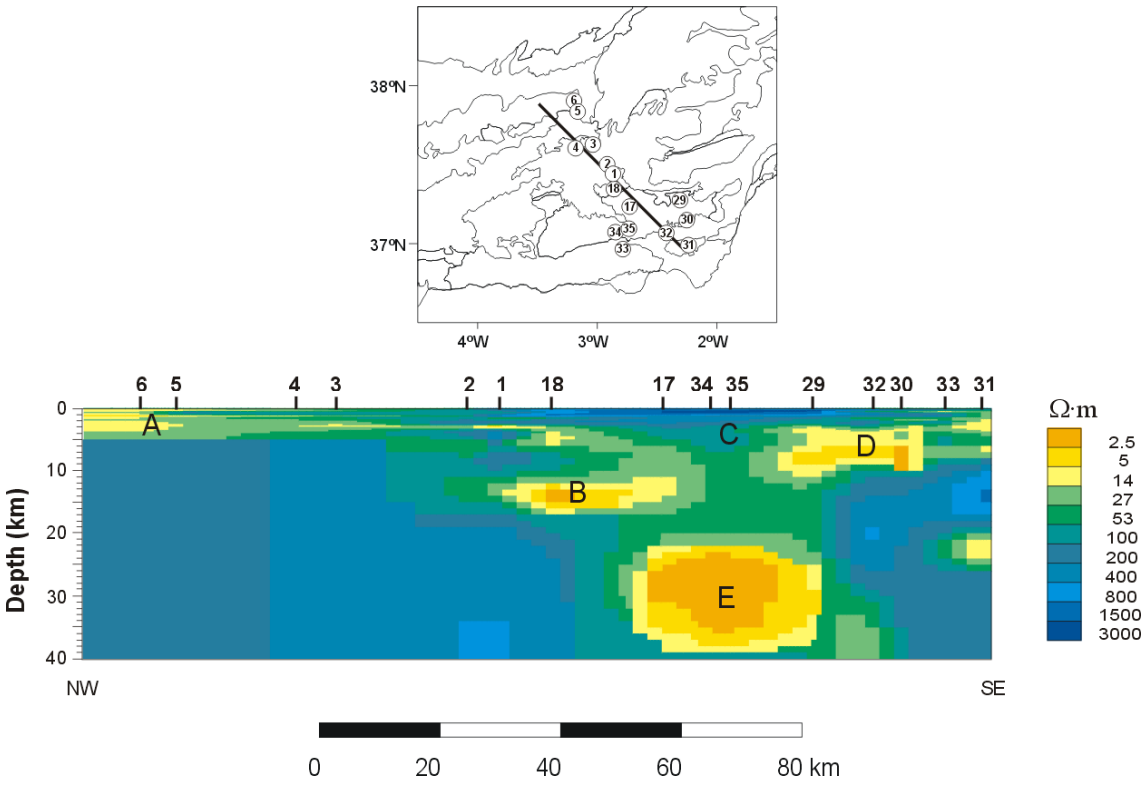

Figure 9.1: MT1 resistivity model. A, B, C, D and E are the main conductive structures identified and interpreted (Pous *et al*., 1999).

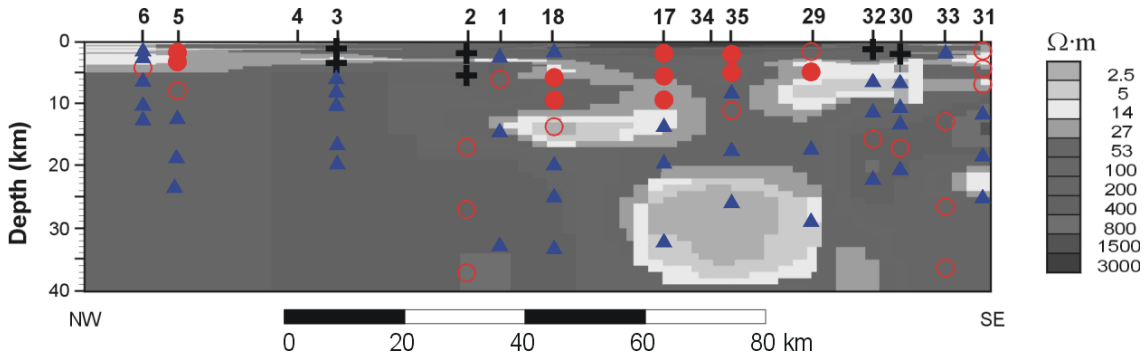

Figure 9.2: Dimensionality of the MT sites along the MT1 profile, displayed over the resistivity model. Dimensionality cases are period-averaged converted into Bostick-depths (see chapter 8, equation 8.1), including the static shift corrections. ✚:1D; ○: 2D or 3D/2D; ●: 3D/2D and ▲: 3D.

The sensitivity matrices of the studied model were computed for both TE and TM mode responses and for TE and TM modes separately. Two datasets were considered: the one containing all 15 sites used to create the model; and a second set in which the sites located over the deep conductor (17, 34 and 35) were removed. This second dataset was considered in order to determine whether the deep conductor is only necessary to fit the above sites, which would indicate that this is possibly a local feature, or also to fit the lateral ones.

Considering a sensitivity threshold of 10^{-4} (Schwalenberg *et al.*, 2002; Ledo *et al.*, 2004) for all 15 sites, the sensitivity maps (Figure 9.3) show that the model is well resolved up to 30km, for TE+TM modes and for the TM mode alone. For the TE mode, the model is well resolved up to only 20km, with the exception of the deep conductor, which is more sensitive to this mode than TM. TE mode is more sensitive to the finite strikes of 3D structures (Wannamaker *et al*., 1984) and, since this sensitivity test is based on 2D assumptions, it cannot resolve lateral continuity in the deep conductor.

The removal of sites 17, 34 and 35 from the datasets only modifies significantly the zone below these sites (Figure 9.3), where the sensitivity decreases for all modes, especially at the shallowest depths, coinciding with the resistor C (Figure 9.1). The deep conductor is well resolved too, as expected given the large penetration depths at the resistant body above.

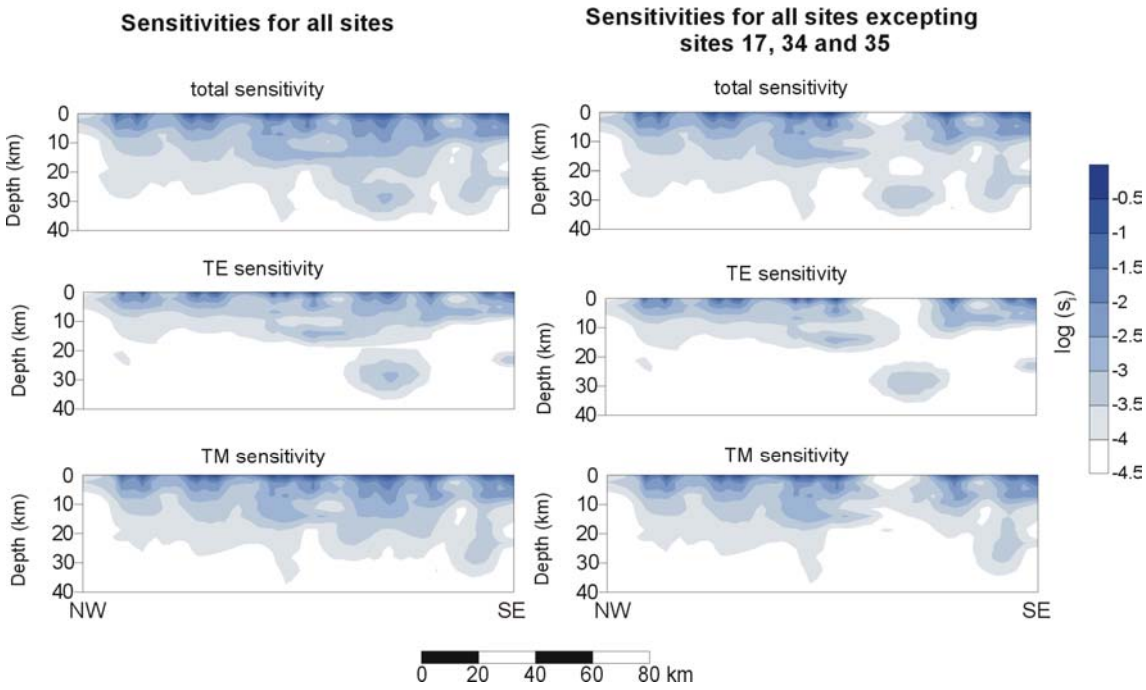

Figure 9.3: Sensitivity values of the 2D model MT1 to the MT responses used in the inversion: TE and TM mode, only TE mode and only TM mode. Left: all sites used in the inversion. Right: all sites but sites 17, 34 and 35 located over the deep conductive body.

The results for both datasets indicate that the presence of the deep conductive body is in deed necessary to fit the data. However, the 3D dimensionality of the data, questions the 2D approach as the most appropriate, and previous studies (Ledo *et al*., 2002) have already demonstrated the problems involved in the 2D interpretation of 3D MT data.

9.2 New 2D Models of the Internal Zones

Using sites from the Internal Zone, the part of the Betics dataset with the highest density of sites, and with more unknowns regarding its conductivity structure (such as the character of the deep conductor) three 2D models were constructed. As already stated, the aims of these 2D models were to obtain a preview of the conductivity structure of the Internal Zone, using inversion techniques, prior to 3D forward modelling.

Three different inversion codes, RLM2DI, REBOCC and DetREBOCC, were used and compared.

9.2.1 Review of inversion codes

RLM2DI code (Mackie *et al.*, 1997) solves the 2D inversion problem using Tikhonov regularization and computes forward responses through finite differences. It allows inverting any of the TE and TM modes resistivities and phases.

REBOCC (reduced basis Occam's inversion) code (Siripunvaraporn and Egbert, 2000) is a variant of the OCCAM algorithm (Constable *et al*., 1987) that allows inverting any of resistivity or phases of TE and TM modes and real and imaginary parts of the Tipper. This code is based on the assumption that MT data are in general smooth and sometimes redundant (if sites or registered periods are too close, although in the Betics dataset this is not the case). Hence, instead of whole datasets, subsets of these are used, which implies a reduction of the size of the sensitivity matrix, without losing details of the model. All these characteristics result in a considerable reduction of memory requirements and computing time.

Pedersen and Engels (2005) propose a routine 2D inversion using the determinant of the impedance tensor, as a variant of REBOCC code, which is here referred to as DetREBOCC. The failure of inverting data that is not truly 2D or that does not have a well-resolved strike direction, decoupled into TE and TM modes, has been largely. Instead, the authors demonstrate that the inversion of the transfer functions (resistivity and phase) related to the determinant of the impedance tensor is a useful tool, as the data are independent of the chosen strike direction, and consequently, of the profile orientation.

The determinant of the impedance tensor is a complex number defined as the square root of the actual determinant (chapter 2, eq. 2.3c, although in that equation it was defined from the MT tensor), thus it has units of impedance (Ω):

$$Z_{DET} = \sqrt{Z_{xx}Z_{yy} - Z_{xy}Z_{yx}} = \left|Z_{DET}\right| e^{i\varphi_{DET}} \text{ , } ^{(1)} \tag{9.2}$$

and the related transfer functions, determinant resistivity,

$$\rho_{DET} = \frac{1}{\mu_0 \omega}\left|Z_{DET}\right|^2, \tag{9.3}$$

and determinant phase, φ_{DET}.

In a truly 2D environment, $\rho_{DET} = \sqrt{\rho_{TE} \cdot \rho_{TM}}$ and $\varphi_{DET} = \frac{1}{2}\left(\varphi_{TE} + \varphi_{TM}\right)$.

The DetREBOCC code utilises data computed from eqs. 9.2 and 9.3 (using all the components of the impedance tensor), while the inversions are carried out using 2D assumptions.

If static shift was corrected at resistivity TE and TM curves, the following approximation was defined to transfer this correction to the determinant resistivity:

$$\rho'_{DET} \approx \sqrt{s_{TE} \cdot \rho_{TE} \cdot s_{TM} \cdot \rho_{TM}} = \sqrt{s_{TE} \cdot s_{TM}} \cdot \rho_{DET}, \tag{9.4}$$

where ′ denotes the corrected value and *s* is the relationship between corrected and uncorrected resistivities. DetREBOCC code can also invert the tipper component, as in REBOCC.

In any of these three inversion processes, RLM2DI, REBOCC or DetREBOCC, the misfit between data and model responses at each step is computed as the *root mean square* (*rms*), whose minimisation is also searched by the inversion algorithms:

$$\left(rms\right)^2 = \sum_{j=1}^{NS}\sum_{i=1}^{NP}\sum_{k=1}^{NVAR} \frac{\left|p_{k,meas} - p_{k,model}\right|^2}{\left|\delta p_k\right|^2}, \tag{9.5}$$

---

[1] $Z_1 = Z_{xx}Z_{yy} - Z_{xy}Z_{yx} = \left|Z_1\right| e^{i\varphi_1}$; $\left|Z_1\right| = \sqrt{X_1^2 + Y_1^2}$ *and* $\varphi_1 = arctan\left(Y_1 / X_1\right)$

$X_1 = Re\left(Z_{xx}Z_{yy} - Z_{xy}Z_{yx}\right) = Re(Z_{xx})\,Re(Z_{yy}) - Im(Z_{xx})\,Im(Z_{yy}) - Re(Z_{xy})\,Re(Z_{yx}) + Im(Z_{xy})\,Im(Z_{yx})$

$Y_1 = Im\left(Z_{xx}Z_{yy} - Z_{xy}Z_{yx}\right) = Re(Z_{xy})\,Im(Z_{yx}) - Re(Z_{yx})\,Im(Z_{xy}) - Re(Z_{xx})\,Im(Z_{yy}) - Re(Z_{yy})\,Im(Z_{xx})$

$Z_{DET} = \sqrt{Z_1} = \left|Z_1\right|^{1/2} e^{i(\varphi_1/2)}$

where p_k refers to the variables inverted (*meas*: measured value, model: model response) and δp_k is the error of the variable, *NS*: number of sites used in the inversion, *NP*: number of periods *NVAR*: number of inverted variables. The decreasing rate of the *rms* accounts for the convergence rate of the inversion process.

Commonly, the *rms* corresponding to the final model is given to quantify the quality of the inversion. It can also be computed for a single site, a determined frequency, a range of periods, and it is usually averaged over the total number of data (divided by *NS·NP·NVAR*).

9.2.2 Two-dimensional profiles

Three profiles were chosen to construct the 2D models (Figure 9.4):

- an east-west profile (termed EW), along which sites b55, b54, b52, b35, b17, b57, b58, b29 and b30 were projected.
- a north-south profile (termed NS1), containing sites from the northern boundary and western side of the Sierra de los Filabres, Eastern side of Sierra Nevada and Sierra de Gádor (b53, b51, b52, b17, b57, b35 and b56).
- a north-south profile (NS2), with sites from Sierra de las Estancias and the Eastern part of Sierra de los Filabres (b37, b29, b58, b30 and b32).

Note that some of the sites were projected over two (perpendicular) profiles.

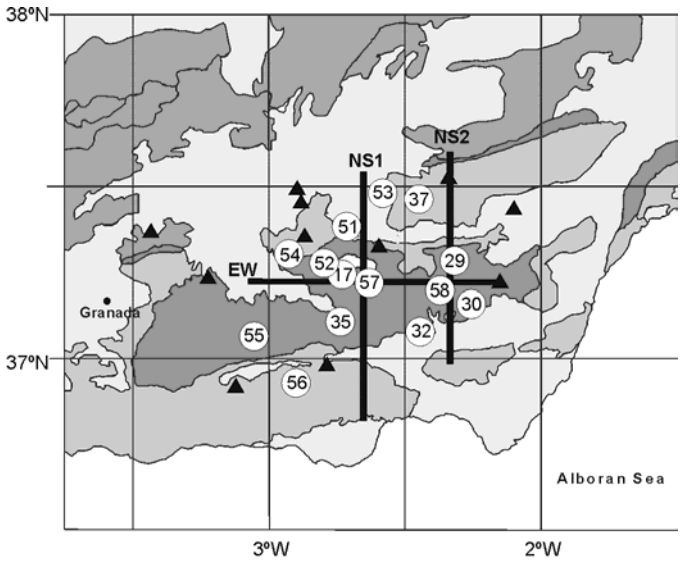

Figure 9.4: Location of Internal Betics MT sites and the 3 profiles, EW, NS1 and NS2 along which the three 2D models were constructed. Numbers in circles are the sites projected over one or two of the profiles.

9.2.3 Data set-up

In order to get the data ready to carry out the inversions, these four steps were conducted:

1) Rotations, identification of TE and TM modes

Since the data sites were projected over EW (i.e. 0^o Strike) and NS profiles (90^o Strike), the data did not need to be rotated. However in each case TE and TM mode had to be defined according to the alignments of the profiles and hypothetical strike directions (Figure 9.5). In the EW profile, since the strike direction is NS (i.e., along x), xy ≡ TE mode. In the NS profiles, yx is aligned along the strike and yx ≡ TE mode.

If tipper is used in the inversion (e.g., REBOCC and DetREBOCC inversions), only the component aligned with the profile is considered (in the 2D assumption, the other component is zero).

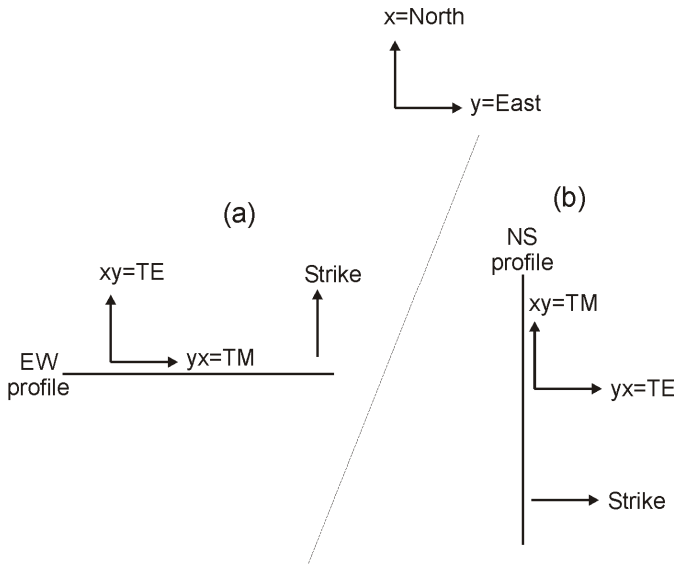

Figure 9.5 Schematic representation of TE and TM modes according to the profile alignment, a) EW and b) NS, using the same reference frame: x=North and y=East. xy ≡ E_x/B_y and yx ≡ E_y/B_x. TE: transversal electric mode: Electric field aligned with the Strike direction. TM: transversal magnetic: Magnetic Field aligned with the Strike direction.

2) Data decomposition

Given the complexity of the data and the presence of galvanic distortion, as obtained from the Groom and Bailey decomposition, data from each profile were decomposed

using the Strike code, to obtain period independent distortion parameters at each site. In this case the strike direction was fixed to 0^o.

The resulting distortion parameters were significant (i.e. twist and shear angles in general greater than 5^o), with large misfits: considering 5% error, values of $\chi^2/\chi^2_{95\%}$ between 1 (site b37) and 18 (site b30), with an average of $\chi^2/\chi^2_{95\%} = 5$, as expected from the invariants dimensionality analysis.

Final responses were computed by the Strike code as:

$$M_{2D^*}(\omega) = C^{-1} M_m(\omega)\,, \tag{9.6}$$

where 2D* refers to the fact that the MT tensor is not 2D, but that the non-diagonal components are assumed to be aligned with the principal directions. From this tensor, the xy and yx resistivities and phases to be inverted were obtained.

3) Static Shift corrections

Data decomposition does not resolve the static shift, which remains unknown. From the processed data (see Appendix D), evidences of static shift are seen as displacements between xy and yx resistivities, starting at the shortest periods, and are in general smaller than one decade.

Static shift was corrected by joining both resistivity curves. The reference resistivity was taken by observing the joining sites curves. This resulted that only yx curves were shifted.

In the inversions, several tests were made using or not using these statics shift corrections.

4) Inactivating periods

Finally, before running 2D inversions, spikes in the curve responses, as well as overly large tipper values were removed to obtain responses as smooth as possible. This was done site by site, by observing all responses' plots. On average, 15% of the data were rejected at each site (see table D.1).

5) Data errors

All data responses to be inverted were assigned an error floor (e_f), i.e., an error level to be taken as the error of a response in the case that its real error is larger than this error floor.

Resistivity and phase error floors were chosen so they have the same weight in the responses, whose relationship is $e_f(\varphi) = \frac{1}{2} e_f(\ln \rho)$.

With regard to the tipper, the recommended error floor, $e_f |\vec{T}| \geq e_f(\ln \rho) \cdot \max |\vec{T}| / 2$ (Gabàs *et al.*, 2003) was used.

9.2.4 Inversions and models

For each of the profiles, all the inversions performed departed from an homogeneous model of 100 Ω·m, using a period range from 10^{-3} s to 10^{3} s. The details of each inversion and the resulting models are summarised in Table 9.1.

Internal Zone Subset Profiles and projected sites	**Inversion code**					
	RLM2DI		**REBOCC**		**DetREBOCC**	
EW (90º strike) b55,b54,b52,b35, b17,b57,b58,b29, b30	TM mode Figure 9.7	rms=2.06	TM mode	rms=16.38		
NS1 (0º strike) b53,b51,b52,b17, b57,b35,b56	TM Fig. 9.6 Fig. 9.7	rms=2.14	TM mode Figure 9.8	rms=6.3	only det Figure 9.10	rms=3.23
	TM+TE Fig. 9.6	rms=6.53	TM+tipper Figure 9.9	rms=5.99	det+tipper Figure 9.11	rms=4.19
	TM+TE+ss Fig. 9.6	rms=5.26			det+tipper+ss Figure 9.12	rms=3.97
NS2 (0º strike) b37,b29,b58,b30,b32	TM mode Figure 9.7	rms=5.35	TM mode	rms=4.60	only det	rms=7.48
			TM mode + tipper	rms=2.88		

Table 9.1: Summary of the sites and profiles used to create 2D models from the Internal Zone subset, indicating the inversion code applied, the inverted data (ss: static shift correction), and the rms of the resulting models.

9.2.5 RLM2DI inversions results

For each of the three profiles over the Internal Betics (Figure 9.4), inversions of TM modes and TM+TE mode were carried out using resistivity and phases responses, before and after static shift corrections.

The same model mesh was considered at each profile to perform the different inversions. Experience with the forward estimation of the responses from synthetic models and inversion have demonstrated that it is necessary to run RLM2DI inversions with as regular a mesh as possible is necessary. Model meshes were extended laterally away from the profiles and to depths of up to 100 km to ensure the stability of the responses.

Models obtained from both TM and TE mode inversions presented large misfit values, as one would expect since TE mode is largely affected by 3D effects, whereas in the inversion models these effects as structures below the profile.

The fact of considering static shift corrections or not implies a significant change in the position, extent and conductivity value of the modelled structures. Below some of the sites, after inverting using static shift corrections, large conductivity contrasts with extreme values appear. This suggests a revision of the corrections already made.

In particular, three different inversions were performed for the NS1 profile: one using TM mode data and two using TE+TM data, before and after static shift corrections. Only one inversion was performed using TM mode data alone, because these were not corrected from static shift (only yx (TE) curves were shifted).

All the resulting models (Figure 9.6) have two resistive structures in the northern and southern parts of the models, and three conductive bodies, in the central and southern parts. However, it is evident that there are differences in their positions, shapes and conductivity values. The model using only TM data (upper panel) shows the simplest structure, with a small extent of the conductivity bodies and not particularly low conductivity values. The models from TE+TM mode inversions have a more complex structure (middle and lower panels), and a new shallow conductive body appears at the northern part of the model. Without static shift corrections (middle panel), all the structures appear at shallower depths and the conductive bodies increase in extent and conductivity. In the last model, after the static shift corrections (lower panel), all the conductive bodies increase in extension, depth and conductivity and have different shapes too.

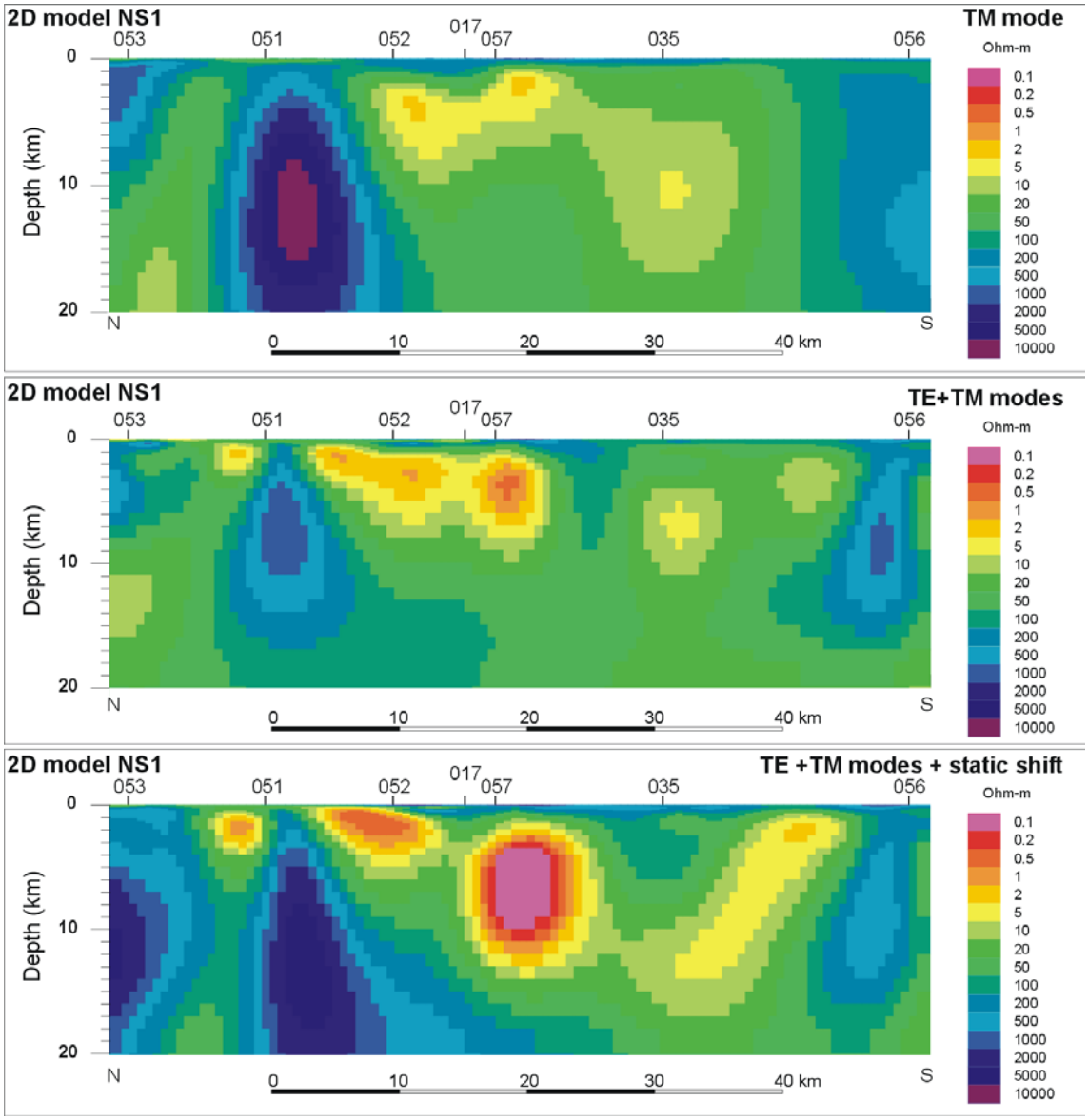

Figure 9.6: Comparison of NS1 profile inversion results, using TM data (upper panel) and TE+TM data, without (middle panel) and with (lower panel) static shift corrections. rms values: 2.14, 6.53 and 5.26 respectively.

For all the profiles, inversions using RLM2DI were performed considering TM modes, without static shift corrections (Figure 9.7). The resulting misfits are low (see figure captions).

Model EW (mesh of 135x50 elements) (Figure 9.7, middle panel) presents structures with well-defined contrasts and a lateral alternation of conductive and resistive bodies. Some interpretations may depict this as anisotropy. In this case it is a consequence of having inverted a profile along a hypothetical strike direction, as all the curves along the profile have similar decreasing resistivity curves. The central conductivity body, below sites 17 and 57, has a vertical extent from 2km-3km to 18km.

Model NS1 (127x50 elements) (Figure 9.7, upper panel) presents highly resistive bodies located under very thin conductive layers, at the northern side below sites located over the Guadix-Baza basin. Between sites 51 and 53, a moderately conductive zone appears at lower depths. The central part of the model, corresponding to the Nevado-Filábride unit (sites 52, 17, 57 and 35) is the most conductive, with a shallow resistive layer on top. The conductor reaches a maximum depth of 9km in its central part, and 15km (10 Ω·m) below site 35.

Model NS2 (74x60 elements) (Figure 9.7, lower panel), located 50 km East from NS1, shows a conductive structure similar to that of model NS1, which can be interpreted as the continuity of the first conductive zone along the Sierra de los Filabres.

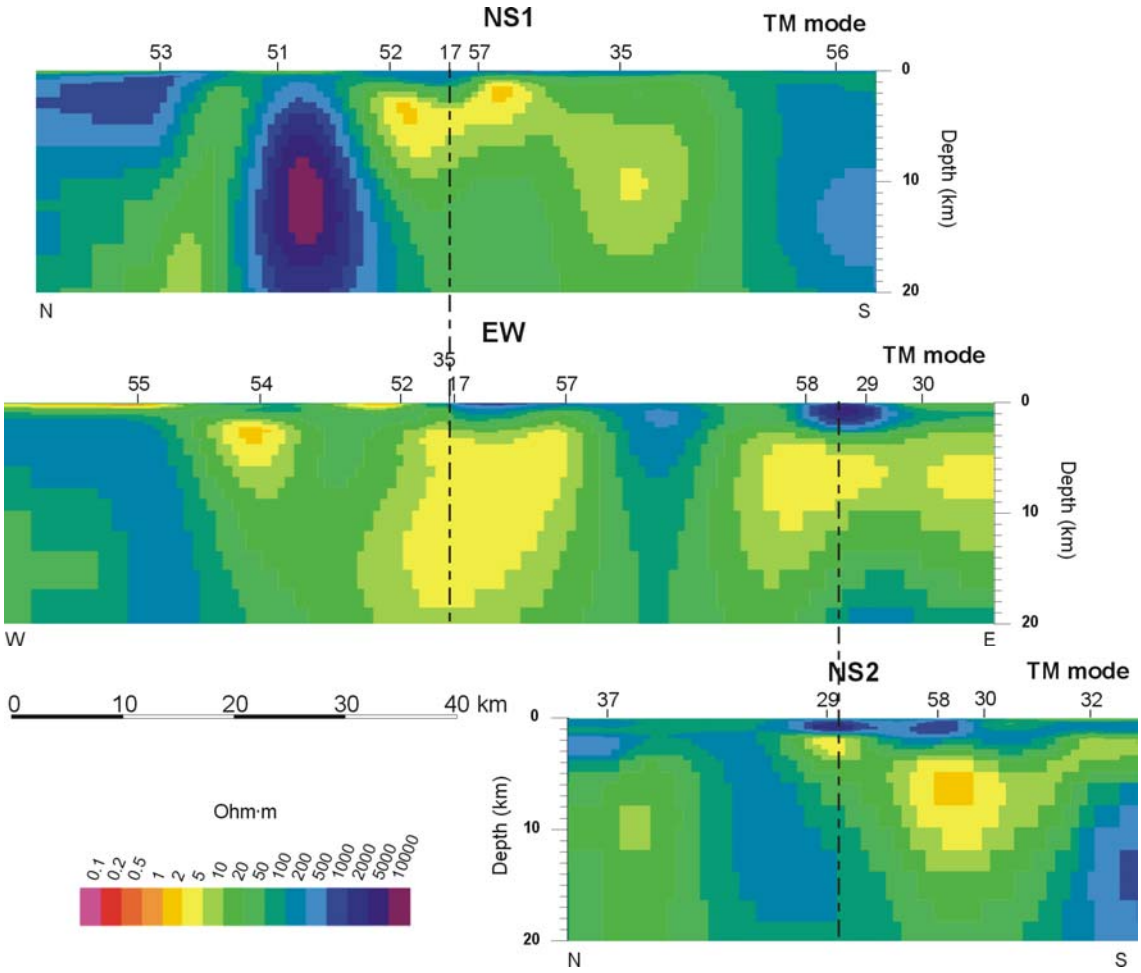

Figure 9.7: 2D models resulting from RLM2DI inversions of TM data, for the three profiles in the Internal Betics. Upper panel, model NS1 (rms=2.14, 57 iterations); middle panel, model EW (rms=2.06, 57 iterations); and lower panel, model NS2 (rms=5.35, 26 iterations). Dashed lines indicate the approximated tie points.

In the Northern side of this body (below sites 58 and 29), its base dips towards the south. Its limit with the underlying resistive structure can be interpreted as the base of the Nevado-Filábride complex.

Below the same sites, the structures depicted from EW and NS directed models are different, since different data polarizations were taken for each direction.

9.2.6 NS1 profile inversions using REBOCC and DetREBOCC codes

As an alternative to the inversions performed and as an opportunity to invert tipper data, REBOCC and DetREBOCC codes were applied to the three profiles.

Using these two codes, inversions from EW profiles showed very poor misfits, even when only considering TM data, since data from these profiles were far from 2D dimensionality with a NS directed strike. The models obtained from NS2 data showed better fits, but very simple structures. Hence, the following description focuses only on the NS1 profile.

A first inversion of the TM mode resistivity and phase data was performed using REBOCC code, to be directly compared to the RLM2DI code (Figure 9.8). Mesh size was set to 104 x 57 elements. The REBOCC model has smoother resistivity contrasts and a lower resolution in depth. REBOCC code has a much faster convergence rate (Siripunvaraporn and Egbert, 2000), although in this case the final *rms* values are higher than those using the RLM2DI code, one of the reasons being the lack of a conductive body below site b35.

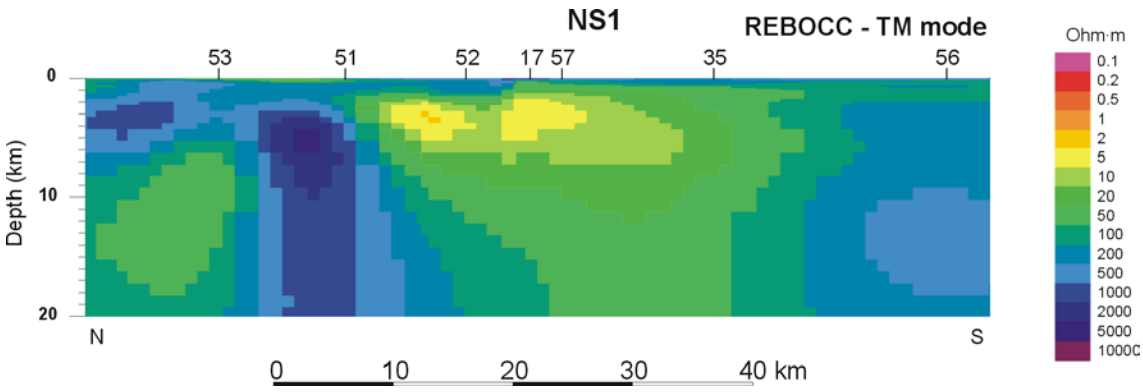

Figure 9.8: Model NS1 from REBOCC inversion of TM resistivity and phase data. (*rms*=6.3, 10 iterations).

The model obtained from joint inversion of TM mode and tipper data (Figure 9.9) presents similar features to the previous one. However, the conductor below Sierra de los Filabres has a larger extent below sites b57 and b17, and the conductor between sites b51 and

b53, already imaged using RLM2DI inversion, appears at a shallower depth, with a lower resistivity value.

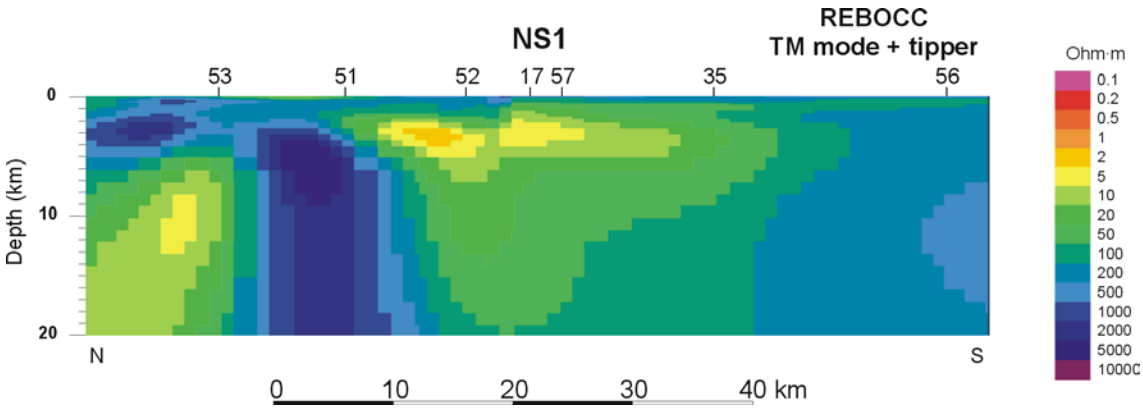

Figure 9.9: Model NS1 from REBOCC inversion of TM resistivity and phase and real and imaginary Tipper data. (*rms*=5.99, 10 iterations).

The DetREBOCC code was used to invert only the determinant data (computed as in eqs. 9.2 and 9.3, using all MT tensor components) (Figure 9.10), including the tipper data (Figure 9.11) and only the determinant data corrected from static shift (eq. 9.4), which resulted in an increase of the determinant resistivity values (Figure 9.12).

The first model (only determinant data, Figure 9.10) shows a conductivity distribution much different from the previous inversions. The conductive body located at the center of the profile, below Sierra de los Filabres, reaches larger depths (up to 20km). Its upper part presents a double-wedged shape, towards sites b52, with extremely low resistivity values, and b57. The inclusion of tipper data (Figure 9.10) allows better resolution of the modelled structures, without major changes, except for a conductive structure that appears at the northern part of the model.

The model obtained from the inversion of the determinant data corrected from static shift (Figure 9.12) presents similar features to the previous ones, especially that which included the tipper. The effects of the static shift correction are not as evident as those observed when inverting the TE mode, since in the present case, the corrections are averaged within the determinant.

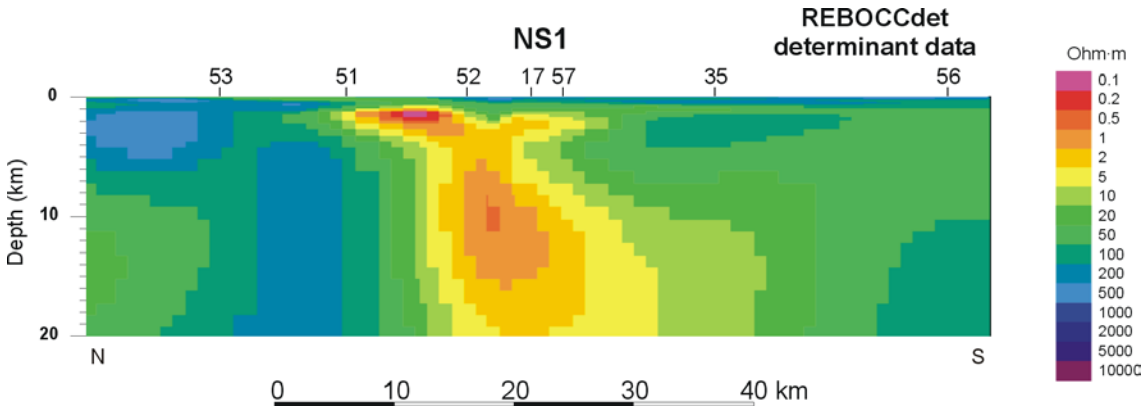

Figure 9.10: Model NS1 from DetREBOCC, inverting determinant data (*rms*=3.23, 10 iterations).

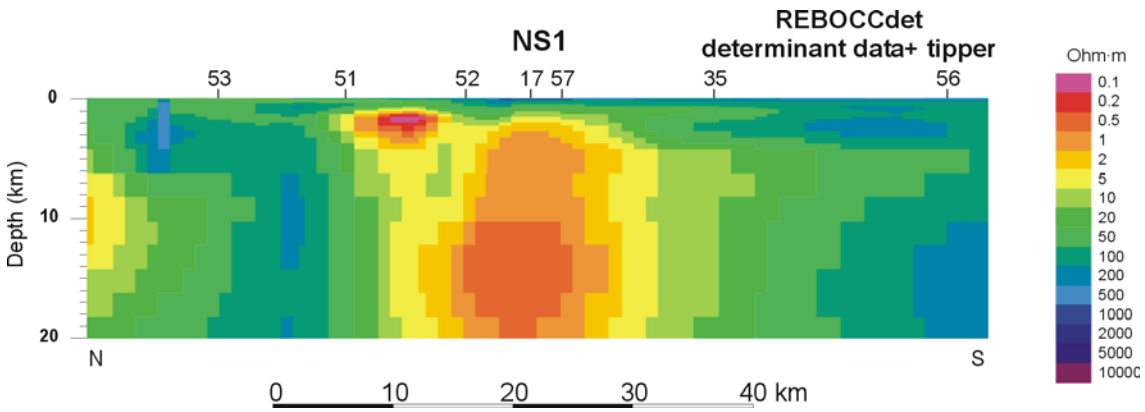

Figure 9.11: Model NS1 from DetREBOCC, inverting determinant data and tipper (*rms*=4.19, 10 iterations).

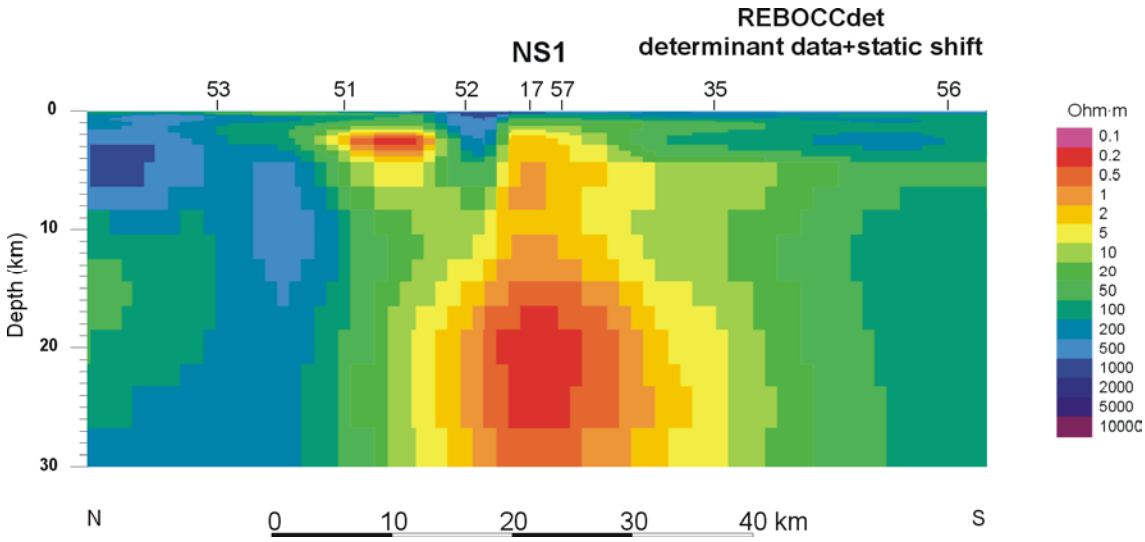

Figure 9.12: Model NS1 from DetREBOCC, inverting determinant, and after static shift corrections (*rms*=3.97, 10 iterations).

Although not shown here, all the models obtained from DetREBOCC inversions of profile NS2 present a differentiation between a shallow conductor located in the Northern part of Sierra de los Filabres and a central and much deeper one, with a variable depth, and a base located between 20 and 30km.

Further 3D modelling of the data should reveal the exact position and geometry of these conductive bodies, in which the sites are not projected over a certain profile.

The use of DetREBOCC code has produced models with very low misfits with respect to the data, and fast convergence rates. The inversion process considers the same amount of information as inverting only TM or TE modes, but, as the data are not truly 2D, the determinant contains information from the full impedance tensor.

9.3 Conclusions

The previous NW-SE 2D resistivity model of the central Betics, which showed a deep conductive body, was revised and a sensitivity test was performed to obtain the resolution at different parts. From this test it can be said that the model is well resolved at shallow depths, whereas resolution is lost in depth. The model responses are sensitive to the deep conductor, although, from the dimensionality results, its lateral continuity is not ensured.

Three 2D models over the Internal Zone, EW, NS1 and NS2, along and across the Nevado-Filábride unit were built as a preview of the 3D model, using RLM2DI inversion code.

The weak point of these inversions is that the data are not truly 2D, and the sites have been displaced and projected over very hypothetical strike directions. Hence, some local conductivity structures are extrapolated to the whole model.

The effects of both the inverted modes and the static corrections are observed in the shapes and resistivity values of the modelled structures, whereas, with some exceptions, these structures are common for all the inversions.

The model EW showed an alternation of conductive and resistive bands, a consequence of inverting data along an approximated strike direction. The largest of these conductors reaches a depth of 18km. NS1 and NS2 models show a conductive body, located below the Nevado-Filabride complex outcrops, which reaches a maximum depth between 10km and 15 km, much shallower than the body imaged in the previous NE-SW model.

The NS1 model was compared with the results from inversions using codes REBOCC and DetREBOCC, which allowed inverting the tipper. With only small variations, all the resulting models presented a conductive body with its base located at 20km depth.

Among the different codes, for the data inverted in this chapter the inversion of the determinant seems to be the most reasonable, because it inverts a response that contains information of the full tensor and is less influenced by the strike direction.

The use of the determinant data in further 3D modelling seems to be a good tool as well, which has the advantages that the sites would not be projected over any particular profile and structures could be imaged in their real positions.

Chapter 10: 3D Modelling of the Central Betics Geoelectric Structure

In this chapter, the modelling of the geoelectric structure of the central Betics crust is presented. Provided that the dimensionality of the data is mainly 3D, with superposition of 2D and 1D cases at particular period ranges, 3D modelling is the only one that has the potential to reproduce the geoelectric structure that best fits all data responses.

The proposed 3D model was constructed from an initial model, and later modified through a trial and error process. In this process, model responses were computed using Mackie *et al.* (1993) forward modelling code. The details of this 3D modelling process, the final model, its misfits, the sensitivity tests and the interpretation of the model features, are addressed below.

10.1 Data Set-Up

Data set-up consisted of arranging the measured data to make them comparable with the model responses, including the following steps:

- Set all the data with the same axes orientations: in this case, x=NS and y=EW, which, as will be seen, coincides with the model orientation.
- Static shift corrections: shifts between xy and yx resistivity curves, and between the resistivity curves at nearby sites, were corrected, in the same way as explained in the 2D modelling data set-up (chapter 9, section 9.2.3). This procedure is justified by the fact that, after several tests, the 3D model responses did not show any

significant separation between the resistivity responses, and hence would not be comparable to the data if it were not corrected from static shift.

- Rejecting data: all site responses were reviewed to inactivate periods with data spikes and ranges of periods with uncommon curve shapes (steep slopes and discontinuities). This lead to the rejection of site b09 (see curves in Appendix D) for having resistivity curves with slopes greater than 45^{o} and phases out of the expected quadrants. As a consequence the final dataset used in the modelling consisted of 42 sites.

The final dataset, compared to the dataset inverted to create the 2D MT1 model of the central Betics (Pous *et al.*, 1999), shows different resistivity curves shapes, and lower resistivity values at some of the common sites of both datasets. This is due to: 1) in this data set-up, where no information is available, the curves were not significantly displaced from their original values; and 2) the data utilised in the MT1 inversions had been rotated and corrected from galvanic distortion assuming a 3D/2D behaviour.

10.2 Model Mesh and Initial Model

A preliminary model mesh with an initial conductivity distribution was constructed from Occam's 1D inversions (Constable *et al.*, 1987) of determinant resistivity and phase at each site. Through an interpolation of horizontal and vertical resistivity values, it resulted in a NS-EW oriented model. The horizontal model mesh was regular, in which sites were relocated at the centre of the cells. The vertical mesh had cell thicknesses increasing logarithmically, with depths from hundreds of metres to tens of kilometres.

The mesh of this preliminary model was extended horizontally (50 km towards south and east) to ensure stability of the responses and to include part of the adjoining Alboran Sea, to model the sea effects. Cells were also split or combined at zones where sites were too close or too distant, respectively. Vertically, the first layers of the mesh were split to gain resolution at the shortest periods. After these modifications, the model mesh considered in our modelling consisted of a rectangular prism with a size of 270(NS)x220(EW)x100(z) km, made up of 50x50x25 cells (Figure 10.1). It extends over the Central part of the Internal and External zones, and includes the eastern end of the Guadalquivir Basin, part of the southern Iberian Massif and a strip of 35 km of the Alboran Sea.

The resistivity distribution of the preliminary model, with a high conductivity zone in its southeastern part, extending in depth from ten to seventy kilometres, was modified in order to be consistent with the static shift corrections applied to the data. On the other hand, specific

conductivity values obtained at the first layers below certain sites were extended towards zones not covered by data, following the distribution of the surface geological units. Hence, low resistivity values (5 Ω·m) were introduced beneath the Cenozoic basins, high values beneath the Internal Zone metamorphic units (200 Ω·m and 500 Ω·m) and Iberian Massif (500 Ω·m), and low to intermediate values beneath the External Zone (50 Ω·m and 100 Ω·m).

In the Alboran Sea, water depth was included in the model, with a resistivity value of 0.5Ω·m and the resistivity of the underlying materials fixed to 50 Ω·m. Below, a relative conductive zone (20 Ω·m) was modelled from 50 km downward, to reproduce the inferred presence of asthenospheric material (e.g. Polyak *et al.*, 1996; Torné *et al.*, 2000; Frizon de Lamotte *et al*., 2004). This simple lithospheric resistivity model was imposed since there is neither MT data coverage over the Alboran Sea nor a good knowledge of the crustal structure of this area.

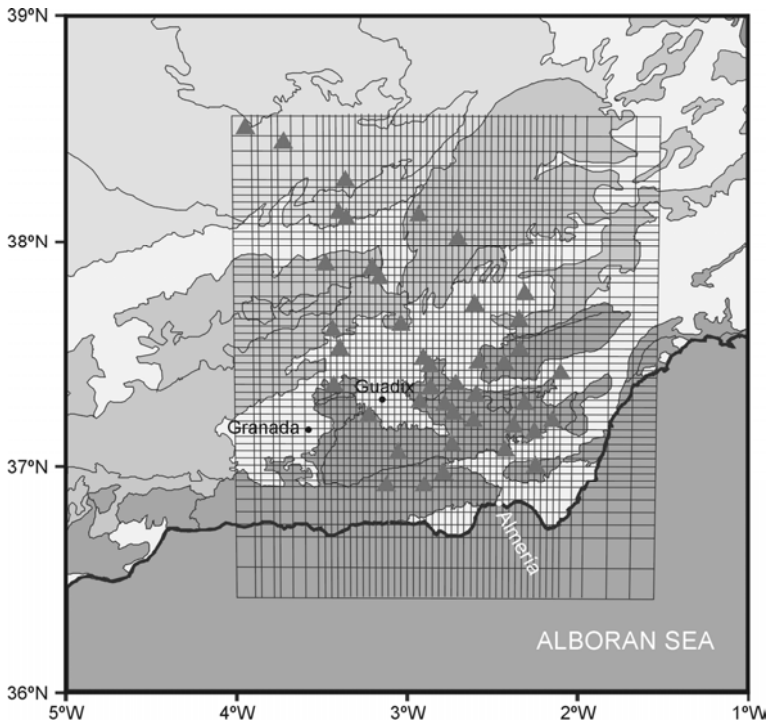

Figure 10.1: Horizontal 2D mesh utilised to construct the initial 3D model, superimposed over the geological units and MT site locations.

The model, result of applying all the previously explained mesh and resistivity distribution modifications is shown in Figure 10.2 and constituted the initial model upon which further models were built.

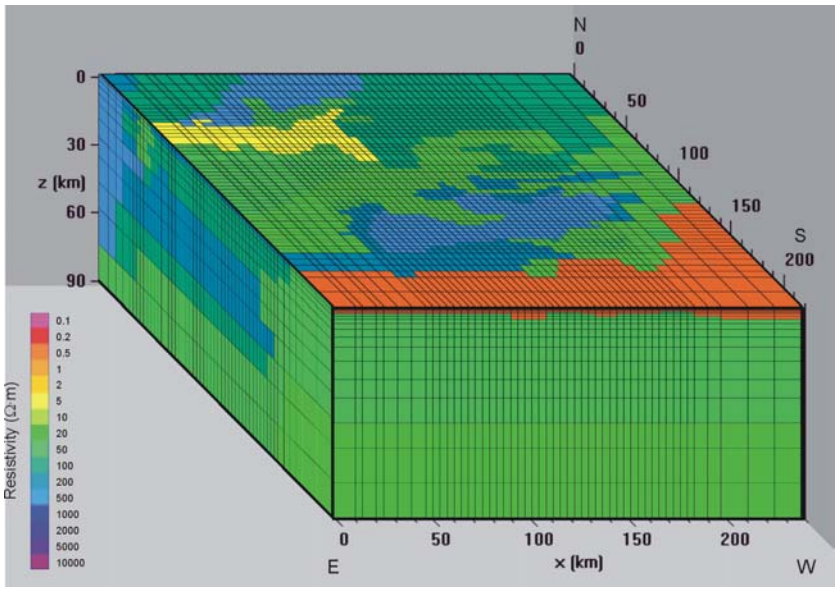

Figure 10.2: 3D view of the initial model and mesh, modified to include the Alboran Sea (0.5 Ω·m) and to reproduce the main geological features.

10.3 Trial and Error Process

Departing from the initial model, successive 3D models were obtained through a trial and error process, which included forward modelling comparisons of responses and model transformations.

The 3D forward modelling was computed using the Mackie *et al.* (1993) code, which was run for 24 periods from 10^{-3} s to 10^{3} s. For the mesh considered (50x50x25 elements), each run took approximately 30 minutes using an Intel Pentium4 (3.0 GHz) processor.

From the electric and magnetic fields obtained from each run, the model responses and related parameters (xy and yx resistivities and phases, determinant responses, WAL invariants and dimensionalities) were computed at MT site positions. Their values were compared with the data responses. The misfits between both responses were analysed using pseudo-sections of the responses plotted at constant periods and were quantified using the rms (eq. 9.5). This allowed identifying the zones of the model with poorer fits and modifying the model accordingly.

Once a satisfactory model was obtained, some very local features non-identifiable with geological structures or bodies were removed, in what was called the smoothing of the model. This smoothing was only considered valid if successive forward modelling steps showed no significant changes in the model responses.

10.4 Final Model

After 140 trial and error steps, a satisfactory model (bet3D-140) was obtained, regarding both data fits (explained in section 10.5) and model smoothness. The most relevant features of this model are shown in the horizontal slices at Figure 10.3 (pages 214 and 215) up to 40 km. Below this depth, the recorded data do not allow constraining any geoelectrical structure and hence, the corresponding slices are not shown.

Apart from the Alboran Sea, the model denotes that, up to 40 km depth, the Central Betics and adjoining areas are relatively resistive (mainly 50 Ω·m to 100 Ω·m) with high conductive bodies located at the uppermost crustal levels (<5 km) in the External betics and both uppermost to middle crustal levels (<17.5 km) in the Internal Betics. It also shows that the conductivity distribution is more complex at upper crustal levels beneath the Betic Chain. This fact is explained by the higher density of sites over this zone and the loss of the model resolution in depth.

Next, the detailed geoelectric features of the final model are described from northwest to southeast, perpendicular to the main trend of the Betics structures. In this description the model has been divided following the surface distribution of the main Alpine geologic units recognized in the area. This division facilitates the description of the model, but has the inconvenience that the boundaries between these geological units are not vertical but tilted or even near horizontal (unconformities, thrusts, etc.), and therefore, that bodies as structures of different units could be and indeed are present beneath the outcropping ones. Consequently, deep geoelectrical features observed below an outcropping unit could be not related to this unit but instead to another geological unit that is present at depth.

The main resistive and conductive zones of the model were identified as **R** (resistive) and **C** (conductive), plus the site number or acronym of the geological region beneath which these are located, and an additional number in case there is more than one resistor or conductor in the same area (e.g.: **CF1**, **CF2** and **CF3** are the three conductive bodies located below the Sierra de los Filabres).

- **Iberian Massif** (northwestern side of the model, sites b14, b13, b11, b07 and b08):

  At all modelled depths, the resistivity is moderate to high, with a general decrease of the resistivity values from NW (200Ω·m to 2000Ω·m, identified as **RIM**) to SE (20 Ω·m to 50 Ω·m).

  Within this resistor **RIM**, however, some relative conductors have been identified. One of them (**CIM**, 50 Ω·m) is a band located at depths between 2.15 km and 17.5 km (Figure 10.3i to Figure 10.3o) that cuts NE-SW across the resistive zone **RIM**. The

other two conductors are narrower and restricted to the SE areas where a Mesozoic cover overlies the Variscan basement: the **C7-8** conductor (10 Ω·m) located between 900 m and 1.2 km, and the conductor named **C-11** (Figure 10.3h), recognised between 1.6 km and 2.8 km.

- **Guadalquivir Basin:**

Beneath the outcropping sediments of this basin, the model reproduces a superficial conductor (**CGB**) up to 350 m depth that depicts a general E-W orientation. This conductor appears again, more localised, between 650 m and 900 m (Figure 10.3e). Below, the resistivity increases with depth, reaching similar values to those described in the Iberian Massif (100 Ω·m – 500 Ω·m).

- **External Zone-Prebetics** (sites b26 and b24):

This part of the model is characterised up to 2.15 km by moderate resistivity values (20 Ω·m – 50 Ω·m); bounded beneath by resistivity values ranging from 100 Ω·m to 500 Ω·m, which are also similar to those described in the Iberian Massif. At site b26, and at a depth between 350 m and 650 m, the model also shows the presence of a conductive body which is a continuation of the conductor **CGB**, recognised in the Guadalquivir Basin.

- **External Zone-Subbetics and Guadiz-Baza basin** (sites b40, b06, b05, b41, b03, b27, b23, b21, b38 and b20):

The resistivity pattern of the model beneath the outcropping Subbetics is similar to that described in the Prebetics. There is an upper body (up to 1.2 km) of moderate resistivities (10 Ω·m – 50 Ω·m) and a deeper resistor with values similar to those of the Iberian Massif (100 Ω·m – 200 Ω·m). Locally between these two bodies, in the northern part of this zone, there is a 2 Ω·m – 5 Ω·m conductor which is a continuation of the **CGB** conductor of the Guadalquivir Basin. However, the model shows that there are remarkable differences between the geoelectric features of the upper body in both External Zone domains: Whereas in the Prebetics the resistivity is rather homogeneous, in the Subbetics the model records two well differentiated zones: a moderate resistivity zone that coincides at surface with outcropping rocks of the outer Subbetic domain; and a conductive zone restricted to the southeast and formed by two isolated conductors (**C20** and **C27-38**). **C20** crops out at surface east of the Guadix-Baza Basin in the areas where pelagic rocks of the inner Subbetics appear at surface, and it is also present

beneath site b23 from a depth of 350m. This is a conductor with resistivity values between 1 Ω·m and 5 Ω·m that reaches depths from 900 m below site b23 to 7 km below site b20. Therefore, it is a conductor bounded downwards by a south dipping surface. Towards the south, it is bounded by a near vertical E-W oriented surface. The other conductor, **C27-38**, is also located beneath the Guadix-Baza Basin, near the southern boundary of the Subbetics but it does not crop out at surface. The top of this conductor appears at a depth of 900m, and its bottom reaches a maximum depth of 2.8 km.

In relation to the conductor **CGB** located between the upper body and the deeper one, the model shows that the conductor in the Guadalquivir Basin continues southwards beneath the resistive rocks of the external parts of the Subbetics. With values ranging from 2 Ω·m to 5 Ω·m, this conductor appears beneath sites b40, b05 and b06, where its bottom is located at greater depths than in the Guadalquivir Basin: 1.2 km beneath site b40 and 5 km beneath sites b05 and b06.

Finally, it should be noted that the Guadix-Baza basin infill is not well reproduced by the final resistivity model.

- **Internal Zone** (sites b53, b37, b19, b02, b01, b51, b36, b60, b32, b30, b59, b54, b18, b52, b17, b57, b35, b58, b29, b15, b56, b33 and b31):

As already stated, this zone of the model is characterised by its high complexity, with well-differentiated resistors (**RI**) and conductors (**CE**, **CF1**, **CF2**, **C31**, Figure 10.4 and **CF3**, Figure 10.5). Up to 13.5 km depth, in the north and above the top of conductor **CF3** in the central and southern parts of this zone, the crust is characterised by moderate to high resistivity values (**RI**, Figure 10.3a-n), comprised between 200 Ω·m and 1000 Ω·m, with areas of moderate resistivity values (20 Ω·m – 100 Ω·m). Among these, high conductivity zones appear at different position and vertical extents.

In relation to the conductors, the conductor **CE** (2 Ω·m – 5 Ω·m) (Figure 10.3g-i) has a vertical extent from 1.2 km to 2.8 km, west of the Sierra de las Estancias. Conductors **CF1** and **CF2,** located beneath the Sierra de los Filabres (Figure 10.3h-j), have the same resistivity values as the conductor **CE** and have a vertical extent from 1.6 km to 3.8 km. In the southeastern part of the model, below Sierra de Alhamilla, conductor **C31** (5 Ω·m) appears, with a vertical extent between 500 m and 2.15 km (Figure 10.3d-h). Below **CF1** and **CF2**, conductor **CF3** (1 Ω·m – 5 Ω·m) is the largest conductor and the most striking feature of the model (Figure 10.3k-o). It has a WNW-ESE orientation and its top is located at 3.8 km depth. The bottom of this conductor ranges between 5 - 7 km

in the southeastern part, 9 km in the northwestern part, and 17.5 km in the central part (Figure 10.5).

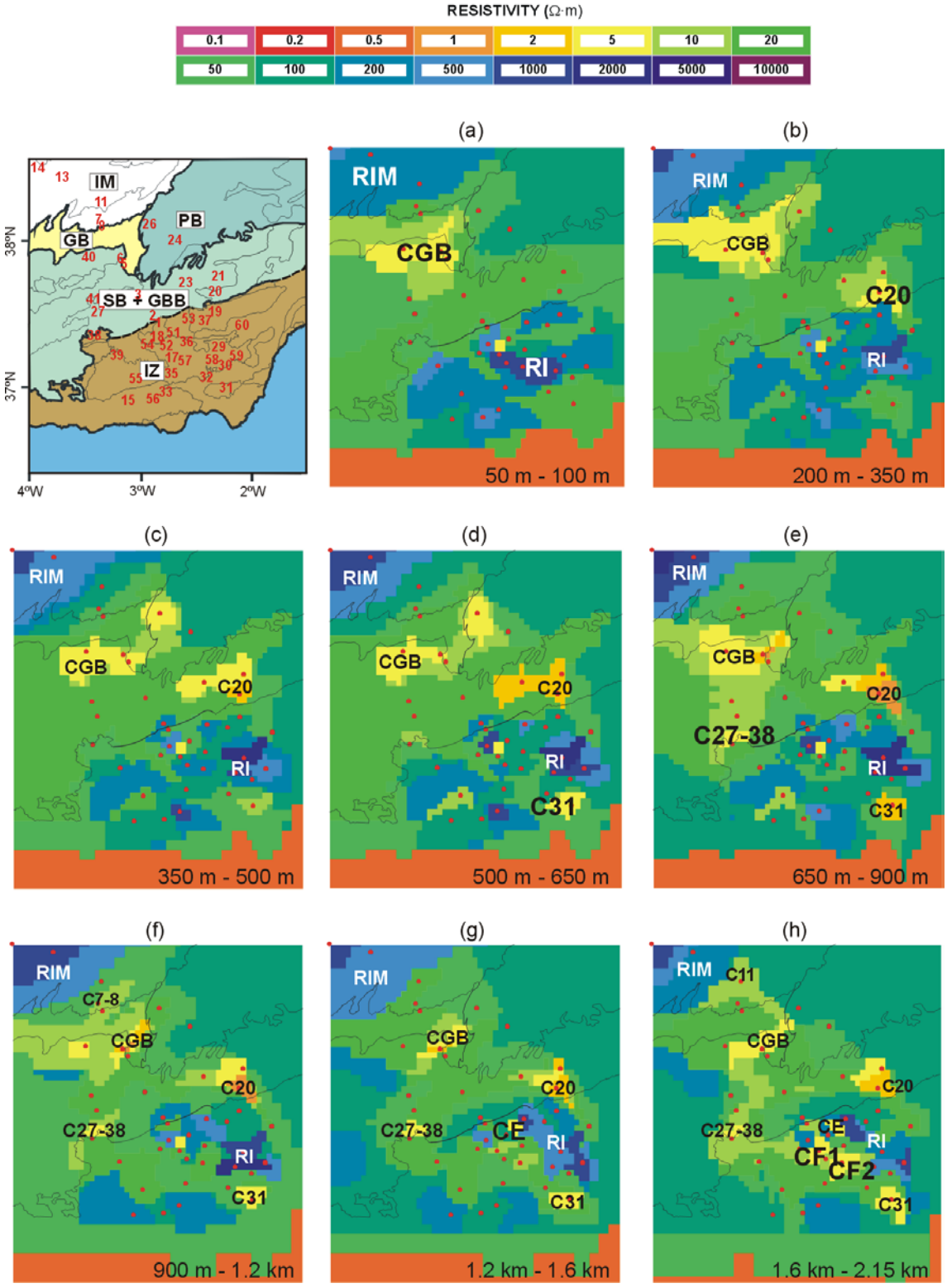

Figure 10.3: Situation map and horizontal cross-sections of the most relevant layers of the final 3D model. Situation map: Site locations in red; main geologic zones used in the model description, separated by wide black lines : IM (Iberian Massif), GB (Guadalquivir Basin), PB (Prebetics), SB+GBB (Subbetics + Guadix-Baza Basin) and IZ (Internal Zone). Cross-sections: red dots indicate site locations; narrow lines mark the geological divisions; the depth range of each layer is indicated in the lower-right;

abbreviations correspond to the main conductors and resistors described in the text, which are indicated in a larger font at its upper position. C: Conductors R: Resistive.

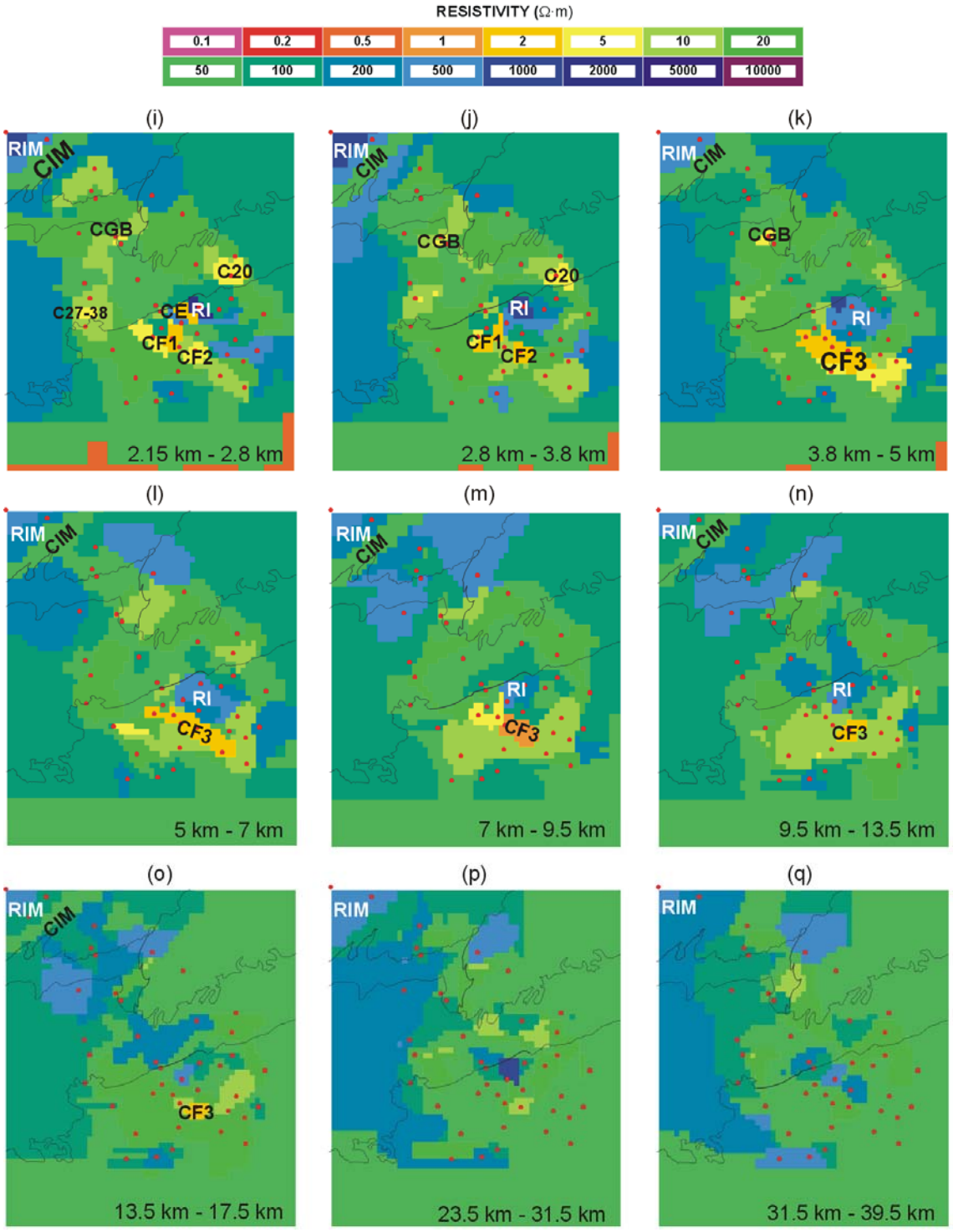

Figure 10.3 (cont.)

Beneath the resistive zone **RI** and the deep conductor, **CF3**, i.e., at depths greater than 13.5 km to 17.5 km, the model shows moderate resistivity values, similar to those

observed in the deeper Iberian Massif and External Zone domains. Nevertheless, locally, beneath site b51 a highly resistive zone (2000 Ω·m) appears between 17.5 and 31.5 km.

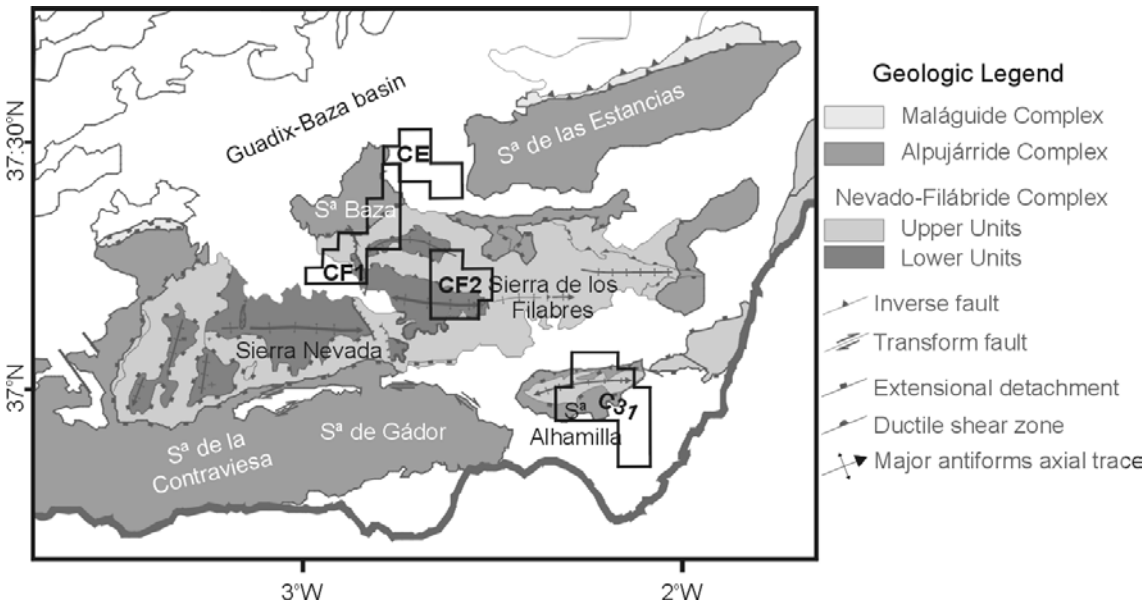

Figure 10.4: Geologic map of the central sector of the Betics Internal Zone, with the locations and shapes of the main shallow conductors imaged in this area. The shapes of these conductors are those of its maximum horizontal extension.

10.4.1 Comparison with 2D conductivity models

Vertical sections of the 3D model bet3D-140, coincident with the 2D conductivity models NS1, NS2 and EW, exposed in chapter 9 (see profiles locations in Figure 9.4) are displayed in Figure 10.6. Comparing the vertical sections of the 3D model with the 2D models, significant differences appear:

The three sections (Figure 10.6) differ significantly from the corresponding 2D models (chapter 9, Figure 9.7). The conductor beneath sites b58, b29 and b30 shown in the 2D model EW disappears; and the deep conductor present beneath the Nevado-Filábride complex has a higher conductivity in sections EW and NS1 but is lower in section NS2. Also, it reaches lower depths in profile NS1, whereas in the profile NS2 it is clearly shallower.

Since the same data sites and static shift corrections have been used in the 3D and 2D approaches, the differences between the three models and sections can be attributed only to the modelling approach, e.g. to the fact of projecting the data sites or not to a profile. In this case, sites have been projected up to 30 km, which is significant given the complexity of the area.

Hence, in the 3D model, the conductive and resistive bodies are more local, such as the deep conductor that is not shown in the 3D section of NS2. In general, the 3D model images some conductive and resistive structures similar to the 2D, although with different positions, sizes and resistivity values.

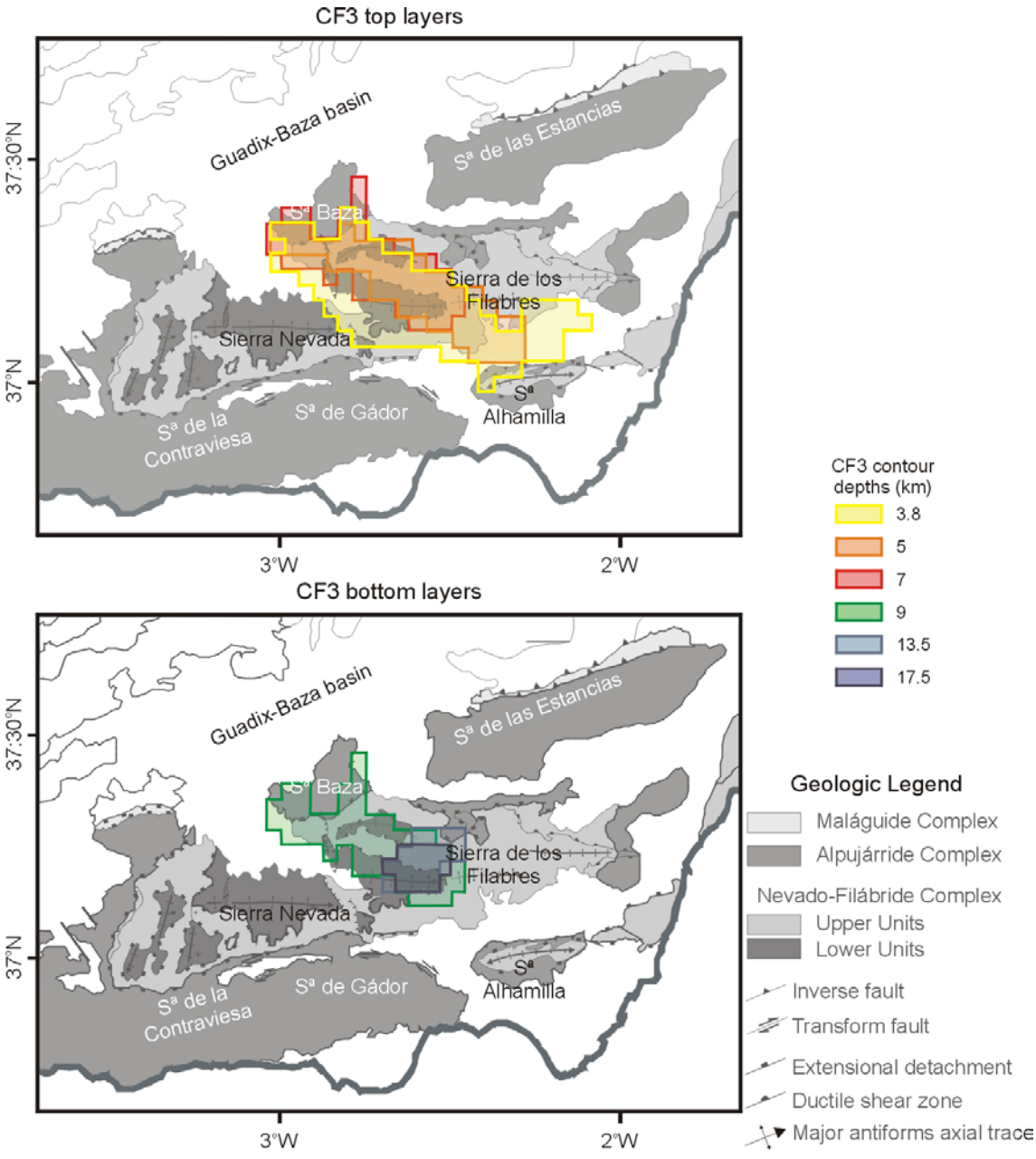

Figure 10.5: Geologic map of the central sector of the Betics Internal Zone, and contours of the top (upper panel) and bottom (lower panel) of conductor CF3.

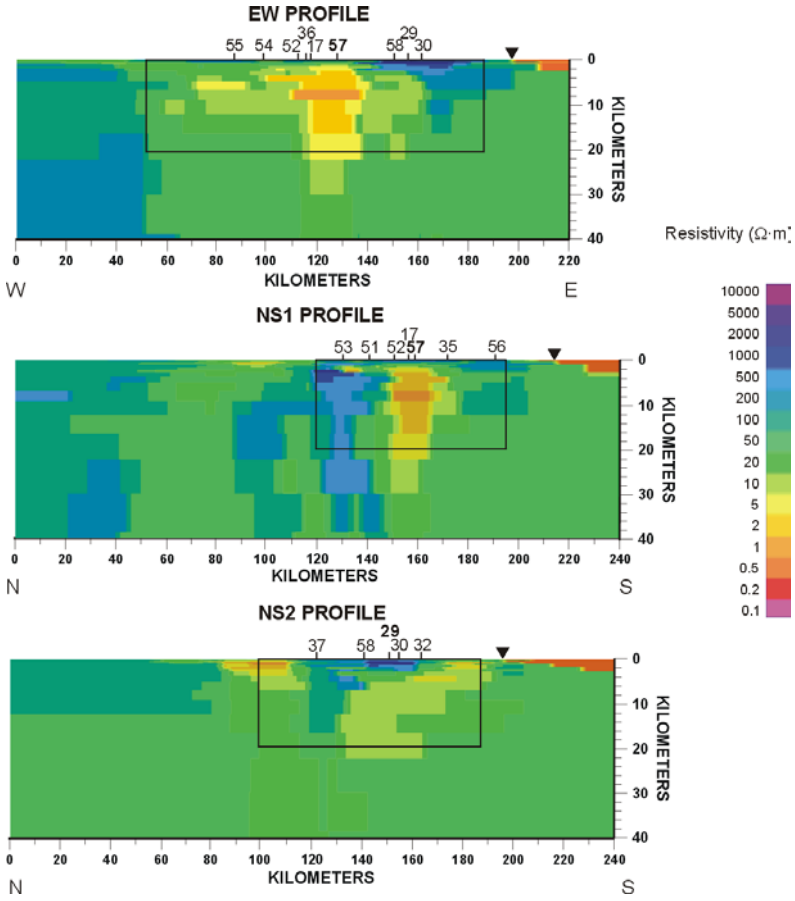

Figure 10.6: Vertical sections of the 3D model bet3D-140 along the NS1, NS2 and EW profiles (see Figure 9.4 for locations). Numbers on top indicate site locations projected over the vertical section. Sites located on the profile trace are in bold. Inverted triangle: coast line. Framed areas indicate the extent of the 2D models.

10.5 Comparison of Responses and Misfits

Data and model bet3D-140 determinant resistivity and phase responses (Appendix E) present a good fit at all sites, except at site b26. At this site, it was not possible to fit data and model responses at periods longer than 1s. Hence, this site was not considered in the computation and analysis of misfit values and further sensitivity tests.

At the other sites, considering an error floor of 10% in the resistivities and 2.9° in the phases, the total rms values are rms(ρ_{DET})= 4.08 and rms(φ_{DET})=2.32. Short period data (up to 1s) are well fitted by model responses, presenting low rms values (rms(ρ_{DET})= 2.94 and rms(φ_{DET})=1.85), whereas for periods longer than 1s, the model does not reproduce so well the data responses (rms(ρ_{DET})= 5.11 and rms(φ_{DET})=2.65) (see Figure 10.10).

Maps of the total rms values at each site averaged over all periods are plotted in Figure 10.7. They show a broad variation of the determinant resistivity misfits (rms(ρ_{DET})) along the different sites locations compared to the misfits of the determinant phases (rms(φ_{DET})), which are more uniform. Higher values of rms(ρ_{DET}) (>5) are present over the Internal Betics and over sites b14 and b40. The high rms values over the Internal Betics are caused by the high density of sites, with different responses, and the difficulty to fit all them jointly. However, at sites b54 and b57, the high rms values are due to the difficulty of fixing the pronounced negative slope at the middle and long periods (>10 s). Similarly, the high rms values observed at sites b14 and b40 are also caused by the longest periods.

In relation to the determinant phases, the misfits are generally low with values comprised between 1 and 3. The only exception is site b08, which shows a significantly higher value (rms(φ_{DET})=6), a consequence of the proximity to site b07, with significantly different resistivity responses.

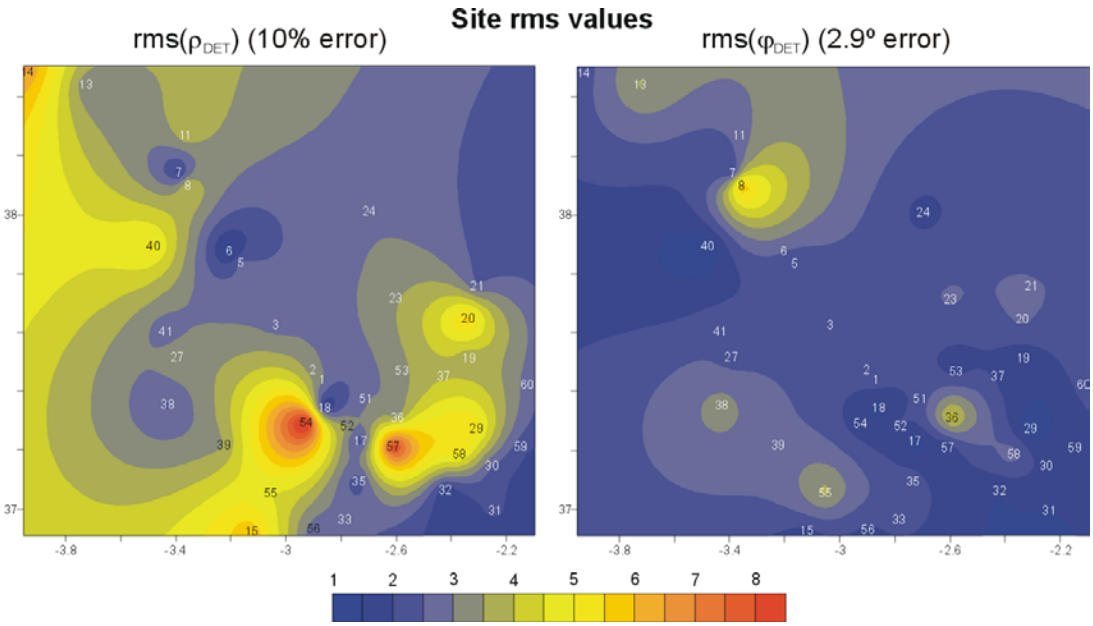

Figure 10.7: Rms maps of the determinant resistivities and phases of the Betics MT sites in reference to bet3D-140 model responses. Numbers on the map indicate site locations.

The rms values of the WAL invariants between data and model responses were also computed, a 10% error. I_1 and I_2, related to the magnitude of resistivity and phase, present low rms values (rms(I_1)=2.87 and rms(I_2)=2.51). For the rest of invariants, although both in the data and model responses are increasing along with the period, the rms values are significantly higher (rms(I_3)=10.84, rms(I_4)=21.56, rms(I_5)=31.09, rms(I_6)=144.53, rms(I_7)=124.76 and

rms(Q)=13.40). Nevertheless, it must be noted that, as already shown in chapter 8, the errors of the Betics dataset invariants are in general higher than 10%. The reasons for these elevated values of the rms stand on the difficulty on jointly fitting all these six invariants and on the lack of errors and/or geologic noise effects in the invariants computed from the ideal model.

10.5.1 Dimensionality of the 3D model

WAL dimensionality analysis of the model bet3D-140 was carried out at the data sites locations (Figure 10.8). Given that it was performed on model responses, not affected by either statistical or geologic noise (i.e., ideal data), a small value of the threshold was used (τ_W=0.01). Although the results do not coincide with the dimensionality obtained from the data at most of the sites, these show how the model complexity increases with the period, and towards the south, as obtained from the data analysis.

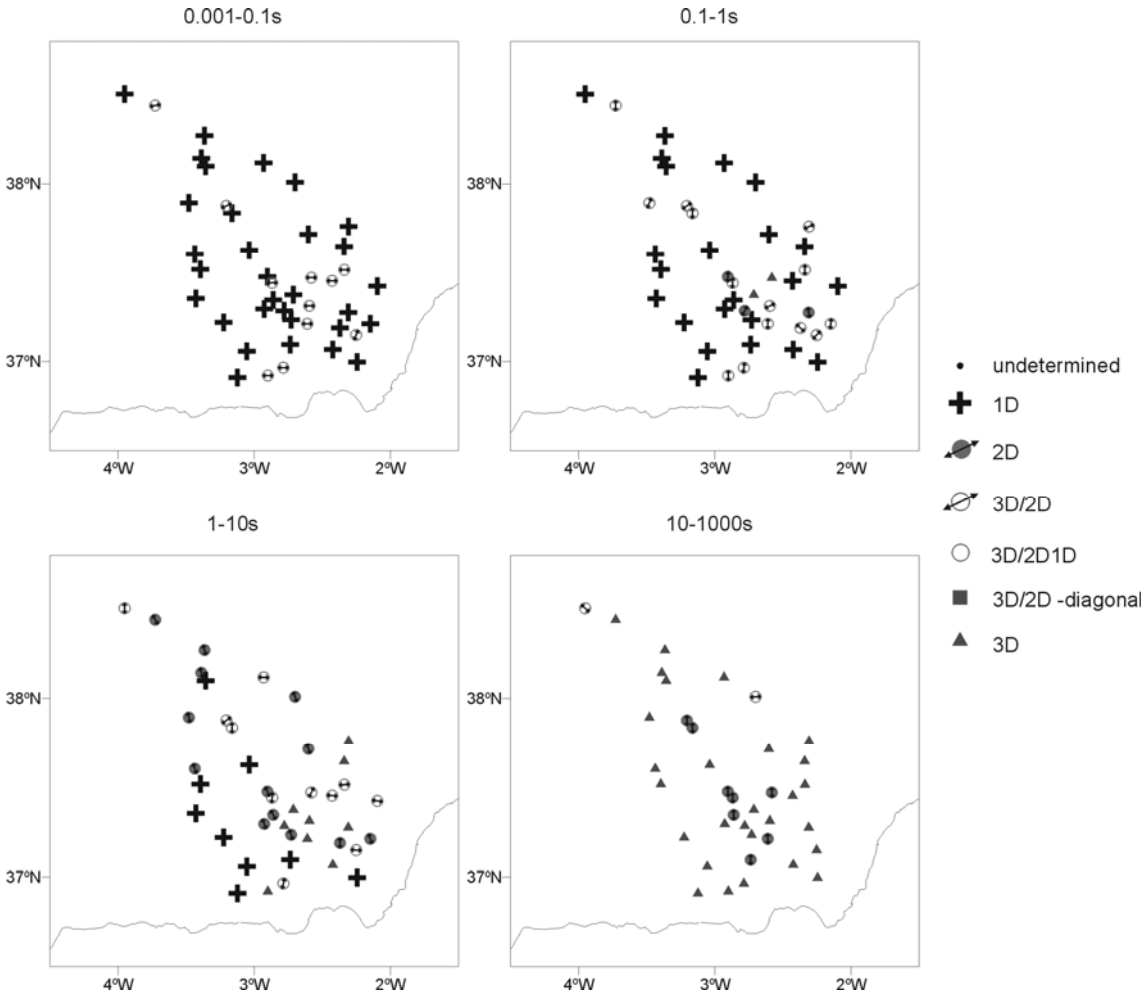

Figure 10.8: Model dimensionality using WAL criteria, using τ=0.01 and τ_Q=0.1.

10.6 Sensitivity Tests

The low and moderate values of the rms obtained between the data and model apparent resistivities and phases allow one to consider the model bet30-140 as valid. However, in order to determine how well defined is the structure shown by the model, sensitivity tests were performed. These deal with: 1) model mesh and 2) position and size of the conductor **CF3** (Figure 10.3k, page 205) located below the Sierra de los Filabres.

Among the sensitivity tests, none were carried out on the resistivity values. It was not considered necessary since along the different steps in the construction of the model, resistivity values were well contrasted. Resistivity values of the model are very sensitive to the static shift correction carried out in the data, and had these corrections been different, other resisitivity values in the model would have been obtained. However, this was outside the scope and time constraints needed to perform such different corrections and to verify them.

10.6.1 Model mesh

With the aim of checking the adequacy of the mesh used to construct the 3D model (50x50x25 elements), the model mesh was resized to 80x80x40 elements. Using this new mesh, the computed forward responses resulted in an increase of the resistivity rms values (Table 10.1). This increase is mainly caused by site 14 ($rms(\rho_{DET})_{bet30\text{-}140}$=6.08 and $rms(\varphi_{DET})_{resized}$=22.29), located at the NW edge of the model, and is attributed to the new boundary conditions, which were not inspected in detail. At the rest of sites, no significant changes in the responses were observed. Consequently, it can be stated overall that the model responses converge and are stable with the mesh size.

Rms/model	Model bet3D-140	Resized mesh model
rms(ρ_{DET}) 10% error	4.08	4.38
rms(φ_{DET}) 2.9° error	2.32	2.38

Table 10.1: rms values of the determinant resistivity and phase between data responses and the original model (bet3D-140) and resized model responses.

10.6.2 Position, extension and size of the conductive body CF3

The presence of a large conductive body at mid crustal levels below the Internal Zone is one of the most striking results obtained from the MT study performed in the Betics.

Consequently, several tests were performed to infer the extension and position of the conductor **CF3** and also to check whether the overlying conductors **CF1** and **CF2** can be considered part of **CF3** or not.

CF3 body extension tests:

To test the horizontal extension of the conductor **CF3**, two new models were constructed (Figure 10.9). In the first one, conductor **CF3** is located only below sites b17 and b57 (bet3D-1757), and in the second, the conductor is extended towards the southwest (bet3D-ext). The conductor was not extended towards other directions, as the surrounding sites indicate that it is not present beneath them.

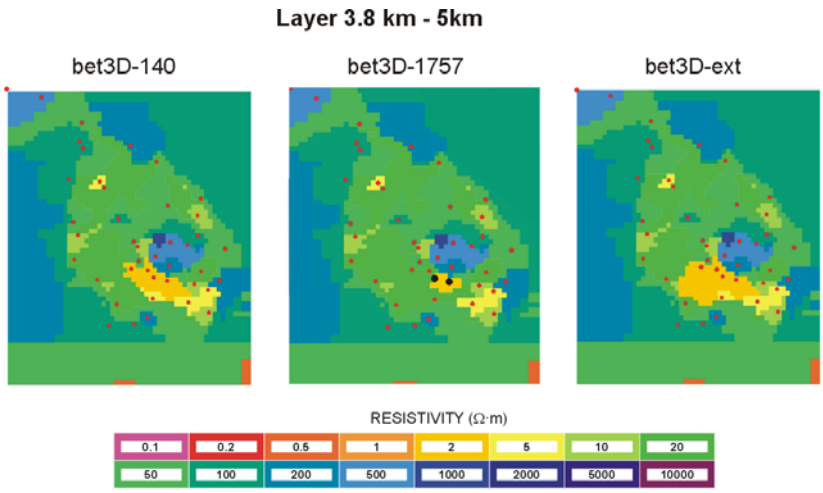

Figure 10.9: Horizontal representation of the 3.8 km – 5 km layer corresponding to bet3D-140 model and the two models testing the extension of conductor **CF3**. In the test model bet3D-1757, the extension of **CF3** reduced to just beneath sites b17 and b57 (locations indicated as black circles on the plot). In the test model bet3D-ext, the conductor **CF3** is extended towards the southwest.

Comparing the rms values corresponding to the determinant responses of these two models with those of the original model (bet3D-140) it can be observed that these changes in the model extension only affect the longest periods (Figure 10.10). Moreover, the resistivity rms values of the sites located above and around the areas are affected by the modifications in the conductor extension (framed region in Figure 10.11).

In the model bet3D-1757, the resistivity rms increases, for periods longer than 50s, in the west and central parts of the framed region (sites b54, b18, b52, b17 and b35), and there is no part of the rms map where this value decreases. Consequently, this model is not considered valid.

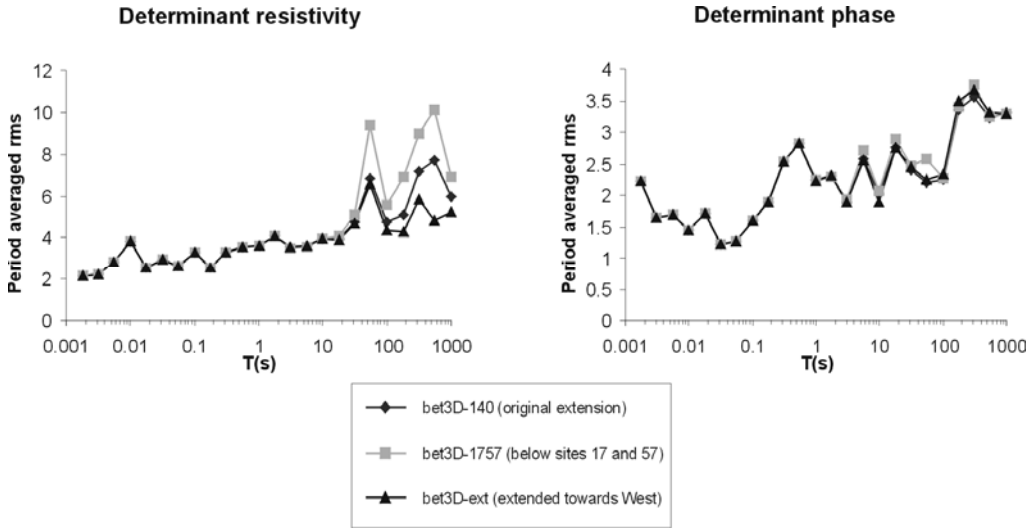

Figure 10.10: Period averaged determinant rms values corresponding to 10% error in the resistivities and 2.9° in the phases, calculated for the three models with different extensions of the conductive body **CF3**. Final model bet3D-140, model bet3D-1757, with the conductor confined below sites b17 and b57; and model bet3D-ext, with the conductor extended towards the southwest.

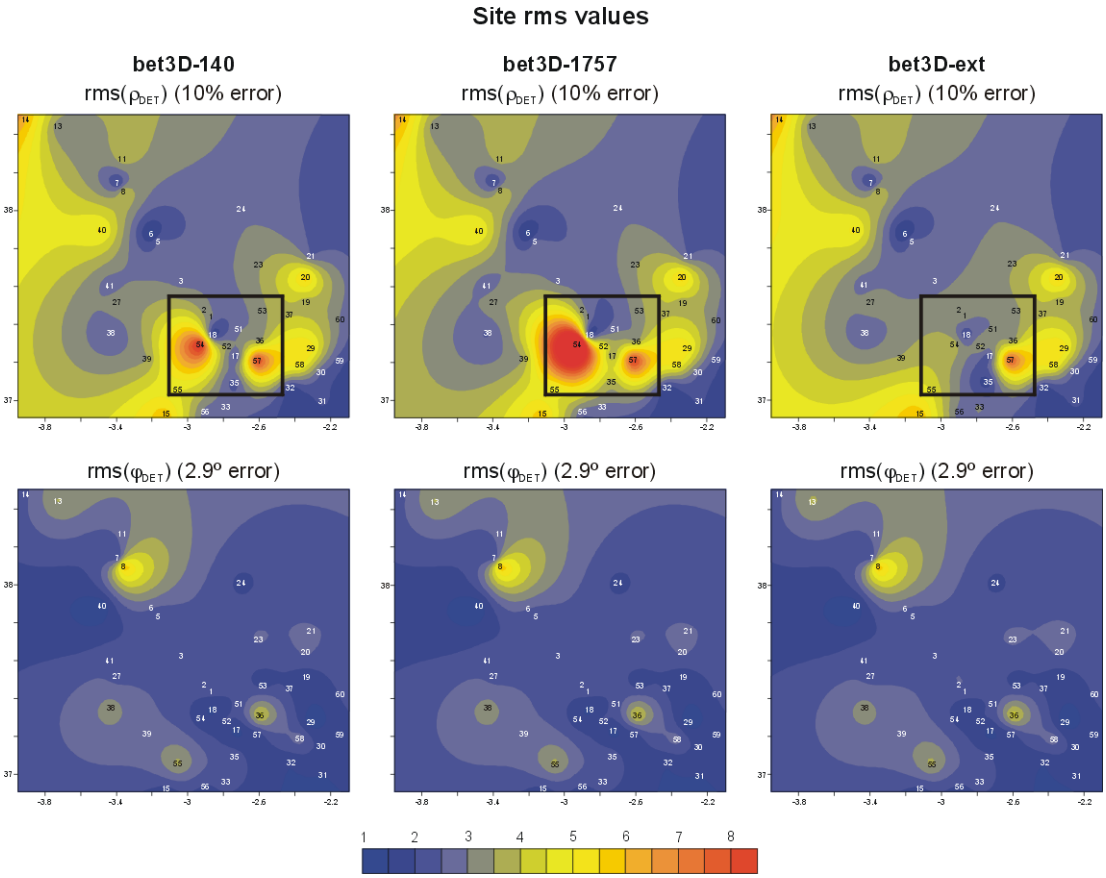

Figure 10.11: Rms maps of the determinant resistivities and phases of the Betics MT sites with respect to models bet3D-140 (original), bet3D-1757 (conductor located below sites b17 and b57) and bet3D-ext (conductor extended towards southwest) models. Numbers on the maps indicate site locations. Frames in resistivity maps show the areas of significant differences between the three models.

As for the model bet3D-ext, the rms values of the determinant resistivity are in general smaller (Figure 10.10). Although in the north-central part of the framed area, it has a slight increase, the rms values decrease drastically at site b54 and, to a lesser degree, at sites b17 and b35. Hence, the model det3D-ext, with the conductor body **CF3** extended towards the west and with an E-W orientation is also compatible with the data responses.

CF3 body depth tests:

The original model, with conductor **CF3** extending vertically from 3.8 to 17.5 km, was modified, in five new models, through changes in the depth positions of the conductor top and bottom (Figure 10.12).

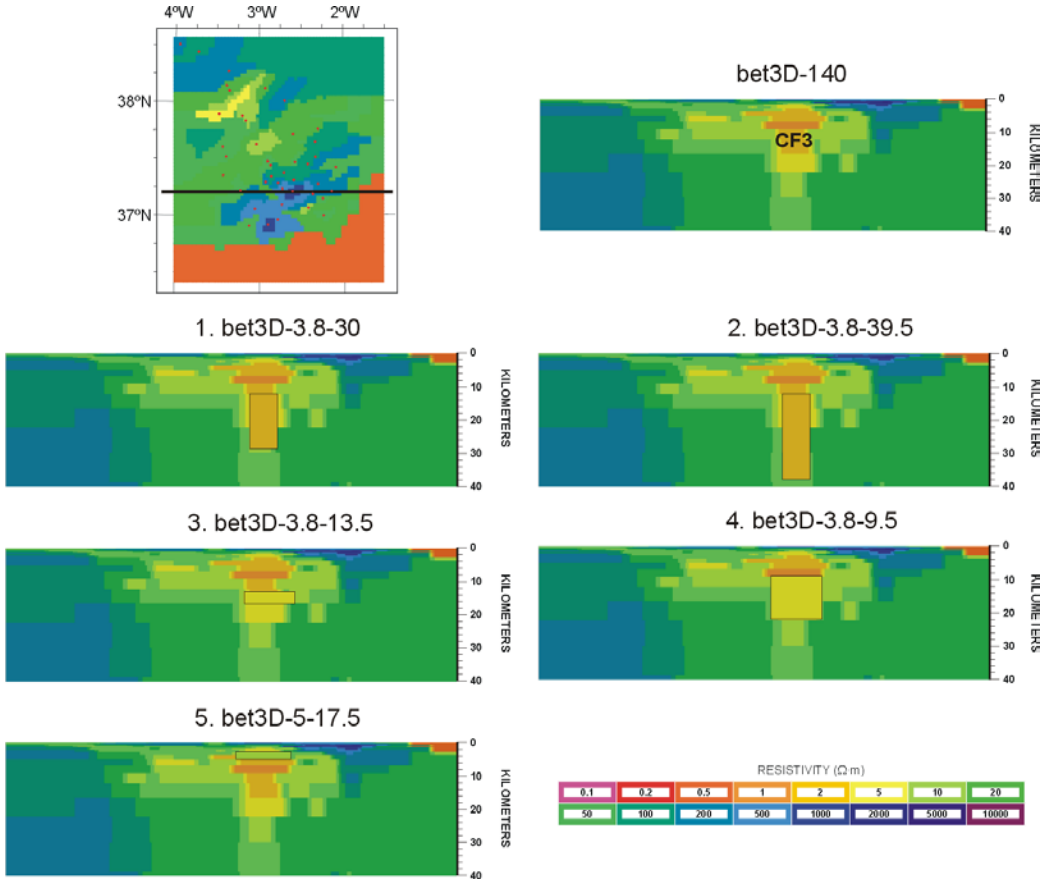

Figure 10.12: Vertical sections of the models created to test the depth sensitivity of the **CF3** conductor. Top: section of the original bet3D-140 model. 1, 2, 3, 4 and 5: sections of the modified models. Numbers in the model names refer to the top and bottom of the modified conductor **CF3** (e.g. 1: top 3.8 km, bottom 30 km). Framed areas in the model sections indicate modified conductivity zones. Location of the vertical sections is indicated in the plan view of the bet3D-140 model (top left corner).

The comparison between the different models only shows significant changes in the values of the rms(ρ_{DET}), and not in the rms(φ_{DET}) (Table 10.2). If the top of the conductor is fixed, the rms values are similar if its bottom is displaced by up to 39.5 km (models 1, 2 and 3), and increases if the bottom is located at an upper position (model 4). On the other hand, changes in the top of the conductor show that its top cannot be at lower depths, given the considerable increase of the rms when the top is located at 5 km depth (model 5). Hence, the conductor **CF3** must have a top located at 3.8 km and a bottom position that may vary from 17.5 km to 30 km depths.

Rms/ model	bet3D-140 (3.8 km-17.5 km)	1. det3D-3.8-30	2. det3D-3.8-39.5	3. det3D-3.8-13.5	4. det3D-3.8-9.5	5. det3D-5-17.5
rms(ρ_{DET})	4.08	4.07	4.08	4.15	4.33	5.38
rms(φ_{DET})	2.32	2.32	2.33	2.32	2.33	2.37

Table 10.2: rms values of the determinant resistivity and phase between data and model responses of bet3D-140 and the 5 models with modifications in the vertical extent of the conductive body, CF3.

Continuity between CF3 and CF1 and CF2 conductors:

In order to test if the conductor **CF3** is in fact connected to the overlying conductors **CF1** and **CF2**, or if, on the contrary, it is separated from them by a relatively resistive zone, two new models were created. Both models include a moderate resistive layer (20 Ω·m) located over the top of the conductor **CF3**. One with the top located at 2.8 km, and a thicker one with the top located at 2 km (Figure 10.13).

Rms(ρ_{DET}) values in both cases are significantly larger than in the original model (Table 10.3). This increase is rather proportional to the separation between **CF1**-**CF2** and **CF3**. Hence, it can be stated that these conductors are vertically connected, or, if they are separated, it is by a thin resistive layer (<400 m).

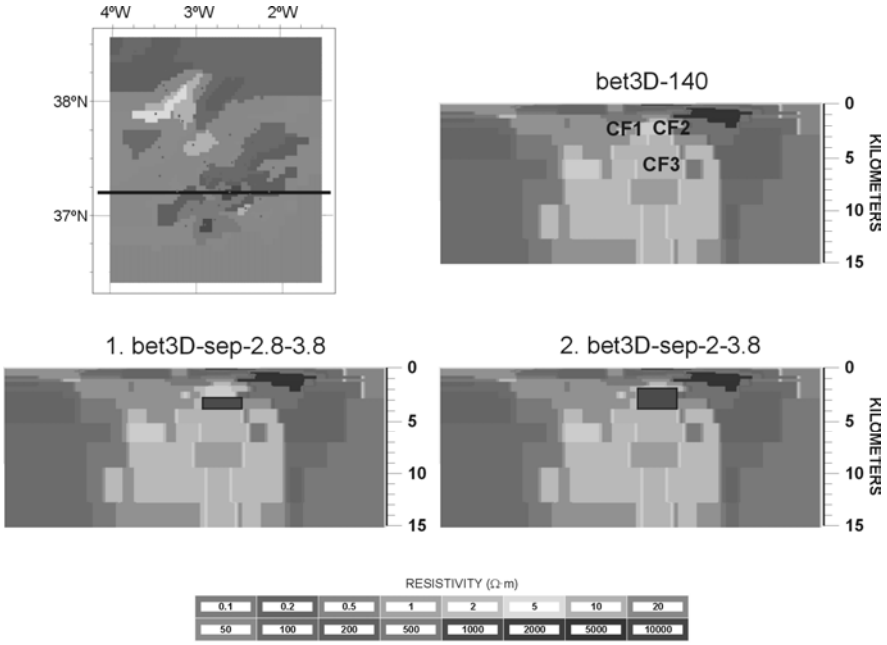

Figure 10.13: Vertical sections of the models created to test the sensitivity of the separation between CF1, CF2 and CF3 bodies. Top: section of the original model bet3D-140 model. 1 and 2: sections of the modified models. Numbers in the model names refer to the top and bottom of the zone where conductivity values were replaced by resistivive ones (black zones, 20 Ω·m). Location of the vertical sections is indicated in the plan view of the bet3D-140 model (top left corner).

Rms/ Model	**bet3D-140** (no separation)	**bet3D-sep-2.8-3.8**	**bet3D-sep-2-3.8**
rms(ρ_{DET})	4.08	4.51	4.99
rms(φ_{DET})	2.32	2.33	2.37

Table 10.3: rms values of the determinant resistivity and phase between data and model responses of bet3D-140 and those of models bet3D-sep-2.8-3.8 and bet3D-sep-2-3.8, introducing a separation between CF1, F2 and CF3 bodies.

10.7 Model Evaluation

The comparison between data and model responses shows that the model bet3D-140 is consistent, given the low and medium values of the rms observed in the determinant resistivities and phases. However, three main weak points of the model can be stated:

The first one is the difficulty to fit all MT tensor components, as has been reflected in the large rms values of the WAL invariants. Such a problem can be attributed to the limited possibilities in the trial and error modelling process and to the complexity of the area.

The second is the large variation in the rms value among different sites, attributed to the difficulty to fit data from close sites with significantly different responses. Then, one must bear

in mind that the parts of the model below isolated sites with low rms values are not better imaged than those parts below a high density of sites and a high rms value.

The third is the loss of resolution at depth, as reflected by the increase of the rms values with the period. This fact is more important below conductive zones, where the skin depth is shorter.

All these problems could be improved by the acquisition of a denser site distribution and longer time series to obtain longer period data and the use of inversion procedures.

With regard to the sensitivity tests performed, these have corroborated the validity of the model and its most significant features. The model shows to be stable to the mesh size, with the exception of site 14 due to boundary problems.

In relation to the conductivity body **CF3**, detailed sensitivity tests denote that:

1) This needs a maximum top depth of 3.8 km, which can be separated by up to 400 m from the upper bodies **CF1** and **CF2**.
2) Its orientation can vary from WNW-ESE to E-W, given the compatibility between the original model and the model with the conductor extended towards the west.

Although other models with a larger extension and depth of the conductor **CF3** have been shown to be valid, bet3D-140 is considered in the interpretation. This is the one that presents a minimum acceptable structure, and, as it will be shown in section 11.9, it has been considered very difficult to interpret a conductive body reaching depths of 30 km, where the model lacks resolution.

10.8 Comparison with other Geophysical Data

The comparison between the 3D model obtained from MT data (bet3D-140) and the available geophysical data in the study area, allows inference of the following:

The Moho and the boundary upper and lower crust (ULCB) depicted from seismic refraction and deep reflection profiles ESCI-B1 (only the Moho) and ESCI-B2 cannot be equally identified in the MT model (Figure 10.14). Thus, it is neither possible to detect the presence of a crustal root below the Internal Zone, as indicated by gravimetric data. The non-identification of these two limits may be because they cannot be distinguished electrically and hence cannot be correlated with the seismic reflectors (e.g. Holmes's Curious Dog, Cook and Jones, 1995), or in the case of the Moho, to a lack of resolution at these depths.

The bottom of the shallow conductor **CGB**, located where the Guadalquivir Basin infill outcrops with continuation towards the Prebetic and Subbetic zones, is coincident with the reflector observed in the seismic reflection profile ESCI-B1 and with a sudden variation in the velocity (refraction seismology). This velocity change and the presence of the reflector are

interpreted as the base of the Guadalquivir Basin, i.e., the top of the Variscan basement (Galindo-Zaldívar *et al.*, 1997).

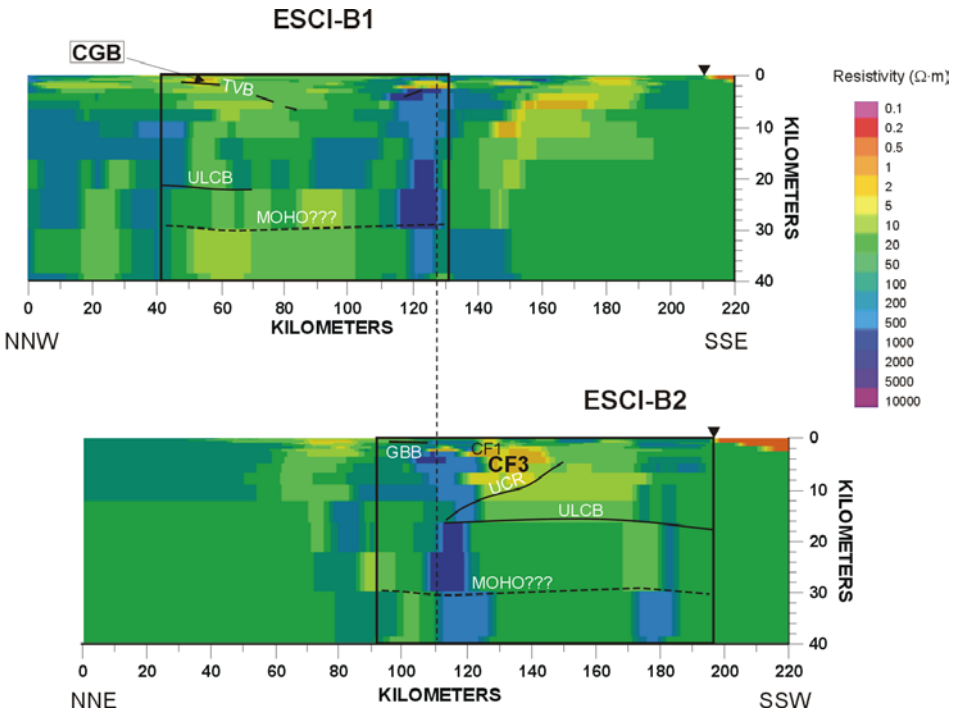

Figure 10.14: Cross sections of 3D conductivity model bet3D-140 along ESCI-B1 and ESCI-B2 seismic reflection profiles with the main interpreted reflectors and conductors. Framed areas indicate the areas covered by these two seismic profiles. White names identify reflection lines, black letters, conductive bodies. Vertical discontinuous line is the tie line. Inverted triangles: coast line. TVB: top of Variscan Basement reflector; ULCB: upper-lower crust boundary reflector; GBB: Guadix-Baza Basin reflector; UCR: upper crust reflector; CGB: Guadalquivir Basin conductor; CF1 and CF3: Filabres conductors.

The conductor **CF3** located beneath the Internal Zone is located slightly SW of a strong magnetic anomaly located at the NNW part of the Sierra de los Filabres (Figure 10.15). This anomaly has a maximum amplitude of 70nT and a dipole length of 15 km – 20 km, which is not incompatible with being caused by the conductor body **CF3**, if it had the required magnetic characteristics.

Along the seismic reflection profile ESCI-B2, the SSW limit of this conductor agrees with the location of the UCR reflector. Yet, there is no significant change in the gravimetric, heat flow and seismic tomography data that could be correlated with the presence of the conductor **CF3**.

Finally, there is no direct correlation between the geoelectric structures, the seismicity and the seismic tomography. However, over and surrounding the conductive body **CF3**, at

depths between 5 km and 17 km, the seismicity is relatively low (Figure 10.16) and this conductor is located over a broader area with relatively high seismic v_p values (Figure 10.17).

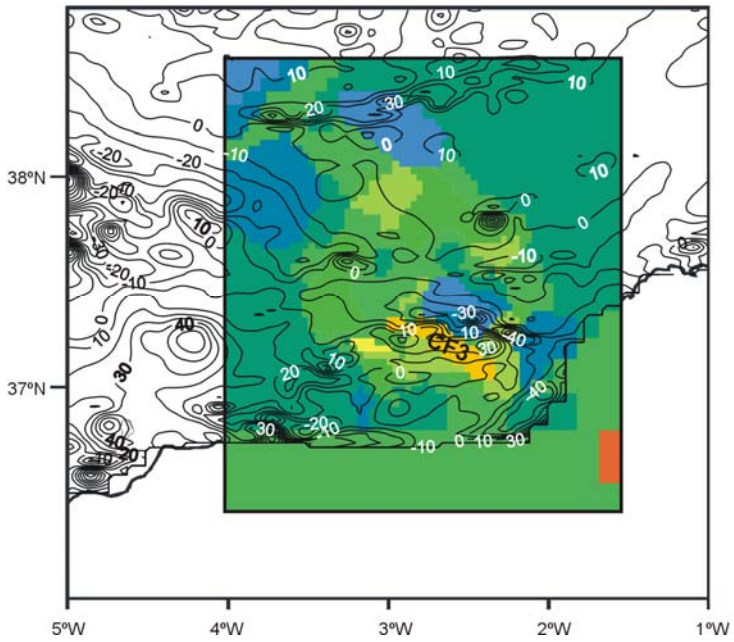

Figure 10.15: Superposition of the total magnetic anomaly map (see chapter 6, Figure 6.7) with layer 5 km-7 km (Figure 10.2l) from model bet3D-140. Isomagnetic anomaly values are in nT.

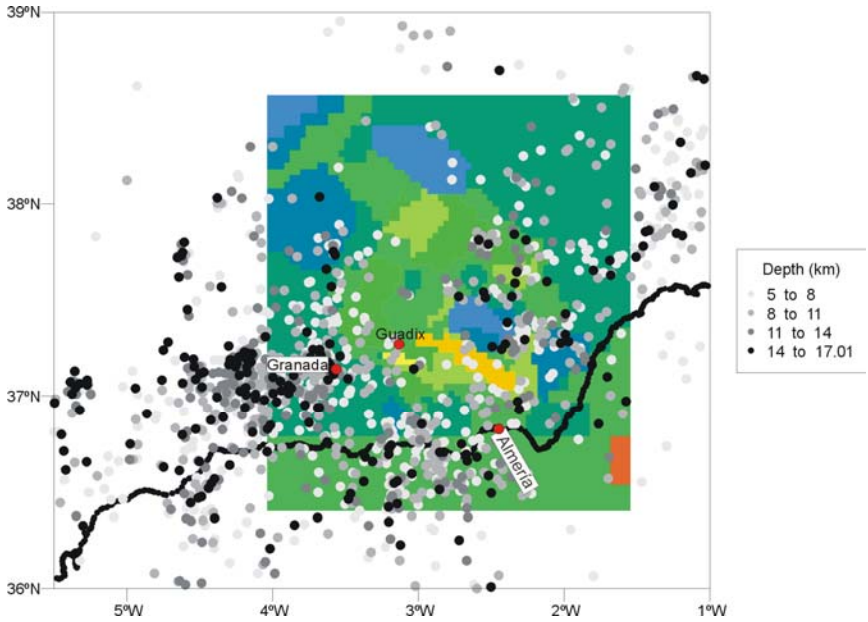

Figure 10.16: Seismicity map of the 3D model area and surroundings, showing only the seismic events from 5 km to 17 km. The coloured background represents the layer 5 km to 7 km of the 3D model bet3D-140.

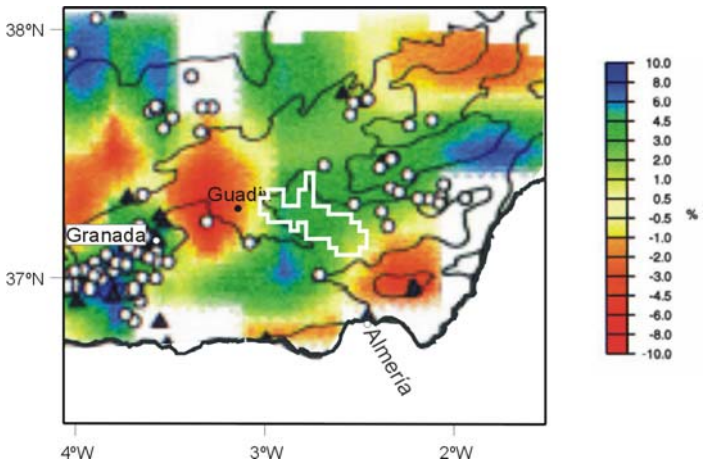

Figure 10.17: Tomographic P-velocity anomalies map corresponding to layer 4 km - 12 km ($\langle v_P \rangle$ = 5.7 km/s). The white outline represents the layer 7 km – 9 km of the conductive body CF3.

10.9 Interpretation

The comparison between the geoelectric structures imaged in the 3D model and the available geological and geophysical information allowed proposing the following interpretation of the main resistors and conductors recognised in this 3D model.

This interpretation is described in the same order as in the model description (section 10.4) and includes a specific subsection with the discussion of the high conductive body **CF3**, located below the Internal Betics.

Iberian Massif:

This part of the model is characterised by a moderately high resistive zone (**RIM**), with a relatively conductive zone (**CIM**) between 2.15 km and 17.5 km, overlain at the southeast by two shallow conductors, **C7-8** and **C-11**.

Considering the outcropping materials and their structure, the resistive zone **RIM** can be associated with the Variscan basement formed by metamorphic and granitic rock. The relatively high conductivity of **C7-8 (**Figure 10.3f, page 214) and **C-11** (Figure 10.3h, page 215), located from 1 km to 2 km depth, which is coincident with the bottom of the Mesozoic cover that overlies the Variscan basement next to the Guadalquivir Basin. This high conductivity is interpreted as due to fluid circulation through the detrital sediments of the base of this cover.

With reference to the NE-SW oriented conductor **CIM**, it does not crop out at the surface and it is not parallel to any of the geologic structures observed at surface, which are mainly NW-SE. Lacking more information, it is proposed that it may be associated with a

lithologic change. In this sense, it may be noted that 200 km towards the west, MT studies (Muñoz, 2005) show even more conductive bodies (5 Ω·m) at similar depths that have been related to the graphite rich Precambrian Serie Negra rocks. Their elevated conductivity has been attributed to the interconnection of graphite grains. These rocks are present in all the Central Iberian Zone, and hence, in the study area as well, although given their higher resistivity values, with a lower content and/or lower interconnectivity.

Guadalquivir basin:

The model shows a shallow E-W oriented conductive body, **CGB**, decreasing in extension with depth that overlies a moderately resistive zone with similar values as in the Iberian Massif.

The coincidence between the shape of the **CGB** conductor at the surface and the outcropping infill of the Guadalquivir Basin, denotes that this conductor is related to this infill, and therefore reproduces its shape (Figure 10.18). Thus, the MT model shows that the maximum depth and thickness of the basin infill increases towards the SE, where it reaches a maximum thickness of 5 km. The high conductivity of the basin infill (5Ω·m) is related to fluid circulation through its poorly consolidated sedimentary layers.

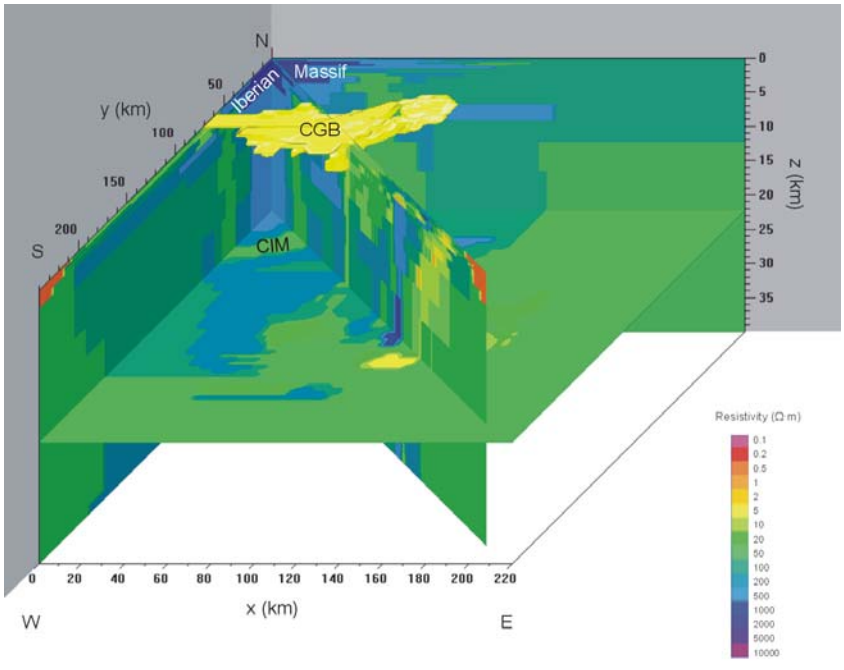

Figure 10.18: 3D view of bet3D-140 conductivity model, in which NS, EW as well as a NW-SE directed vertical slices and a horizontal slice at 22 km are plotted. A 3D view of the 5 Ω·m conductive zone corresponding to the Guadalquivir basin (CGB), and Iberian Massif main features (high resistivity, RIM; and conductive zone CIM) are also plotted.

External Zone:

This zone is characterised by a shallower level (up to 1.2 km - 2.15 km) of moderately resistive values that is more conductive to the south (**C20** and **C27-38**) and overlies a thin conductor, which is in continuity with the conductor **CGB** recognised in the Guadalquivir Basin. Below, in this entire zone there is a relatively high resistive zone.

The elongation in depth of the conductor **CGB** allows delimiting the continuation of this foreland basin below the External Zone, up to 20 km E beneath the Prebetic zone, and up to 30 km S beneath the Subbetics.

The overlying shallow level of moderately resistive values and the conductors **C20** and **C27-38** are associated with the Mesozoic and Cenozoic rocks forming the External Zone of the Betics. The shallow moderate resistivity is related to fluid circulation in carbonated rocks of the Prebetic and outer Subbetic zones; and the conductivity of **C20** and **C27-38** to a major content in shales and the presence of basaltic rocks in the inner Subbetic. The significantly higher conductivity of **C20** indicates that it can be directly attributed to the presence of flysch rocks in this area, which continue NW below the Inner Subbetic materials (Jabaloy *et al.*, 2005) (chapter 6, figure 6.9), below the location of site b20. Differences in the composition and/or porosities between the flysch and inner Subbetic rocks can explain the different conductivity values observed between these two zones.

The continuation of **C20** and **C27-38** below the Internal zone denotes that the External Zone and/or the Flysch units are partially overthrusted by the Internal zone.

Below the conductors and moderately resistive zone of the External Zone and the Guadalquivir Basin, the higher resistivity values are associated with the continuation of the Iberian Massif below the External Zone.

Internal Zones:

This part of the model shows a resistive zone, up to 13.5 km (**RI**), among which several conductors appear as well as a deeper and larger conductor (**CF3**). The shallow conductors appear beneath the Sierra de los Filabres at depths between 1.6 km and 3.8 km (**CF1** and **CF2**), and beneath the Sierra de las Estancias (**CE**) and Sierra de Alhamilla (**C31**), reaching in these cases 2.8 km and 2.15 km respectively. The larger conductor **CF3** has a top that can be more or less variable, depending on whether it includes **CF1** and **CF2** conductors or not. In any case, this top would be situated at depths from 1.6 to 3.8 km in the WNW (or W) part and 3.8 km in the ESE (or E) one. Its base dips from 5 to 9 km (below the NW and SE extremes) to 17.5 km (below the central part of Sierra de los Filabres, i.e., site 57).

The high resistivity values of first layers below the Alpujárride and Nevado-Filábride complexes (**RI**) are caused by metamorphic materials, mainly graphitic schists. Despite its

graphite content, the bulk resistivity of these metamorphic rocks is high, which may be caused by a separation of the graphite films during their uplift (e.g. Mareschal *et al*., 1992), contrary to the high conductivity observed in the Serie Negra (Iberian Massif), where the graphite films are connected (e.g. Keller and Frischkneht, 1966).

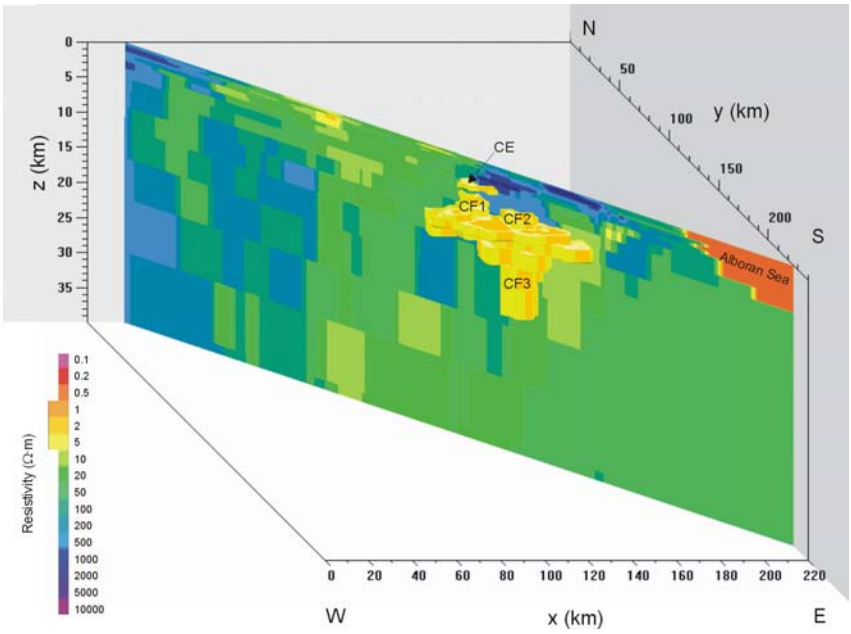

Figure 10.19: N45°W vertical cross section of the 3D model plus a 3D representation of the conductive zones (1 Ω·m, 2 Ω·m and 5 Ω·m) imaged below the Internal Zone.

The size and location of the shallow conductors in the areas affected by folded extensional detachments bounding the Alpujárride and Nevado-Filábride complexes or different Nevado-Filábride units (Figure 10.4) suggests that they are generated by fluid circulation along these fractures.

10.9.1 CF3 high conductivity

The WNW-ESE orientation, parallel to the Variscan structures and tectonic zones, together with the alignment with the conductive Variscan pyrite belt that outcrops NW of the conductor **CF3**, could suggest that this conductor belongs to the Iberian Massif. However, its shallow top makes this interpretation very improbable, as it would imply that the Betics detachment would be located below the Internal Zone at depths of only 3 km -5 km, implying a sudden uplift of such a detachment which, dipping to the SE is located at 10 km depth at the Internal – External boundary zone.

Given its vertical location and extension, the interpretation of **CF3** as belonging to the Alboran domain, seems the more plausible. Under this hypothesis, it is located between the overlying Nevado-Filábride resistive metamorphic rocks (with a total thickness from 1.6 km to 4 km) and the Betics-Iberian crustal detachment level (see NNW-SSE model cross section superposed over Transmed I section, Figure 10.20), in the core of the major antiform that crosses EW the central parts of the Sierra de los Filabres and Sierra Nevada (Figure 10.5).

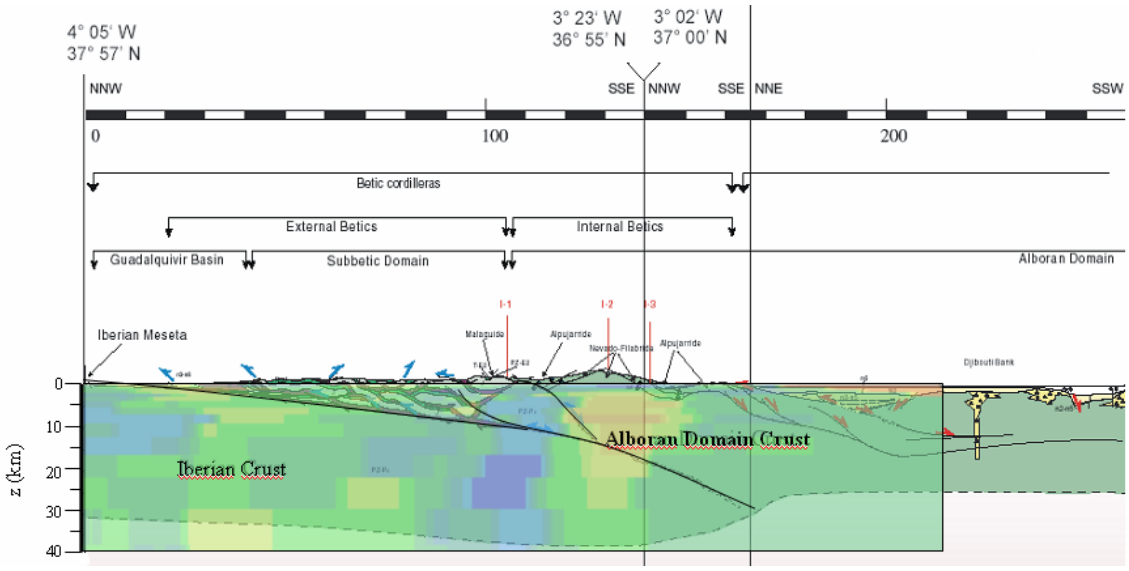

Figure 10.20: Transmed Transect I with a NNW parallel cross section of the 3D model projected.

In this tectonic setting, the conductor is located in an area where available geophysical information shows:

1) A moderately high seismic v_p anomaly between 4 km and 12 km depth (Dañobeitia *et al.*, 1998) (Figure 10.17).
2) Low seismic activity (Figure 10.16).
3) The local coincidence between the location of UCR reflector and the bottom of **CF3** conductive body (Figure 10.14).
4) A magnetic anomaly (-40nT to +30nT) with an almost E-W orientation, with the centre of its western edge coinciding with the WNW edge of the conductor **CF3** (Figure 10.15). This anomaly has been modelled by Galindo-Zaldívar *et al.* (1997) as a 10 km thick magnetic body caused by Fe-mineralisation along joints in the Nevado-Filábride metamorphic rocks, up to a depth of 10 km.
5) High topography (peaks up to 3500 m) located over an area in which the proposed gravimetric models do not show any significant crustal root.

6) Crustal geotherms, calculated for the Betic Chain (Zappone *et al*., 2000) from available heat flow data (Fernàndez *et al.*, 1998b), estimate a range of temperatures at the depths of **CF3** between 100ºC at its top (3.8 km), to 325ºC-500ºC at its bottom (17.5 km).

In Earth materials, as already seen, high electrical conductivity anomalies can be due to the presence of fluids, partial melting or high conductive mineral phases (e.g. Jones, 1992). In the later, the high conductivity depends on their composition and interconnection level.

With reference to conductive body **CF3**, the presence of fluids alone makes it difficult to explain the large volume of the conductor, its location in the axis of the antiform, the moderately high seismic velocity values and the low seismic activity (the presence of fluids at the considered depths implies elevated pore fluid pressures which decrease the ultimate strength, rupture strength and ductility, Davis and Reynolds, 1996).

The hypothesis of partial melting was rejected too, as it commonly needs minimum temperatures of 700ºC (Thompson, 1992), significantly higher than those estimated from heat flow data (see above). Only if **CF3** reached depths up to 30 km, as can be accepted from the sensitivity tests, could partial melting be considered just for the deepest kilometres of the conductor (27 km to 30 km).

Therefore, the high conductivity of the conductor **CF3** seems to be due to the presence of highly conducting mineral phases. According to the geophysical observations the conductor must also be a material with moderately high v_p values, of a ductile nature or mechanically resistant (low seismicity), and likely high density.

As already stated, **CF3**, according to the heat flow data, must have temperatures ranging between 100ºC and 500ºC. For most materials, these temperatures are below the Curie temperature, and hence, it could explain the westernmost part of the magnetic anomaly observed (Figure 10.15).

Kiss *et al.* (2005) demonstrated the effects of the increase of magnetic susceptibility just below the Curie temperature over magnetic and magnetotelluric data (Hopkinson effect), which is considered more significant than previously thought. If this effect is not considered, magnetic anomalies are interpreted as being caused by large magnetic bodies. Over 2D and 3D MT data, the interpretation results in an ensemble of highly conductive and highly resistive zones. Within the depth range of **CF3**, if the Curie temperature were reached and the Hopkinson effect occurred, it would only involve a layer of a few hundreds of meters. Hence, even if this transition occurred, the whole conductive body **CF3** could not be replaced by a body with lower conductivity values and higher magnetic susceptibilities.

Another geophysical constraint to be considered is the non-existence of a significant crustal root below the highest topography as interpreted (Torné and Banda, 1992) from the Bouguer anomaly map (Figure 7.6). The emplacement of a dense body in the crust below the

high peaks of Sierra Nevada and Sierra de los Filabres, and the addition of a crustal root, is compatible with the observed gravimetric data (e.g. a body with a density 0.1g/cm^3 higher than the average crustal value will result in a crustal root of 7 km). Hence, the conductive body **CF3** can have a higher density than the average crustal rocks, which would allow for the existence of a crustal root below the Internal Zone.

In order to explain the reasons of the high conductivity of this body, it must be considered how the conducting mineral phases interconnect as to increase the bulk conductivity of a rock. In the case of graphite, it forms thin films that are easily interconnected; whereas other conducting minerals (e.g. pyrite and pyrrhotite) need an additional mechanism to enable their interconnection. This mechanism may be fluids that spread the massive sulphurs forming a matrix allowing for their interconnection. Although these fluids are subsequently released, the interconnected matrix, and hence, the high conductivity prevails.

Considering high seismic velocities, low associated seismicity and high density, the rock hosting these conducting minerals must be a ultrabasic or basic rock, such as ophiolites (e.g. gabbro) or peridotites. In the Betics, rocks of the same type have been observed in the ophiolitic units of the Nevado-Filábride complex, and in outcrops at the western sector of the Betics (Ronda, Alpujárride complex), in some cases partly serpentinized (Zappone *et al.*, 2000). However, especially in the case of ophiolites, the seismic velocity values would be much higher than those estimated, although the v_p values obtained from seismic tomography are averaged over a large depth range. Another possibility is continental lower crustal rocks (amphibolites or granulites). Based on the present geologic and geophysical constraints it is not possible to discern among these hypotheses. Additional petrologic studies and resistivity measurements *in situ* of outcropping materials of the same type as those discussed above, and detailed tomographic and gravimetric studies would provide more constraints on the exact nature of this body.

Summarizing, the highly conductive body has been interpreted as ophiolitic or as lower crustal rocks with some type of mineralization (graphite or pyrite) that enhances the conductivity in a large volume at depths between 4 km and 17.5 km. This differentiated lithologic unit would be located beneath the Nevado-Filábride complex, along the core of the E-W major antiform of the Sierra de los Filabres and Sierra Nevada. This antiform forms a culmination over the conductor **CF3** and plunges east in the east and west in the west. Such geometry, combined with the south-dipping plane of the basal Betic detachment, would explain the disappearance of the conductor east and west of the study area (Figure 10.21). Taking this geometry into account, the conductor would be E-W oriented. In the 3D model, its orientation is WNW-ESE, although, as shown in the sensitivity studies, it can be also E-W, in accordance with the explained geometry.

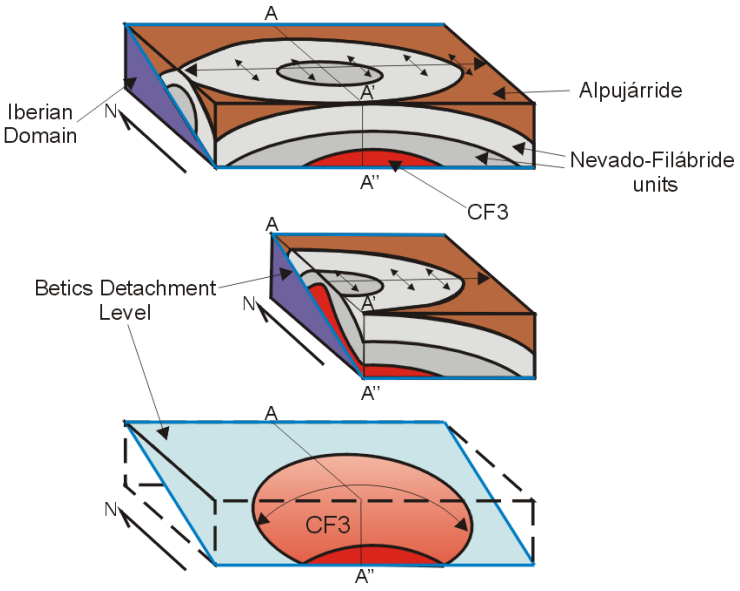

Figure 10.21: Schematic representation of the position of conductor CF3 in the Internal Zone complexes.

10.9.2 Regional geodynamic implications

From the interpretation of the 3D model, the following regional constraints can be added on the geologic and geophysical knowledge of the study area:

- The continuation of the External Zone below the Internal Zone in the Central Betics is only of a few kilometres, as shown by the elongation of the conductive bodies of the External Zone towards the south. Analogously, the conductivity contrast between the Guadalquivir Basin sediments and the External Zone show the continuation of the Guadalquivir basin up to 20 km E beneath the Prebetic zone, and up to 30 km S beneath the Subbetics.
- The emplacement of a differentiated lithologic unit in the core of the main Nevado-Filábride antiform (conductor **CF3**) reinforces the hypothesis that the Internal Betics are formed by an antiformal stack of crustal or even mantle thrust sheets, bounded by a major south-dipping sole thrust. This thrust separates the allochtonous rocks of the Alboran Domain from the authochtonous Iberian plate and belongs to the southern continuation of the sole thrust of the External Betics.
- The presence of mantle or lower crustal rocks below the Central Betics suggests that the mechanism that emplaced peridotitic bodies in some sectors of the western and southern parts of the Gibraltar Arc affected a broader area. This mechanism implied exhumation of mantle rocks at depths of about 180 km.
- The effect of this higher density body opens the door to a new gravimetric model, which would agree with the presence of a crustal root below the Internal Betics.

10.10 Conclusions

This chapter has described the construction of a 3D conductivity model of the Central Betics, from the Iberian Massif to the Alboran Sea, from the first meters to lower crustal levels, the results obtained, how the model was tested and its interpretation, considering other available geological and geophysical information.

A preliminary model was constructed from the extrapolation of 1D models inverted from determinant data at each site, towards a three-dimensional mesh. This initial model was extended towards the Alboran Sea and surrounding areas, whose conductivities were imaged using available surface data. The model mesh consisted of 50x50x25 elements with total dimensions of 270 km(NS) x 220 km(EW) x 100 km(z).

Successive steps to obtain a reliable model consisted of a trial and error process, whose objective was to reach an acceptable misfit between model and data responses.

The final model, termed bet3D-140, was obtained after 140 steps. This model is characterised by average resistivity values between 50 Ω·m and 100 Ω·m. Over this, some resistive zones appear, interpreted as the metamorphic and granitic rocks of the Iberian Massif, and the metamorphic rocks of the Internal Zone. Shallow conductive bodies are associated with the Guadalquivir Basin sediments and with the sedimentary materials of the Subbetic units. In depth, these two conductive regions continue towards the south, i.e., the Guadalquivir sediments below the External Zone, and the External Zone below the Internal Zone.

Among the resistive materials of the Internal Zone, shallow conductors are interpreted as due to fluid circulation along the contacts between the Nevado-Filábride and Alpujárride complexes or different units of the Nevado-Filábride. Below the Sierra de los Filabres, a deep conductor, **CF3**, extends in depth from 4 km to 17.5 km, with resistivities between 1Ω·m and 5Ω·m.

A sensitivity test of the model and its main features was performed, which proved the stability of its mesh, and allowed testing the extension, depth and resolution of the conductive body **CF3**. The main results were that the extension of this conductor could continue some kilometres towards the west, have an orientation from E-W to WNW-ESE and its bottom could also continue up to 30 km depth.

Based on geological and geophysical constraints, the deep conductive body is interpreted as a differentiated lithologic unit formed by ophiolites or lower crustal rocks containing a conducting mineral phase below the Nevado-Filábride complex. This body is located in the core of the main Sierra Nevada – Sierra de los Filabres antiform, and extends in depth up to the Betics detachment level.